

MID SWEDEN UNIVERSITY

MASTER THESIS

**Design and implementation of
piezoelectric energy harvesting for low
frequency industrial and maritime
application**

Author:

Mats G. Eliassen

*A thesis submitted in partial fulfillment of the requirements
for the degree of Master of Science*

July 2014



KONGSBERG



MID SWEDEN UNIVERSITY

The Department of Information Technology and Media

Examiner: Prof. Bengt Oelmann
bengt.oelmann@miun.se

Supervisor: Rune Harald Hestmo
rune.harald.hestmo@km.kongsberg.com

Author: Mats Granmo Eliassen
matsge@gmail.com

Degree programme: International Masters in Electronic Systems
and Instrumentation, 120 credits

Main field of study: Master's Thesis Work in Electronics

Semester, year: Spring, 2014

MID SWEDEN UNIVERSITY

Abstract

Faculty of Science, Technology and Media
Department of Electronic Design

Master of Science

Design and implementation of piezoelectric energy harvesting for low frequency industrial and maritime application

by Mats G. ELIASSEN

In this thesis a system for harvesting vibrational energy it designed and implemented using the LTC3588 from *Linear Technology* as the power managing device. It is aimed at reducing the need for batteries as the main source of power in WSN nodes. A model for estimating power output of piezoelectric transducers is developed in COMSOL, but lacking damping parameters for the system the usable outputs from the model was few. Both a commercial (V21BL from *Midé*) and custom produced (PVDF) transducers were tested at frequencies in the 0 - 200 Hz area. Although the custom transducers showed promising output voltages, they could not be utilized for energy harvesting using the designed system. Using the commercial transducer, power was harvested in the milliwatt range for vibrations of up to 2 g (RMS) in amplitude. Additionally, solid state batteries were added to the design to accumulate any excess power, limiting the impact of short periods of low vibrational input.

Keywords: Energy harvesting, piezoelectricity, PVDF, PZT, transducers, vibration, COMSOL, electronics, low power, WSN.

Acknowledgements

I would like to thank:

My fellow classmates Vidar Berg, Torleif W. Utvik, Stig M. Celius, Martin S. Børns-Lind, Håkon G. Strømstad and Joachim K. Flem. Your friendship, discussions and advice have made these last years interesting and enjoyable.

Dag R. Hjelme and Dominik Osinski at HiST for your guidance and direction.

My family for your support throughout the years. You are the reason I made it this far.

Kongsberg Maritime for supporting me in this thesis and giving me access to both workspace and equipment. A special thanks goes out to Rune H. Hestmo who acted as project supervisor.

Contents

Abstract	v
Acknowledgements	vii
Contents	ix
List of Figures	xiii
List of Tables	xvii
Abbreviations	xix
Symbols	xxi
I Preface	1
1 Introduction	3
1.1 Background	3
1.2 Objectives	6
1.3 Scope	7
1.4 Concrete and verifiable goals	7
1.5 Outline	7
II Theory	9
2 Vibration characteristics	13
3 Piezoelectricity	17
3.1 Axis and notation	17
3.2 Piezoelectric coefficients	18
3.3 Piezoelectric materials	20
3.3.1 Selecting the best material	22
3.4 The piezoelectric transducer	24
3.4.1 Beam composition	25

3.4.2 Mechanical behavior	26
3.4.3 Electrical behavior	33
4 Power management	37
4.1 Maximum power vs. Efficiency	37
4.1.1 DC-power applications	38
4.1.2 AC-power applications	40
4.2 Different loading techniques	42
4.2.1 Complex conjugate impedance matching	42
4.2.2 Resistive impedance matching	43
4.2.3 Adaptive impedance matching	44
5 Power storage	51
5.1 Different power storage technologies	51
5.1.1 Capacitors	51
5.1.2 Batteries	52
5.1.3 Electric double layer capacitors	54
III Model and methodology	57
6 Methodology	59
6.1 Piezoelectric transducer	59
6.1.1 Material selection consideration	59
6.1.2 Simulation	59
6.1.3 Production	60
6.1.4 Commercial transducer	60
6.2 Power manager	60
6.2.1 Schematic and PCB design	60
6.3 Casing	61
6.3.1 Software	62
6.3.2 CAD modeling	62
6.3.3 3D-printing	63
6.4 Data acquisition and analysis	63
7 Modeling	65
7.1 Model geometry	66
7.2 Adding material properties	67
7.3 Defining relationships and external forces	68
7.4 Meshing	70
7.5 Verification and testing	71
IV Implementation	75
8 Transducers	77
8.1 Material selection	77
8.2 Production	77
8.3 Commercial transducer	79

9 Power manager	83
9.1 Component selection	83
9.1.1 DC-DC Converter	83
9.1.2 Power storage	86
9.1.3 Passives	87
9.2 Schematics	88
9.3 PCB design	90
9.4 Finished device	91
10 Casing	95
10.1 The box	95
10.2 The lid	96
10.3 The transducer clamp	96
10.4 Assembled view	97
10.5 Finished product	98
11 Measurement system	99
11.1 Data acquisition hardware	99
11.2 Data visualization and analysis software	102
V Results and Discussion	105
12 Results	107
12.1 Testing at Kongsberg Maritime	107
12.1.1 Transducer clamps	108
12.2 Testing at the Lab (HiST)	109
12.2.1 Transducer voltage	110
12.2.2 Harvested power	111
13 Discussion	117
14 Further work	121
15 Conclusion	123
Bibliography	125
VI Appendices	129
A Schematic - Sheet overview	131
B Schematic - Power management	133
C Schematic - Power storage	135

D Schematic - Input/Ouput	137
E Gerber - Bottom layer (approximate scale)	139
F Gerber - Top layer (approximate scale)	141
G Gerber - Bottom layer w/overlay (enlarged and mirrored)	143
H Gerber - Top layer w/overlay (enlarged)	145
I Mechanical drawing - Casing Bottom	147
J Mechanical drawing - Top Lid	149
K Mechanical drawing - Transducer clamps	151
L MATLAB script for frequency response	153
M LabVIEW documentation	155

List of Figures

1.1	Wireless devices per person 2003 - 2020 (estimated) [1]	4
1.2	Predicted value of global market for wireless sensor devices 2009-2016. Summary figure. [3]	4
1.3	Energy flow in piezoelectric energy harvesting system [4]	11
2.1	Exaggerated visualization of natural frequencies and mode shapes in ship hull [5]	13
2.2	A typical vibration spectrum measured from a running 4-stroke diesel engine (Wärtsilä 6L46F) [7]	14
2.3	The Wärtsilä 6L46F 4-stroke 7200 kW diesel engine.	15
3.1	The inverse piezoelectric effect	17
3.2	Common nomenclature for axis and dimensions of piezoelectric materials	18
3.3	Unit cell of perovskite crystal structure	21
3.4	Polarization of ceramic polycrystalline structure	21
3.5	Unit cell of Lead Zirconate Titanate (PZT)	22
3.6	Structure of Polyvinylidene Fluoride (PVDF)	23
3.7	Cantilever beam	24
3.8	Piezoelectric cantilever beam transducer composition (exploded view)	25
3.9	Comparison of bimorph and unimorph transducer	25
3.10	Illustration of SMDS.	28
3.11	Frequency response of magnitude factor	31
3.12	Strain distribution in bending body	32
3.13	Simplified thevenin-equivalent circuit of piezoelectric generator with voltage source [9]	33
3.14	Impedance of capacitor over frequency.	34
3.15	Simplified Norton-equivalent circuit of piezoelectric generator with current source [9]	35
4.1	DC source and load resistance	37
4.2	Efficiency of power transfer vs. Impedance ratio	38
4.3	Power dissipated in load vs. resistance ratio	40
4.4	AC source and load impedance	40
4.5	Inductance needed for complex conjugate impedance matching of capacitive source vs. frequency.	42
4.6	Fundamental switch-mode converter topologies.	44
4.7	Voltage and current characteristics for inductor [18]	45
4.8	Buck converter circuit for piezoelectric energy harvesting proposed by Ottoman et al. [20]	48

4.9	Buck-boost converter circuit for piezoelectric energy harvesting from a PZT source, proposed by Inman et al. ^[16]	49
5.1	Illustration of plate capacitor [edited]. ^[21]	51
5.2	Equivalent circuit of capacitor.	52
5.3	Leakage current for supercapacitors over time ^[24]	54
7.1	COMSOL Multiphysics ^[29]	65
7.2	FR4 material domain (FR4 marked as blue).	67
7.3	Piezo material domain (marked as blue). Identical domain exist on bottom side.	68
7.4	Prescribed displacement boundary in COMSOL (boundary placement marked as blue)	68
7.5	Prescribed displacement interface with time-dependent value in Z-axis.	68
7.6	Dimensions of V21BL transducer (imperial units) ^[31]	72
7.7	Eigenfrequencies of modeled Voltule V21BL transducer with no added end mass	73
8.1	8331S-15G silver conductive epoxy. ^[33]	78
8.2	The two produced transducers with 28 and 110 µm PVDF layers. PVDF layers exists on both top and bottom sides of both transducers.	79
8.3	Volute V21BL transducer from Midé ^[31]	79
8.4	Composite structure of V21BL ^[34]	80
9.1	Block diagram of LTC3588 DC-DC step-down (buck) converter ^[35]	84
9.2	PGOOD driving gate of N-channel MOSFET	85
9.3	Pinout of LTC3588 DC-DC step-down (buck) converter in 10-eMSOP package ^[35]	86
9.4	Top level schematic, showing schematic relationships in the project	88
9.5	Schematic of DC-DC converter and related passives	89
9.6	Schematic of battery backup, including batteries and charger circuits	89
9.7	Schematic of Input/Output connector, showing the available signals and pinout	89
9.8	Gerber (left) and 3D view (right) of top-layer of power manager	91
9.9	Gerber (left) and 3D view (right) of bottom-layer of power manager	91
9.10	Isometric view of PCB design with added component 3D-models	92
9.11	Finished power manager device (top view)	92
9.12	Finished power manager device (bottom view)	93
10.1	Rendering of bottom/main part of casing, 'the box'. Dimensions in mm.	96
10.2	Rendering of top part of casing, 'the lid'. Dimensions in mm.	96
10.3	Rendering of top part of transducer clamp. Dimensions in mm.	97
10.4	Rendering of bottom part of transducer clamp. Dimensions in mm.	97
10.5	Exploded view of casing with mounted power manager and V21BL transducer. No lid.	97
10.6	Photo of 3D-printed casing with power manager, transducer clamps and V21BL transducer mounted. No lid.	98
10.7	Photo of 3D-printed casing with power manager, transducer clamps and V21BL transducer mounted. Lid closed.	98

11.1 The NI9205 data acquisition module ^[28]	99
11.2 The NI9207 data acquisition module ^[28]	100
11.3 The compactDAQ cdaq-9174 data acquisition platform ^[28]	100
11.4 The accelerometer setup	100
11.5 Graphical User Interface of LabVIEW software	102
11.6 Conditioning of accelerometer signal in LabVIEW	102
11.7 Implementation of power measurement in LabVIEW	103
12.1 Overview of test setup at Kongsberg Maritime	107
12.2 Testing adjustable range of transducers with strobe light (HELIOTROB Compact-75)	108
12.3 Sub-woofer excitation setup.	109
12.4 Non-uniform and noisy acceleration data due to eigenfrequencies in the system.	109
12.5 Open Circuit* voltage (peak-to-peak) of produced transducer. 110 µm PVDF film. (*($10 M\Omega$) Oscilloscope probes loading the terminals.)	110
12.6 Collapsing output voltage (peak-to-peak) of PVDF transducer. 2 g mechanical excitation @ 33 Hz	111
12.7 Input voltage of LTC-3588 with PVDF transducer connected. High vibration amplitude ($\gg 2.12$ g) with transducer in resonance.	112
12.8 V21BL transducer mounted in shaker. Accelerometer and power manager visible.	112
12.9 Harvested power from V21BL transducer for different amplitudes of vibration.	113
12.10 Maximum achievable output power of V21BL transducer with shaker setup at HiST. No acceleration reference.	113
12.11 V21BL with 50 cent euro-coin glued to transducer tip.	115
12.12 Power output of energy harvester. V21BL transducer with added 50-cent euro-coin to tip	115

List of Tables

3.1	Piezoelectric material properties, averaged values within material "families" [10]	23
5.1	Comparison of battery technologies ^[22]	53
7.1	Geometric parameters	66
7.2	FR4 properties in COMSOL	67
7.3	COMSOL meshing paramters (note variable h_{PVDF} from table 7.1)	70
7.4	Rented EC2 computing node (m2.4xlarge) specifications	71
7.5	Natural frequency (f_n) of modeled V21BL transducer with various end masses placed 15 mm from transducer tip vs. V21BL datasheet specification	73
8.1	Properties of chosen PVDF film ^[32]	78
8.2	Properties of piezoelectric material in V21BL transducer ^[34]	80
8.3	Natural frequency and open-circuit output voltage of V21BL ^[34]	81
9.1	Pinout and signal description of main I/O connector	90

Abbreviations

AC	Alternating Current
ADC	Analog to Digital Converter
CAD	Computer Aided Design
CCM	Continuous Conduction Mode
DC	Direct Current
DCM	Discontinuous Conduction Mode
DOF	Degree of Freedom
EC2	Elastic Computing Cloud
ESR	Equivalent Series Resistance
DFN	Dual-flat No-leads
FEA	Finite Element Analysis
FOM	Figure of Merit
FDM	Fused Deposition Modeling
GPIO	General Purpose Input \Output
HiST	Høgskolen i Sør-Trøndelag (Sør-Trøndelag University College)
GUI	Graphical User Interface
IC	Integrated Circuit
IoT	Internet of Things
KM	Kongsberg Maritime
LabVIEW	Laboratory Virtual Instrument Engineering Workbench
PCB	Printed Circuit Board
PLA	Polylactic Acid
PVDF	Polyvinylidene Fluoride
SDOF	Single Degree of Freedom
SMDS	Spring Mass Damper System

SMPS	Switch Mode Power Supply
SMD	Surface Mounted Device
TEG	Termoelectric Generator
UVLO	Undervoltage Lockout
PWM	Pulse Width Modulation
PZT	Lead Zirconate Titanate
WSN	Wireless Sensor Network

Symbols

a	Acceleration	Meter per square second [m/s^2]
A	Area	Square meter [m^2]
b	Width	Meter [m]
B	Susceptance	Mho [Ω]
c	Damping coefficient	Newton seconds per meter [Ns/m]
C	Capacitance	Farad [F]
d_{xx}	Piezoelectric strain coefficient	Meters per volt [m/V]
E	Electric field	Volts per meter [V/m]
f	Frequency	Hertz [Hz]
F	Force	Newton [N]
g_{xx}	Piezoelectric voltage coefficient	Electric field per stress [E/σ]
h	Height / Thickness	Meter [m]
i	Moment of inertia	Kilograms per square meter [kg/m^2]
I	Current	Ampere [A]
k	Spring constant	Newtons per meter [N/m]
l	Length	Meter [m]
L	Inductance	Henry [H]
m	Mass	Kilogram [kg]
n	Efficiency	Dimensionless
p	Pressure	Pascal [Pa]
P	Power	Watt [W]
Q	Charge	Coulombs [C]
r	Radius	Meter [m]
R	Resistance	Ohm [Ω]
t	Time	Seconds [s]

v	Velocity	Meters per second [m/s]
V	Voltage	Volt [V]
w	Width	Meter [m]
x	Displacement	Meter [m]
X	Reactance	Ohm [Ω]
Y	Young's Modulus (Elastic modulus)	Pascals [Pa]
Z	Impedance	Ohm [Ω]
ϵ	Permittivity	Farads per meter [F/m]
λ	Strain (ΔL)	Dimensionless
ω	Angular frequency	radians per sec [$rads^{-1}$]
σ	Stress	Pascals [Pa]
θ	Angle	Radians [rad]
ζ	Damping ratio	Dimensionless

Part I

Preface

Chapter 1

Introduction

This thesis is written with Kongsberg Maritime (KM) as a business partner. KM is interested in energy harvesting as a step in the further development of instrumentation of maritime vessels and offshore industrial installations, e.g. wind farms. After several meetings discussing what specific direction to take, energy harvesting soon came on the table and KM wanted to investigate into harvesting energy from vibrations utilizing piezoelectricity. The framework of the assignment was very open, but the key points discussed were implementation of a energy harvesting system. As a small side note, focusing on commercialization could be interesting, outlining potential pitfalls and best practices in the development phase.

1.1 Background

In today's society we are already surrounded by wireless electronic devices. Our smart-phones, tablets and laptop computers are as natural as the air surrounding us. Research done by Cisco^[1] in 2011 estimates that as early as 2015 we will have approx. 3.5 connected devices per person (figure 1.1).

A lot of this growth in devices can be contributed to the introduction of wearable electronics like smart watches and glasses^[2], but we will also see an increase in wireless sensors feeding data wirelessly from our surroundings to our existing electronic devices. This new trend in connected devices is often referred to as the "Internet-of-Things" and may have a huge impact on our day-to-day life. Gathering data from the world around us, and even our own bodies, will enable us to understand how the world works in a much more detailed way. Analyzing the gathered data from all these devices can lead

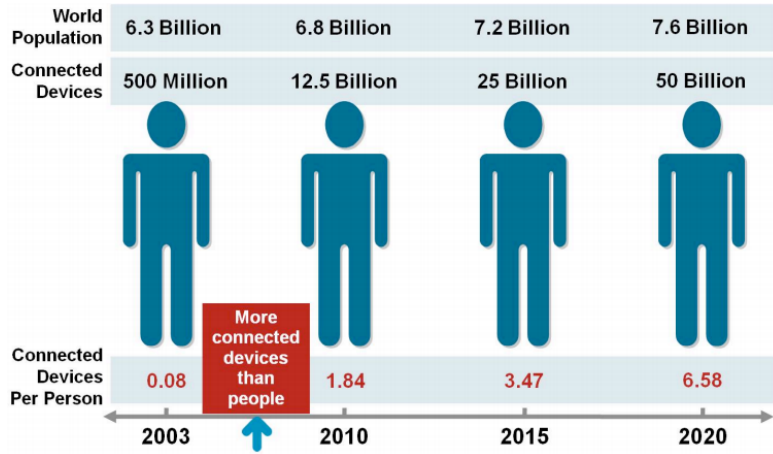


FIGURE 1.1: Wireless devices per person 2003 - 2020 (estimated)^[1].

to an improved understanding of the systems around us and enable us to predict future system behavior, may they be physiological, environmental or industrial.

Wireless Sensor Networks

To achieve all this interconnectivity and data gathering, Wireless Sensor Networks (WSN) play a huge role. They consist of many small electronic devices equipped with a wireless data interface and one or more sensors. These small devices are often referred to as *sensor nodes* and they are often part of large networks of similar devices, measuring their respective parameter(s) and reporting to a central data sink and/or each other.

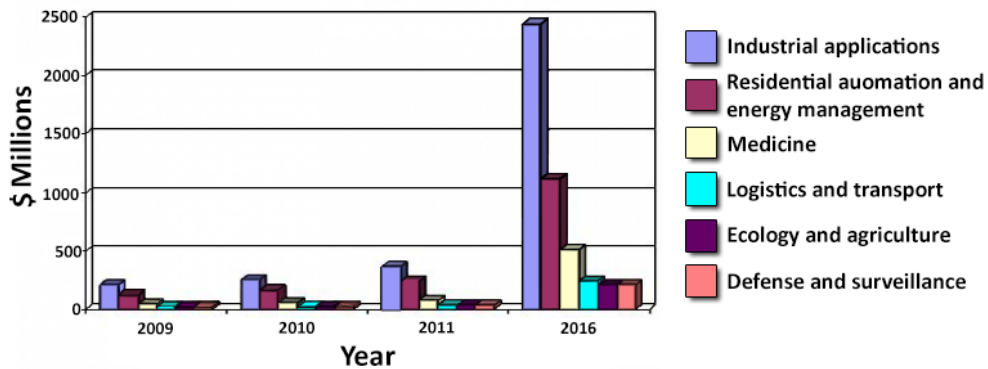


FIGURE 1.2: Predicted value of global market for wireless sensor devices 2009-2016.
Summary figure.^[3]

Predictions tell us (figure 1.2) that the market for WSNs will grow significantly^[3] during the coming years. While the consumer market will see large growth due to home automation, fitness & health devices and increased connectivity of home appliances (IoT), the largest growth is expected to happen in the industrial segment.

In industrial applications WSNs could allow large scale deployment of sensors to critical industrial processes like condition monitoring of engine rooms or wind farms without the need for expensive and intrusive cabled data connections. This can be specially beneficial when reconditioning or improving existing installations with new technology where it might not be possible to add new cables to the installation due to cost, space or even weight restrictions. Even on fresh installations, the cost of the cable and installation process may be many times the cost of the sensor itself. Another benefit of using wireless over wired sensor networks is the possibility for deployment in moving or unreachable areas, e.g. on rotating machinery or engine parts.

Power and alternative energy sources

Powering a wireless sensor node can sometimes be achieved through a cabled connection. This is beneficial when deploying the sensor network in areas where power distributing cables are already installed and easily accessible. This is often not the case in environmental and industrial condition monitoring situations, and battery powered sensor nodes seems to be the mainstream approach.

Even though a lot of work has been put into reducing the power consumption of these devices, in terms of both hardware improvements and more power efficient software algorithms, the battery powered sensor node will eventually deplete its energy source. This may take months or even years, depending on the size of the battery, but eventually the battery will die and the sensor node will be offline until an operator/technician has physically replaced or recharged the battery.

Having personnel travel to the node location can in offshore and maritime applications be an immense cost, and should be avoided as much as possible. To reduce this need for personnel, the energy in the surrounding area of the sensor node should be exploited as much as possible. This energy can be found in solar energy, temperature differences, vibrations, radio waves, wind or even in chemical or biological processes. Utilizing or *harvesting* this energy could reduce or even remove the need for batteries all together and limiting the lifetime to the physical endurance and environmental tolerances of the components in the node.

To reduce the impact of any short term reduction in available energy and avoid downtime, it may be beneficial to combine this energy harvesting with a means of storing redundant power for later use.

Energy harvesting in industrial and maritime environments

In industrial and maritime environments, some energy sources may be more available and consistent than others. Engine rooms are often sealed off and sheltered from exposure to the sun or the wind. This means that we are often limited to the ambient energy generated by the industrial processes themselves, like thermal or vibrational energy.

Thermal energy can be exploited where there is a temperature gradient by thermoelectric generators (TEGs) containing dissimilar conductors utilizing the *Seebeck* or *Peltier* effect. Another means of exploiting temperature gradients is through taking advantage of the pyroelectric effect found in some materials. This effect is *closely* related to the piezoelectric effect and requires an alternating temperature difference to produce electric power. One of the main disadvantages of thermal energy harvesting is the limited placement opportunities of the harvesting devices. They need to be mounted in the close vicinity of the temperature gradient, e.g. on the surface of the hot pipe or machinery part. One big advantage is that thermal energy harvesting can be achieved with no moving parts and no exhaustible materials or chemicals which makes it a candidate for long operational lifetime.

Vibrational energy is often more distributed in the local environment, e.g. the vibrations from the engine of a large maritime vessel can sometimes propagate throughout the whole hull with constant frequency, but varying amplitude. This means more freedom when deploying the energy harvester(s). The characteristics of these vibrations are discussed in chapter 2.

These vibrations have a lot of energy, and harvesting them using e.g. a piezoelectricity could enable a WSN-node to be powered from ambient energy with flexibility regarding placement. As with TEGs, piezoelectric energy harvesting can be achieved without expendable materials or chemicals.

1.2 Objectives

The objectives in this project is to build and test a system for harvesting vibrational energy and turning it into usable electric energy. The system will be mainly aimed at industrial or maritime applications where the frequency of vibrations can be quite low (< 100 Hz). This implementation can be divided into three main parts;

Model and build piezoelectric transducers aimed at low frequency industrial environments.

Develop an electronic device capable of managing the power generated from the transducer, and also incorporate any long-term power storage.

Building a suitable casing for the system to allow it to be installed / mounted in a industrial/maritime environment is also an important part of this project.

1.3 Scope

Based on the introduction, background and objectives listed this thesis has several topics to discuss. To model the piezoelectric transducers, a model must be developed. Taking into account as many physical parameters as possible. Once this model is complete, transducers can be built in respect to the model output. To interface this transducer, the power manager must be able to optimize the power extraction and implement storing 'excess' power. The power manager must also be efficient in terms of low operating power, and the electronic design in general must be approached with regards to low leakage. The casing of the transducer and electronics should enable the system to be tuned at installation to increase flexibility.

1.4 Concrete and verifiable goals

In this thesis, the following goals can be specified:

- Develop model for estimating the behavior and power output of a piezoelectric transducer and compare to a real system.
- Investigate currently available devices (Integrated Circuits) capable of managing the raw transducer output and discuss potential improvements to these devices.
- Investigate the possibility of long term energy storage in energy harvesters.
- Implement and test a piezoelectric energy harvesting system.

1.5 Outline

Part 1: Part one contains the preface of this document. It includes introductory chapters and objectives.

Part 2: Part two of this document contains the theoretic foundation for understanding the different parts of the system.

Part 3: Part 3 contains the modeling and methodology chapters. It explains the tools and approaches used at implementation and development of the FEA-model of the transducer.

Part 4: Part 4 involves implementation. In this part, all the implementation done in this project is documented and explained.

Part 5: This part includes the results, discussion and conclusion of the report.

Part 6: This part contains all appendices to the report.

Part II

Theory

Theory

This part of the thesis will discuss the different aspects of the energy harvester, from characteristic vibrations in maritime industrial environments, to energy extraction and storage. Figure 1.3 shows the energy flow in typical piezoelectric energy system.

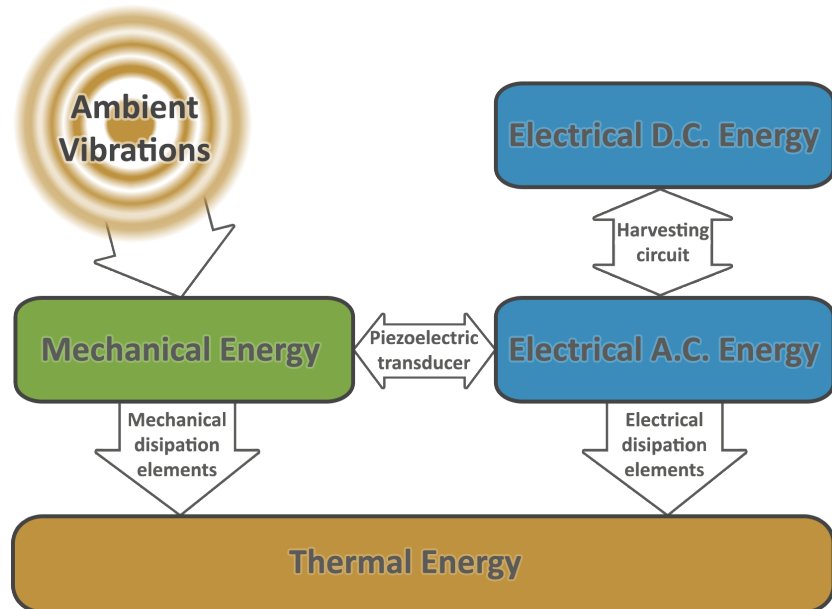


FIGURE 1.3: Energy flow in piezoelectric energy harvesting system^[4]

Chapter 2

Vibration characteristics

As mentioned in the *introduction*, this thesis will focus on harvesting ambient vibrational energy in maritime environments. In this chapter the distribution of this energy within a large maritime vessel will be discussed in terms of excitation frequency, harmonic frequencies and amplitude.

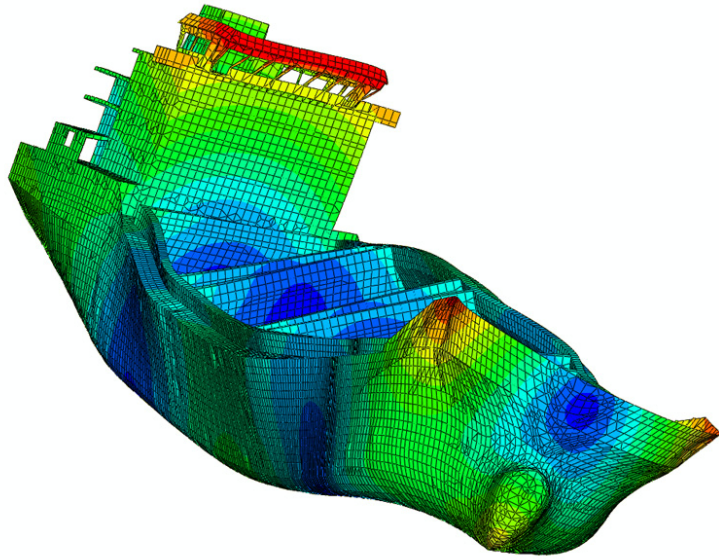


FIGURE 2.1: Exaggerated visualization of natural frequencies and mode shapes in ship hull^[5].

Mechanical vibrational excitation in maritime vessels can originate from a multitude of sources. Some of them are^[6]:

- The main engine
- Shaft-line dynamics
- Propeller radiated pressures and bearing forces
- Air conditioning systems

- Transverse auxiliary engines
- Cargo handling and mooring machinery
- Vortex shredding mechanisms
- Intakes and exhausts
- Slamming phenomenas

Many of these sources are non-constant e.g. cargo handling, slamming phenomenas and auxiliary engines, and cannot be counted as the main source of vibration for energy harvesting. More constant sources of vibration must be used.

The vibration from the main engine will be present as long as it is running, and once the vessel is moving (propeller engaged), excitation from the shaft-line, propeller and subsequent bearings will come into play. The engine speed together with the hull dynamics will classify the vibration frequency and amplitude in different parts of the ship. These more constant vibrations are a good candidate for our energy harvesting solution.

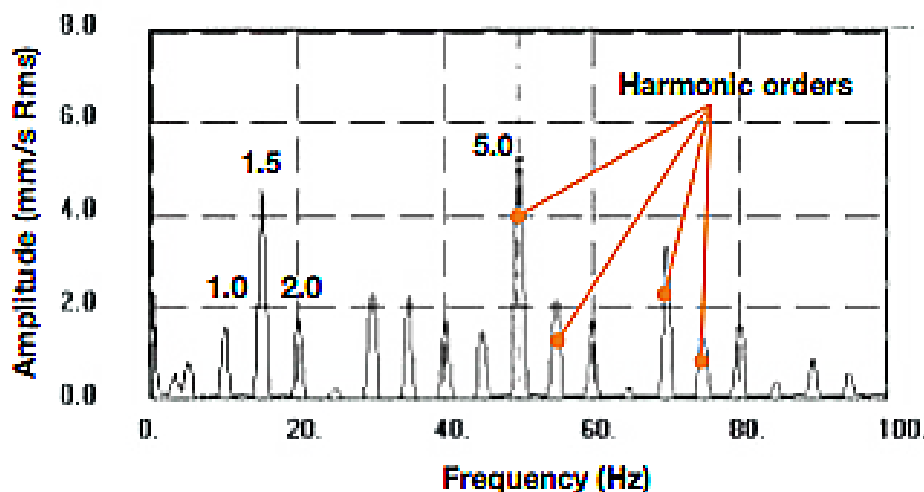


FIGURE 2.2: A typical vibration spectrum measured from a running 4-stroke diesel engine (Wärtsilä 6L46F)^[7]

Figure 2.2 shows a typical vibration spectrum of a 'low speed' 4-stroke diesel engine (the Wärtsilä 6L46F) running at 600 rpm^[7], which translates to 10 Hz. At this frequency the amplitude of the vibrations coming directly from the engine's speed can be seen. This is the 1st harmonic frequency (marked by a '1' in the figure). The harmonic frequencies ('2' and '5') are also visible, and because of the four-stroke engine configuration, even the *half-order* harmonics ('1.5')^[7] are present. One very interesting aspect of this frequency distribution is that the engine's running frequency (10 Hz) is not where the biggest vibrational amplitude is. Much more energy exist in both the 1.5 and 5th harmonic frequencies at 15 and 50 Hz.



FIGURE 2.3: The Wärtsilä 6L46F 4-stroke 7200 kW diesel engine.

This is beneficial when designing an energy harvester in several ways. The largest advantage is that even though the engine is 'low speed', the most dominant vibrations generated may be of much higher frequency (5 times for the 5th harmonic) than the speed of the engine. This may make things easier when dimensioning energy transducers. Another important observation is that there are multiple frequencies with large energy spikes. This can bring flexibility when designing the energy harvester and might justify having several transducers tuned to each peak in the power spectrum.

These observations may change from ship to ship and from engine to engine and suggests that thorough data gathering and analysis should be performed before designing or deploying an energy harvesting system to a maritime vessel or any other environment.

Chapter 3

Piezoelectricity

A piezoelectric material is a material that produces a voltage when introduced to mechanical strain or stress (the *direct* piezoelectric effect). This effect is reversible, causing the material to change its physical form when introduced to an electric field (the *inverse* piezoelectric effect) (fig. 3.1). This chapter will give a short introduction to these effects and lay the foundation for later work with piezoelectric materials.

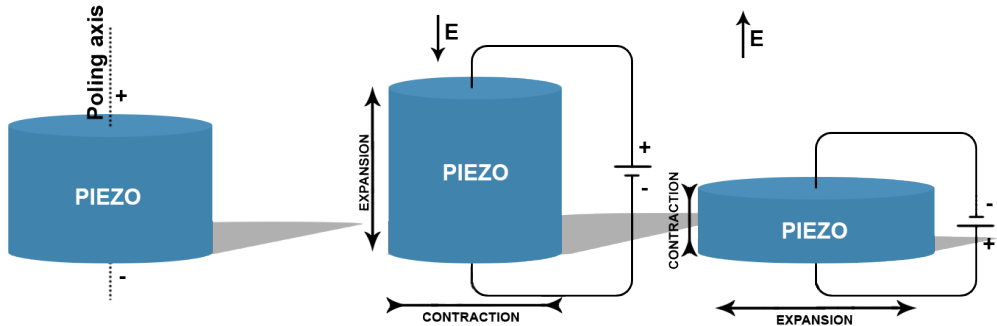


FIGURE 3.1: The inverse piezoelectric effect

3.1 Piezoelectric axis nomenclature and parameter notation

When working with piezoelectric materials, the focus is on stress, strain or voltage potentials in different directions in the materials. This has led to a standardization of nomenclature for axis and directions as figure 3.2 tries to illustrate. The polarized axis ('Z' in fig. 3.2) is always denoted as direction 3, while the X and Y axis are more loosely denoted as either 1 or 2. Additionally, rotation around these axis are described as 4, 5 and 6 as shown in the figure, and can be used to describe a twisting effect in the piezoelectric material.

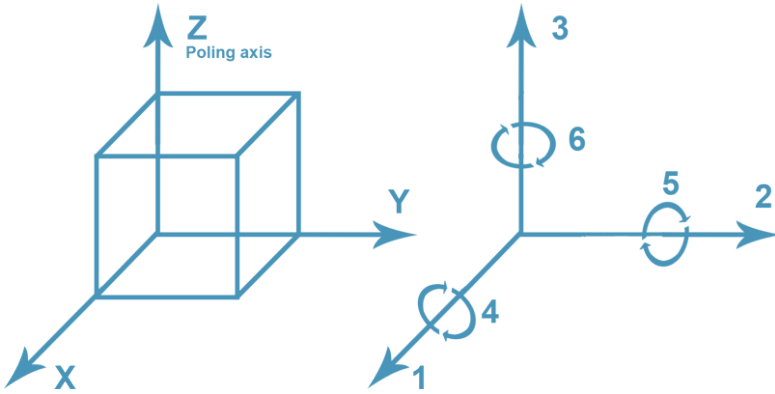


FIGURE 3.2: Common nomenclature for axis and dimensions of piezoelectric materials

Notations in piezoelectrics often use this axis/direction nomenclature to describe the different parameters and the relationship between mechanical and electrical properties. An example can be seen below:

$$g_{ab}$$

In this example the sub notations 'a' and 'b' refer to the directions of the different effects inherent in the piezoelectric voltage coefficient 'g'. 'a' is the direction of the electric effect while 'b' is the direction of the mechanical effect.

E.g. "g₃₁" means the piezoelectric voltage coefficient with induced electric field in direction 3 per unit stress applied in direction 1 OR induced strain in direction 1 per unit electric displacement applied in direction 3.

3.2 Piezoelectric coefficients

In applications where piezoelectric materials are utilized, the goal is usually to try to convert mechanical energy into electrical energy, or electrical energy into mechanical energy. The rate and efficiency of the energy conversion in a piezoelectric material, can often be described by the elementary piezoelectric coefficients:

- Strain coefficient d
- Voltage coefficient g

These coefficients are specific to each material, and can enable us to calculate the expected outcome of an applied electrical, or mechanical force. The strain coefficient (d) and

voltage coefficient (g) relates the electrical and mechanical properties in the material. These coefficients can be interpreted differently based on whether the direct or inverse piezoelectric effect is being utilized^[8].

For the *direct* piezoelectric effect (mechanical to electrical) ^[8]:

$$d = \frac{\text{Short circuit charge density}}{\text{Applied mechanical stress}} \quad [C/m^2] \quad [N/m^2] \quad [C/N]^1 \quad (3.1)$$

$$g = \frac{\text{Open circuit electric field}}{\text{Applied mechanical stress}} \quad [V/m] \quad [N/m^2] \quad [Vm/N] \quad (3.2)$$

For the *inverse* piezoelectric effect (electrical to mechanical) ^[8]:

$$d = \frac{\text{Strain developed}}{\text{Applied electric field}} \quad [m/m] \quad [V/m] \quad [m/V] \quad (3.3)$$

$$g = \frac{\text{Strain developed}}{\text{Applied charge density}} \quad [m/m] \quad [C/m^2] \quad [m^2/C] \quad (3.4)$$

In this document, the focusing is on energy harvesting from vibrations. This means converting mechanical energy into electrical energy and thus, the '*direct*' interpretation of the piezoelectric coefficients will be used.

The piezoelectric coefficient is often accompanied by the Piezoelectric coupling coefficient (k). This coefficient gives an indication of the energy loss in the material. For mechanical to electrical conversion it can be defined as^{[9][10]}:

$$k = \sqrt{\frac{\text{Electrical energy stored}}{\text{Mechanical energy applied}}} \quad (3.5)$$

Simplified, this means that the charge density in a piezoelectric material when approaching short circuit conditions can, when electrodes are placed in the 3-dimension, be given by^[9]:

¹The strain coefficient can often be expressed as pico-Coloumbs per Newton ([pC/N])^[9].

$$D = \frac{Q}{A} = k_{3n}d_{3n}\sigma_1 \quad [C/m^2] \quad (3.6)$$

Where:

- D is the developed charge density
- A is the area of the conductive electrode
- k is the piezoelectric coupling coefficient
- d is the piezoelectric strain coefficient
- n axis of applied mechanical stress
- σ_n Applied stress in the relevant direction

When open circuit conditions apply, the output voltage of the piezoelectric material can be found using the *simplified* expression below^[9]:

$$V_o = k_{3n}g_{3n}\sigma_n t \quad [V] \quad (3.7)$$

Where:

- V_o is the output voltage
- k is the piezoelectric coupling coefficient
- g is the piezoelectric voltage coefficient
- n axis of applied mechanical stress
- t Thickness of piezoelectric material

3.3 Piezoelectric materials

The unit cell of a material is the smallest repeating unit in its material structure. If this unit cell has a net non-zero charge it means that each cell acts as a dipole. This is visualized in a polarized perovskite cell in figure 3.3. The figure shows that the four calcium and oxygen ions are distributed in way that cancel each others charge out. In the middle however, there is an offset titanium ion which disrupts the charge balance of the cell and gives it a total net charge.

If a mechanical stress is applied to the unit cell, changing its dimensions will also change the offset of the charged ion, thus generating a varying electric field.

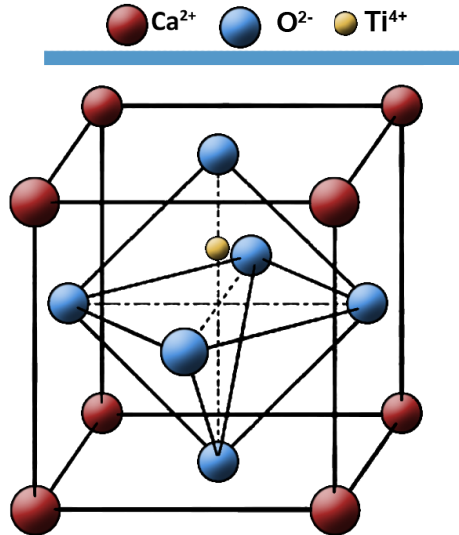


FIGURE 3.3: Unit cell of perovskite crystal structure

In a monocrystalline crystal structure, all these unit cells will be facing the same way and thus contributing their dipole in the same direction. For polycrystalline structures on the other hand, the dipoles may only be aligned in small areas called grains which are randomly oriented in the material. In these cases, the effect of the dipoles can to a large extent cancel each other out. This is often the case for synthetic materials which needs to be polarized before displaying piezoelectric behavior.

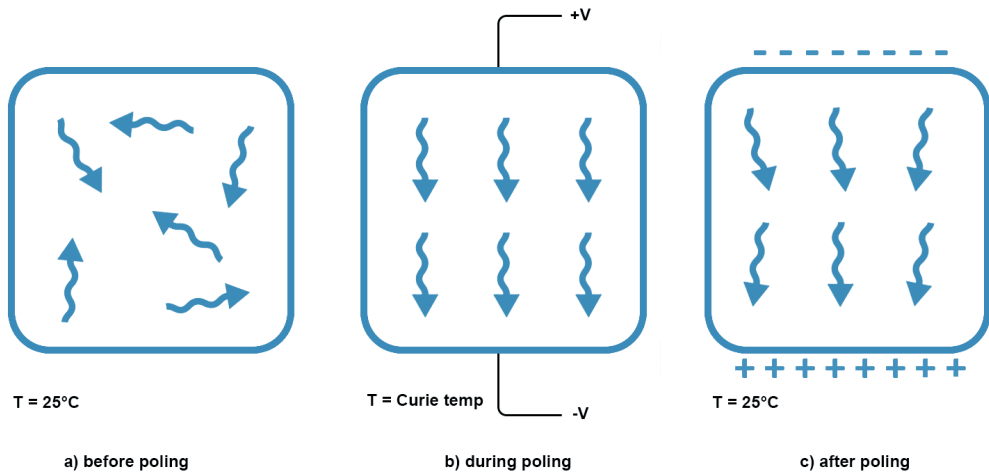


FIGURE 3.4: Polarization of ceramic polycrystalline structure

Figure 3.4 shows the polarization process for a polycrystalline ceramic piezoelectric material. 3.4 a) shows the randomly oriented crystal grains before the polarization process. In b) the material is heated up to its *curie temperature* and having a high voltage applied to each side. This aligns the crystal grains. The temperature is then lowered below the curie point while still applying the voltage (c). Once the material is

cooled, the voltage source is removed, and the crystal grains keeps *most* of its alignment and the material now has a non-zero net charge.

Lead Zirconate Titanate (PZT) is one of the most widely used piezoelectric materials. It has a perovskite crystal structure (fig. 3.3), but is built up from Lead (Pb), Zirconium (Zr), Oxygen (O) and Titanium (Ti). It is a ceramic material and many variations of the material exists.

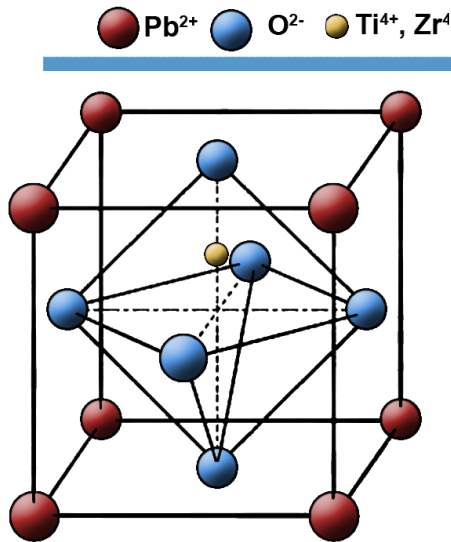


FIGURE 3.5: Unit cell of Lead Zirconate Titanate (PZT)

The piezoelectricity of PZT is as described earlier connected to the net charge of the dipole unit cells. When applying a mechanical pressure to the material, the dimension change along with the offset of the single ion which produces an electric field in the material.

Polyvinylidene Fluoride (PVDF) is another widely used piezoelectric material. One of the main differences from PZT is that PVDF is a polymer (plastic) material. This means it has a very different structure than the ceramic PZT which is illustrated in figure 3.6.

PVDF consists of long chains of carbon molecules with fluoride and hydrogen appendices (CH_2CF_2). When a longitudinal force stretches the material, the change in length and thickness also changes the electric field between the charges which generates a charge on the material surface.

3.3.1 Selecting the best material

Figuring out what material most suitable for energy harvesting applications can be hard. Several approaches for determining the best energy harvesting material can be used. Figure of Merit (FOM) is one of them.

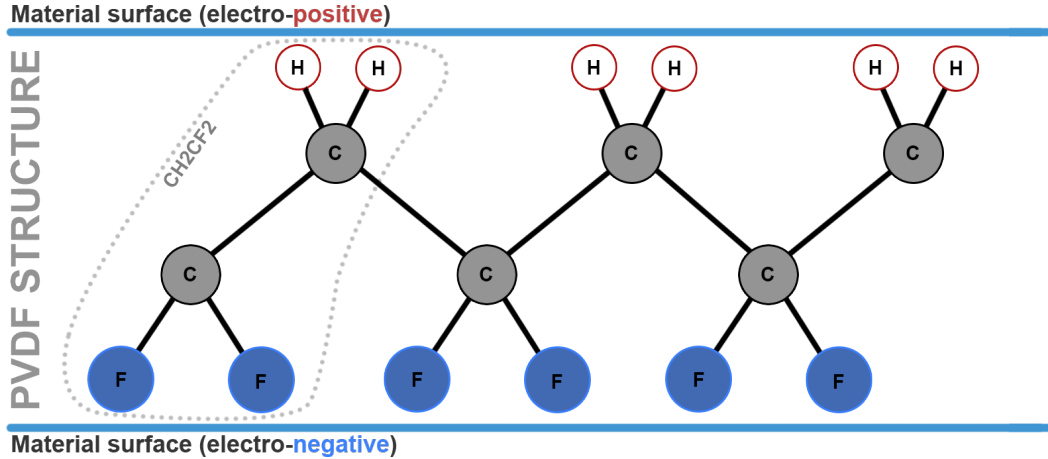


FIGURE 3.6: Structure of Polyvinylidene Fluoride (PVDF)

The FOM is calculated as the product of the piezoelectric strain and voltage coefficients. The idea is that since the strain coefficient (d) is related to the short-circuit current and the voltage coefficient (g) is related to the open-circuit voltage, multiplying these will give an indication of the possible output power^[10] ($P = VI$). Since these coefficients are based on two different circuits (open and closed) it is not a realistic measure of power, but can give and indication on the theoretical maximum power output^[10].

$$\text{FOM} = g \times d \quad (3.8)$$

Daniels et al.^[10] discusses different approaches to selecting the best piezoelectric material based on the piezoelectric coefficients (d and g), elastic modulus(Y), piezoelectric coupling (k), FOM and relative dielectric constant (ϵ_r).

Material	Y_{31} $\times 10^9 [N/m^2]$	$ d_{31} $ $\times 10^{-12} [m/V]$	$ g_{31} $ $\times 10^{-3} [Vm/N]$	ϵ_{r33}^T	k_{31}	FOM $\times 10^{-12}$
PVDF	3	20	188	12	0.11	3.76
HARD PZT	85	115	11.3	1204	0.30	1.30
SOFT PZT	64	252	9.6	3115	0.39	2.42

TABLE 3.1: Piezoelectric material properties, averaged values within material "families"^[10]

Their study^[10] show that the elastic modulus (Y) has little correlation to power output for all tested materials (table 3.1). The strain coefficient (d) was found to have more influence over power output than other properties, but the FOM showed a more linear correlation to generated power. In a situation where materials with similar strain coefficients were to be compared, the material with the lowest relative dielectric constant (ϵ_r) was found to be the most favorable^[10]. The study concluded that no 'best parameter' for

material evaluation in energy harvesting applications could be found, but a combination of FOM and the strain coefficient would give an indication of the best power output.

Looking at table 3.1 both the PZT type materials have a high d value, while the FOM of PVDF is somewhat higher than for the PZTs. No obvious winner can be made from the represented materials, but 'SOFT PZT' shows a high d and also a quite high FOM compared to the other two and would be a good candidate for energy harvesting. Given its low d , PVDF might be the least suited of the three.a

3.4 The piezoelectric transducer

The type of piezoelectric transducer discussed in this document is of the "cantilever beam" type. In this configuration, the transducer is shaped like a beam with one end fixed to a base while the other end is free to move (see fig 3.7). An extra mass (m) may be fixed to the free end in order to manipulate the behavior of the beam in such a way which would be impractical or impossible to achieve by modifying its length (L), width (b) or thickness (h).

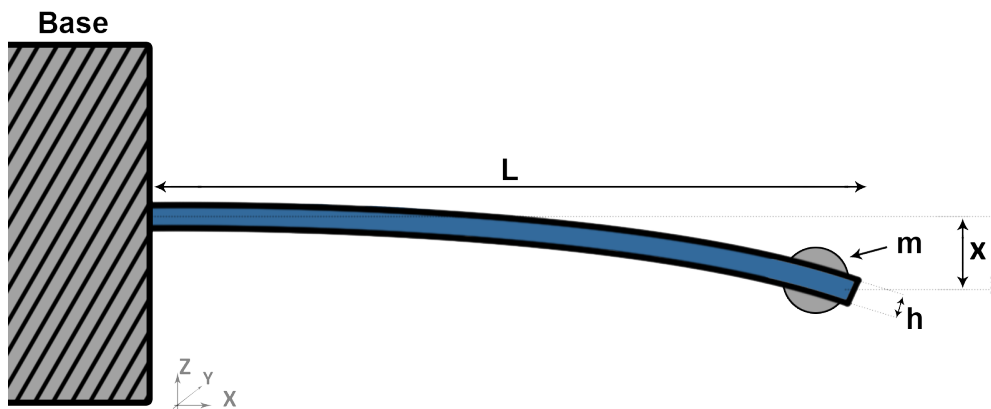


FIGURE 3.7: Cantilever beam

When the base of such a transducer is introduced to mechanical excitation, the inertia of the beam structure causes a stress in the beam material. as seen in section 3.2 applying stress to a piezoelectric material causes charge and voltage to be developed on its terminals. This means that the transducer can be viewed as a high impedance power source, delivering an A.C. power to the load with the same frequency as the mechanical excitation.

The following sections will focus on understanding the piezoelectric cantilever beam transducer from both a mechanical and electrical point of view.

3.4.1 Beam composition

Before we go in depth on the mechanical and electrical behavior of the transducer we need to take a brief look at the material composition in the device. The piezoelectric cantilever beam transducer is made up of several parts. The most important part is the actual layer of piezoelectric material and its electrodes which makes its electrical output externally available. Additionally there is often a layer added for mechanical support. This enables the behavior of the beam to be characterized not only by the piezoelectric material itself, but with large contributions from this support layer.

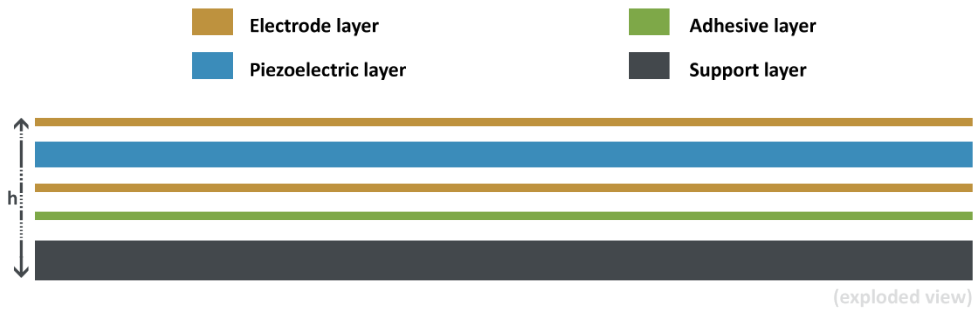


FIGURE 3.8: Piezoelectric cantilever beam transducer composition (exploded view)

The electrodes are often adhered to the piezoelectric material through some sort of metal depositing technique, but the adhesion between the electrode layer and support layer may require an adhesive like epoxy or equivalent. In very thin transducer geometries, the thickness of this adhesive layer and the thickness of the deposited metallic electrodes could affect the overall behavior of the transducer. In this report they will be assumed to be much thinner than the piezoelectric layer and support layer, thus allowing them to be neglected.

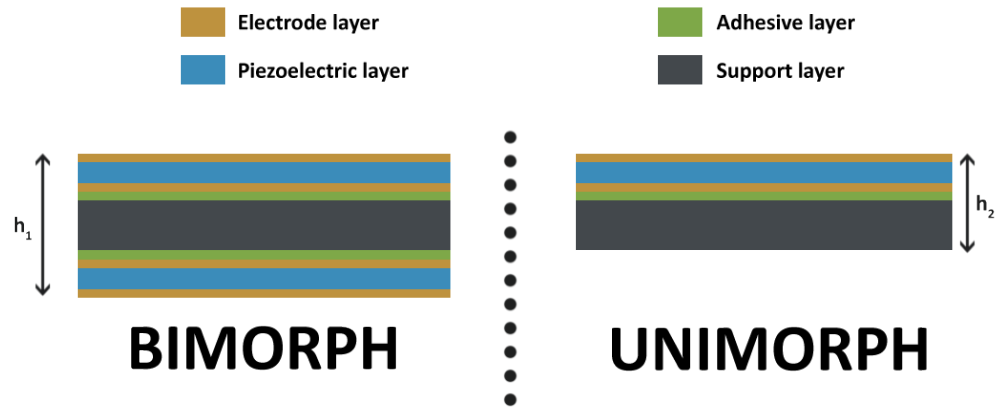


FIGURE 3.9: Comparison of bimorph and unimorph transducer

The illustration in figure 3.8 shows a *unimorph* transducer. A very similar configuration is the *bimorph* transducer which has a piezoelectric layer on both sides of the support

layer. This means we can double the amount of active (piezo) materials without doubling the volume of the transducer. This could theoretically yield a higher power density (W/m^3) than the unimorph type, making bimorph transducers more suitable for energy harvesting applications. A visual comparison of the unimorph and bimorph transducers can be seen in figure 3.9.

A problem that can quickly arise when working with structures composed of different materials is how to define its elasticity. Since there are two or more materials with different elastic moduli, the values need to be combined into a modulus representing the composite structure as a whole. The most accurate approach would be to develop an algorithm which takes into account not only the different elastic moduli, but also the inherent crystal and/or texture symmetries like the Voight and Reuss bounds^[11]. If no information about these structures and symmetries are available, a simplified weighted mean approach can be used instead. The elastic modulus for the composite beam (Y_c) with n different materials can then be found by equation 3.9, where Y is the elastic modulus and V_f is the volume fraction² of the n -th material.

$$Y_c = \sum_{i=1}^n V_{f_i}(Y_i) \quad (3.9)$$

This approach would not be applicable if the transducer layer stack would change significantly along the transducer length (l).

3.4.2 Mechanical behavior

In this section the behavior of the piezoelectric cantilever beam transducer will be investigated from a mechanical viewpoint. To simplify things, a single degree of freedom (SDOF) system can be assumed where the beam only flexes around the Y-axis, or put in other terms, tip deflection only occurs in the Z-axis (referenced to figure 3.7 on page 24). This simplification means that a lot of parameters that would normally require a tensor expression, e.g. the piezoelectric and coupling coefficients, can be expressed as scalars.

²The volume fraction of a material is the fraction of the total structure volume held by the respective material. ($V_f = V_{mat}/V_{tot}$)

Deflection

Beam deflection is caused by an external applied force. Looking back at figure 3.7 on page 24 we see the deflection (x) caused by an end mass (m) and the gravitational acceleration g .

To find the deflection (x) when a force (F) is applied to the transducer tip, the following equation can be utilized^[12]:

$$x_{max} = \frac{FL^3}{3YM} \quad (3.10)$$

Here, x is the tip deflection, F is the force acting on the beam tip, L is the length of the beam, Y is the elastic modulus and M is the beams moment of inertia. The moment of inertia (M) can be found utilizing equation 3.11^[12] where b is the beam width and h is the beam thickness.

$$M = \frac{bh^3}{12} \quad (3.11)$$

Spring Mass Damper System

The SDOF cantilever beam transducer can be viewed as a spring mass damper system, defined by a spring, a mass and a damper. The spring and mass is characterized by the geometry and material properties of the transducer while the mechanical connection between transducer and base, material properties and viscosity of the surrounding media (air) defines the damping.

Hooke's law^[13] describe how much force (F) is needed to stretch a spring with spring constant k a distance of x :

$$F = kx \quad [N] \quad (3.12)$$

Rearranging and inserting equation 3.10 and 3.11 yields:

$$F = k \left(\frac{FL^3}{Y3I} \right) \quad (3.13)$$

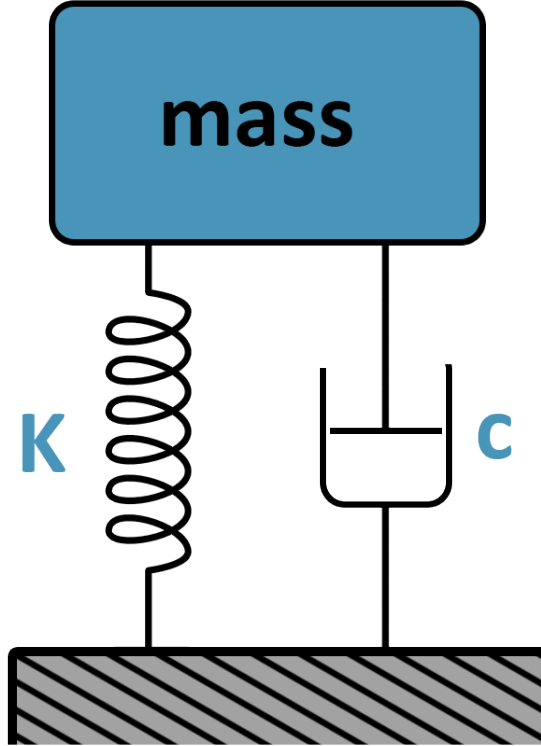


FIGURE 3.10: Illustration of SMDS.

$$k = \frac{3Y \left(\frac{bh^3}{12} \right)}{L^3} \quad (3.14)$$

The damping of the cantilever beam is a force acting in opposite direction of an proportional to the speed of the transducer. It is defined by the damping coefficient (c) and expressed as:

$$F_c = -cv \quad (3.15)$$

... and since speed is the derivative of distance^[13] it can be rewritten.

$$F_c = -c \frac{dx}{dt} \quad (3.16)$$

$$c = -F_c \frac{dx}{dt} \quad (3.17)$$

Unlike the spring constant, the dampening coefficient (c) can be hard to determine. There are many different physical effects contributing to the damping, and calculating an exact value be almost impossible.

Some effects contributing to the damping of a cantilever beam transducer:

- Viscosity of surrounding media (air, water etc.)
- Fixing mechanism between beam and base
- Friction against external components
- Friction between internal material structures

If the damping coefficient can be determined, the *damping ratio* (ζ) from the mass (m) and spring constant (k) is given by equation .

$$\zeta = \frac{c}{2\sqrt{mk}} \quad (3.18)$$

There are generally four modes of damping which defines the *step-response* (releasing the system from deflected state at $t=0$) of the system.

- **Over damping** ($\zeta > 1$): The system return to its initial position without overshoot (no oscillation). The time needed to return is defined by the magnitude of damping ratio ζ .
- **Critical damping** ($\zeta = 1$): The system returns to its initial position without overshoot (no oscillation) as quickly as possible.
- **Under damping** ($0 < \zeta < 1$): The system oscillates around the initial position, slowly reducing its amplitude until finally coming to a stop.
- **No damping** ($\zeta = 0$): The system oscillates at its natural frequency f_n forever.

Without knowing much about the system parameters, in non-ideal conditions (the real world) and high viscosity surrounding media (air), the expected damping type is *under damping*.

$$0 < \zeta < 1$$

From the spring constant and system mass the (undamped) natural frequency, f_n , of the transducer can be found. This is the frequency at which the system would oscillate with no damping ($\zeta = 0$).

$$f_n = \frac{1}{2\pi} \sqrt{\frac{k}{m}} \quad (3.19)$$

Frequency response

Now that the defining parameters of the system (m , k and c) are known, investigation into the frequency behavior of such a SMDS can be done. The system behavior can in general be defined as *Forced vibration with damping* since the transducer base is 'forced' by external excitation.

Summing up the different forces in the system to find the total force (F) acting on the system.

$$F_{mass} + F_{damper} + F_{spring} = F_{tot} \quad (3.20)$$

$$ma + cv + kx = F \quad (3.21)$$

... where a is the acceleration, v is the velocity and x the tip-displacement of the system. Redefining the expressions around x gives a second-order differential equation describing the behavior of the system:

$$m \frac{d^2x}{dt^2} + c \frac{dx}{dt} + kx = F \quad (3.22)$$

To simplify things, the system can be defined as *steady state*. This means that all transient behavior is ignored and the system is considered to have constant applied force and frequency. Doing this simplifies things and allows solving the equation using its steady-state solution^[14]:

$$x(t) = X \frac{F}{k} \cos(\omega t + \phi) \quad (3.23)$$

In this representation, X is the magnitude factor of the displacement $x(t)$ and is defined by exitation frequency, damping ratio and natural frequency of the system^[14].

$$X = \frac{1}{\sqrt{(1 - (\frac{f}{f_n})^2)^2 + (2\zeta \frac{f}{f_n})^2}} \quad (3.24)$$

The phase shift is another important factor, and can be expressed as^[14]:

$$\phi = \arctan \left(\frac{2\zeta \frac{f}{f_n}}{1 - (\frac{f}{f_n})^2} \right) \quad (3.25)$$

Combining these expressions in a MATLAB-script (Appendix VI) enables plotting the amplitude of deflection with different frequency of exitation (vibration) and damping ratios.

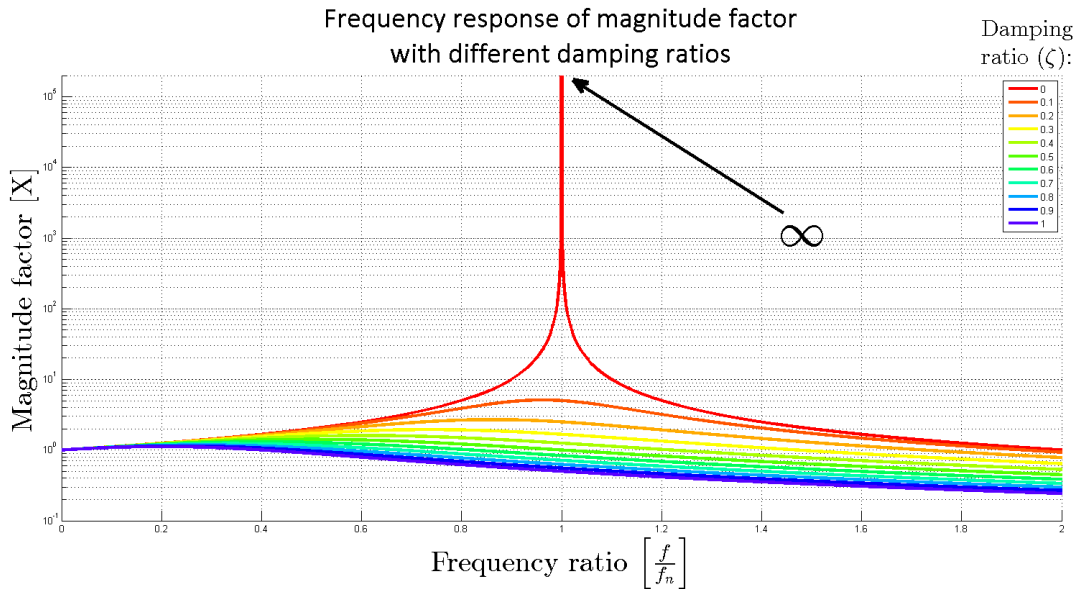


FIGURE 3.11: Frequency response of magnitude factor

Looking at the resulting figure 3.11 and equation 3.23, it is clear that the amplitude of deflection is very frequency dependent. With no damping ($\zeta = 0$), the magnitude factor is infinitely high and extremely narrow banded. This is not possible to achieve in the real world, some air resistance of internal material friction *will* contribute to the damping factor to some degree. Looking at the magnitude factor with a damping ratio of 0.1, the magnitude is severely decreased compared to no damping and that a more broad banded response is achieved. As the damping ratio increases further, the magnitude of

deflection decreases and for a energy harvesting application where displacement and by extension, deflection is important to achieve a high energy output, it would be beneficial to keep the damping ratio as low as possible. Care should still be taken to design the system in such a way that the transducer device is not exposed to more stress than it is capable of handling without taking permanent damage.

Stress and Strain

On page 19 it was shown that the voltage and developed charge in the piezoelectric material is proportional to the stress developed in the material.

Strain describes the deformation of a material in response to an applied force and has no unit. It is merely a factor of elongation in a material in one or more directions^[13].

$$\lambda = \frac{L - L_0}{L_0} \quad (3.26)$$

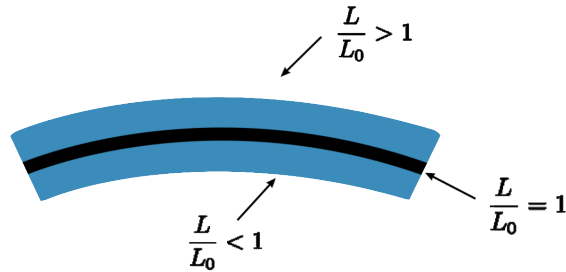


FIGURE 3.12: Strain distribution in bending body

In eq. 3.26 , strain (λ) is expressed in terms of length (L) and initial length (L_0). This stretching in the length direction is directly related to the deflection of the beam, and its thickness. Figure 3.12 shows that the length increases on the *outer* side of the bend and decreases on the *inner* side.

$$Y = \frac{\sigma}{\lambda} \quad \rightarrow \quad \sigma = Y \times \lambda \quad \rightarrow \quad \lambda = \frac{\sigma}{Y} \quad (3.27)$$

Translating strain and stress is easily achieved using Young's modulus (Y)^[13] (eq. 3.27).

3.4.3 Electrical behavior

From an electrical point of view, the piezoelectric generator can be represented by a simplified electrical circuit (thevenin equivalent).

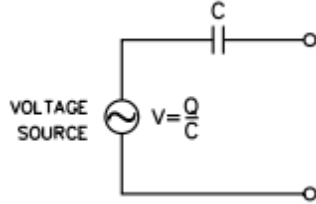


FIGURE 3.13: Simplified thevenin-equivalent circuit of piezoelectric generator with voltage source^[9].

Figure 3.13 shows the equivalent circuit of a piezoelectric material as a voltage source and a series capacitance. The series capacitance is a result of the permittivity (ϵ), area (A) and thickness (h) of the material and can be expressed as^[15]:

$$C = \epsilon \frac{A}{h} = \epsilon_r \epsilon_0 \frac{lw}{h} \quad (3.28)$$

The voltage source is defined as the generated charge (Q) over the series capacitance (C)^[9]^[15].

$$V = \frac{Q}{C} \quad (3.29)$$

This is a very simplified representation of the piezoelectric generator. In addition to the series capacitance, there are parallel and series resistances representing leakage due to inherent material imperfections, but these can often be neglected when working at low frequencies.

From this equivalent circuit we see the the main characteristic feature of the source impedance, the capacitance. Its contribution to the source impedance can be expressed as^[15]:

$$Z_{SOURCE} = X_C = \frac{1}{2\pi f C} \quad (3.30)$$

Plotting eq. 3.30 over frequency (f) (fig. 3.14) we see that for low frequencies the impedance is very high and at D.C. it is infinite. This means that no DC current can flow from the generator. Another important observation is that the impedance changes with frequency which can affect the way we extract the generated power.

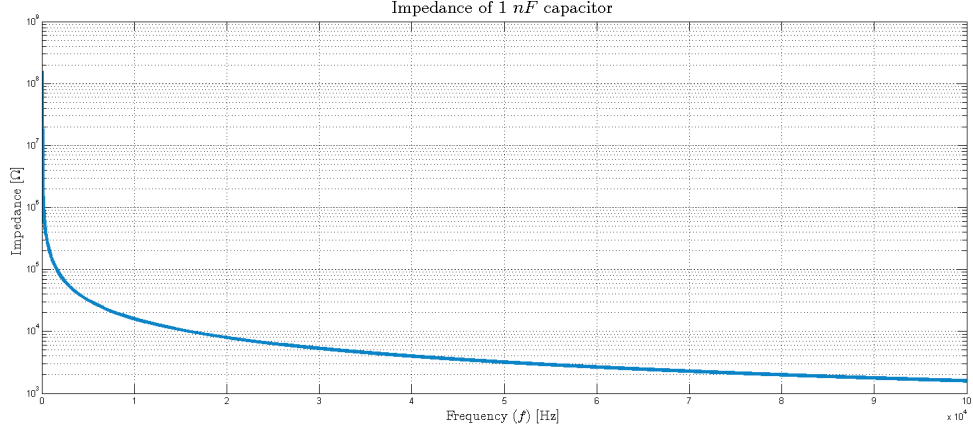


FIGURE 3.14: Impedance of capacitor over frequency.

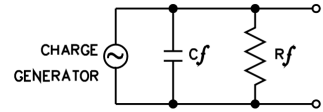


FIGURE 3.15: Simplified Norton-equivalent circuit of piezoelectric generator with current source^[9].

Another popular representation of the piezoelectric generator is a current source in parallel with the material capacitance (Norton equivalent) seen in figure 3.15. Here, both the piezo-capacitance (C_f) and internal resistance (R_f) is included.

Chapter 4

Power management

The output impedance of any piezoelectric transducer device will be defined by its physical size alongside the specific properties of its material(s) and structure. When trying to transfer power from any electric source, its impedance plays a huge role in how much power can be extracted and how to extract it. This chapter talks about this impedance, and what considerations needs to be taken to ensure the best possible energy harvesting application.

4.1 Maximum power vs. Efficiency

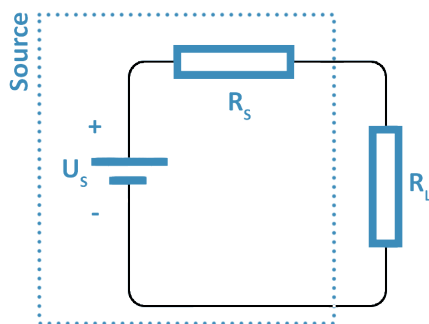


FIGURE 4.1: DC source and load resistance

When working with most energy harvesting systems, it is very important to differentiate between maximum power and maximum efficiency. For systems with a specific and limited amount of power, e.g. battery operated systems, efficiency is often a key factor. In these applications it is important to use the available power as efficiently as possible. To achieve maximum efficiency, it is key to dissipate as little power as possible within the power source.

For many energy harvesting applications efficiency is not important, but rather maximum power transfer. The energy produced by a piezoelectric cantilever transducer is very volatile and is not accumulated in the transducer. This means that as much power as possible should be extracted when it is available in the transducer.

4.1.1 DC-power applications

For DC-power applications the efficiency (η) of any power transfer from a source to a load can be given by equation (4.1)^[15].

$$\eta = \frac{R_L}{R_L + R_S} \quad (4.1)$$

Plotting η as the ratio of R_L to R_S in figure 4.2 is changed, two key features can be recognized. The first thing is that when the resistances are the same ($R_L = R_S$), the efficiency is 50%. This means that an equal amount of power is dissipated in the loads. The second thing to notice is that as R_L grows larger than R_S the efficiency increases.

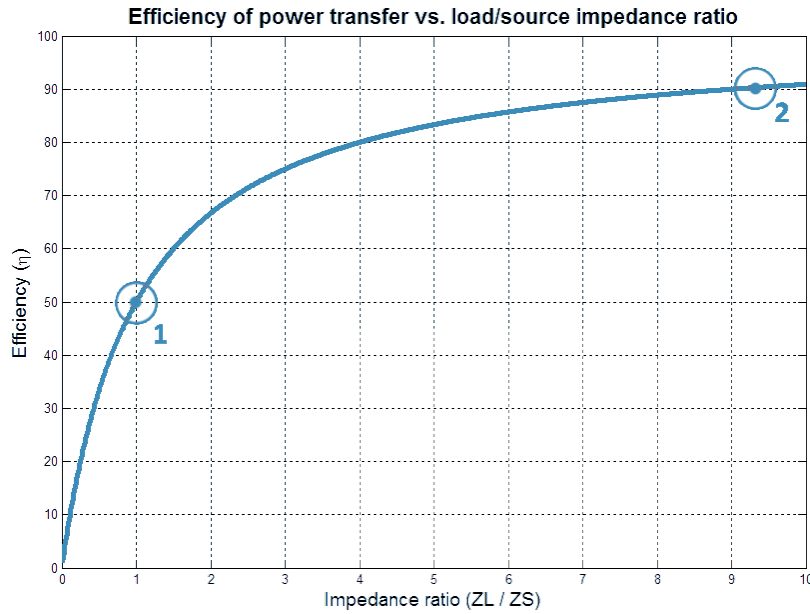


FIGURE 4.2: Efficiency of power transfer vs. Impedance ratio

For power harvesting systems the energy is often very volatile and small, and it is very important to be able to utilize as much of it as possible before it "vanishes". E.g. in piezoelectric vibration harvesting, a certain amount of energy is generated for every vibration pulse. This energy needs to be directed into the load or an external storage

before it escapes through system leakage. This means that the most important factor is to transfer as much energy as possible into the load and efficiency is not as important.

$$P_{tot} = \frac{V^2}{R_{tot}} \quad (4.2)$$

$$P_L = \frac{(V \frac{R_L}{R_L + R_S})^2}{R_L} \quad (4.3)$$

Inserting some theoretical values for R_S and V_S (figure 4.1) and utilizing equation (4.2)^[15] and (4.3) the ratio of R_L to R_S which yields the highest power output can be investigated.

$$V_S = 12V$$

$$R_S = 100\Omega$$

The resulting graph (figure 4.3) shows that the ratio of R_L to R_S which results in the most power transferred to the load is '1' ($R_L = R_S$). Referencing this to the plot of efficiency (figure 4.2) it can be seen that at this point the efficiency is 50%, meaning half of the generated power is 'lost'. For a energy harvesting application this is OK since we are extracting as much energy as possible regardless of this loss.

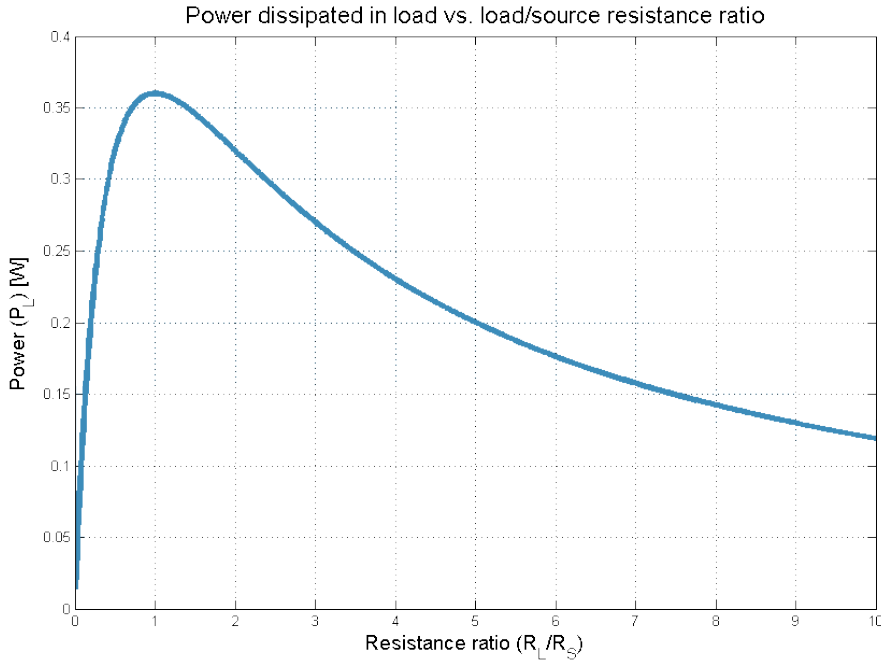


FIGURE 4.3: Power dissipated in load vs. resistance ratio

4.1.2 AC-power applications

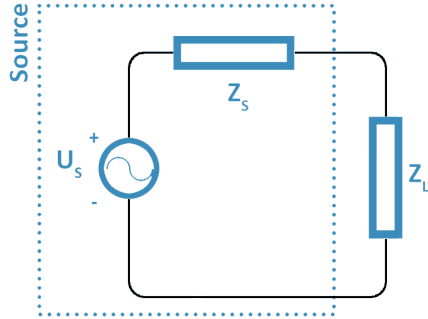


FIGURE 4.4: AC source and load impedance

The same behavior can also be found in AC-power applications, although some adaptations must be made. When dealing with AC-power the reactance (X) caused by capacitance (C) and inductance (L) must be taken into account. Combining the reactance as an imaginary value and the resistance as a real value gives the impedance (Z) (eq. (4.4)).

$$Z = R + iX \quad (4.4)$$

where:

$$X = X_L - X_C = \omega L - \frac{1}{\omega C} \quad (4.5)$$

For maximum power transfer to occur in an AC-power application the load impedance (Z_L) must be the complex conjugate of the source impedance (Z_S)^[16]:

$$Z_L = \overline{Z_S} \quad (4.6)$$

Which means that if $Z_S = R - iX$, then $Z_L = R + iX$.

This implies that if the source impedance is mainly capacitive (negative reactance), then the load impedance must be equally inductive (positive reactance). Building on eq.(4.5) and (4.6):

$$X_{load} = -X_{source} \quad (4.7)$$

$$(X_L - 0) = -(0 - X_C) \quad (4.8)$$

$$\omega L_{load} = \frac{1}{\omega C_{source}} \quad (4.9)$$

$$L_{load} = \frac{1}{\omega^2 C_{source}} \quad (4.10)$$

Plotting the result of eq. (4.10) for different values for C_{source} the inductance required for different values of source capacitance can be seen(figure 4.5). To illustrate the availability of different inductor sizes, the figure is marked with yellow and green areas. The yellow area shows what inductor sizes are commercially available^[17] regardless of package, while the green area shows what inductor sizes are commercially available in both surface mount type package and other packages^[17].

As the graph (figure 4.5) suggest, it would either require a huge source capacitance or a high frequency signal to be able to complex conjugate match the impedance of the capacitive source with commercially available inductors. Larger inductors could be made specially for the application, but prize and physical size makes this approach impractical.

Eq. (4.10) also implies that the inductance needed would be severely frequency dependent. This means that a complex conjugate impedance matched system would only

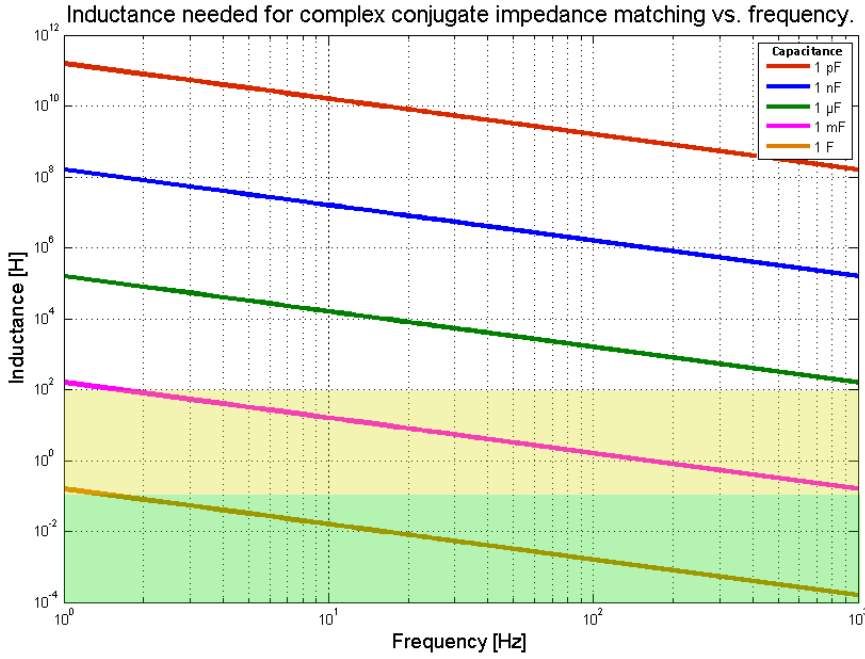


FIGURE 4.5: Inductance needed for complex conjugate impedance matching of capacitive source vs. frequency.

be matched for a very narrow frequency range. Further discussion regarding complex conjugate loading can be found in section 4.2.

4.2 Different loading techniques

In section 4.1 the concept of maximum power transfer and complex conjugate impedance matching was briefly discussed. This section will further elaborate on these concepts and introduce alternative loading methods.

4.2.1 Complex conjugate impedance matching

Earlier (sec. 4.1), how to draw the maximum amount of power was discussed and it was derived that complex conjugate matching of the load impedance was one way to achieve maximum power in an AC-power application.

When complex conjugate matching is done correctly, the output power is given by equation 4.11^[16]:

$$P_{L,max} = \frac{R_S^2 + X_S^2}{4R_S} I_S^2 \quad (4.11)$$

Or expressed in terms of voltage (eq. 4.13)^[16]:

$$P_{L,max} = \left| \frac{V_S}{Z_S + Z_{L,opt}} \right|^2 \Re(Z_{L,opt}) \quad (4.12)$$

$$P_{L,max} = \frac{V_S^2}{4R_S} \quad (4.13)$$

From eq. 4.13 we see that when complex conjugate matching is achieved, the maximum power delivered to the load ($P_{L,max}$) is only dependent on the voltage source (V_S) and the resistive part of the source impedance (R_S).

Although complex conjugate is easy in theory, it is not so easy to achieve in the real world. As was found in section 4.1, the load inductance required for a capacitive source impedance could be very high (fig. 4.5) for low frequency operations. This would introduce problems with availability, cost and size. Another drawback is that the required load impedance would vary greatly with frequency (f) (eq. 4.10).

4.2.2 Resistive impedance matching

Another way of loading the complex impedance source is using a purely resistive load. This does not always provide the optimal solution in terms of power output, but it is much easier to implement than complex conjugate matching.

The optimal value for the resistive load can be found by taking the absolute value of the source impedance (eq. 4.14)^[16].

$$R_{L,opt} = |Z_S| = \sqrt{R_S^2 + X_S^2} \quad (4.14)$$

This tells us that the optimal load resistivity will change with the frequency of the applied signal. This is the same behaviour as we saw with complex conjugate matching (eq. 4.10).

The potential maximum power of a resistive matched system is given by the equation below^[16].

$$P_{L,max} = \frac{R_S^2 + X_S^2}{2(\sqrt{R_S^2 + X_S^2} + R_S)} I_S^2 \quad (4.15)$$

Comparing this to the equation for maximum power we can see that the power output of the resistively matched system is lower than for the conjugate matched system by a factor of X_S . This means that the quality of the resistive impedance matching will increase as the reactive component of the source impedance decreases ($X_S \rightarrow 0$).

4.2.3 Adaptive impedance matching through DC-DC converters

Instead of using passive components to match the source impedance of the piezoelectric source, a more adaptive technique can be achieved using DC-DC converters. There are mainly two types of DC-DC converters; the linear and the switch-mode regulator.

The linear voltage regulator converts its input DC voltage to a lower output DC voltage. There are many types of linear regulators, but common to them all is that they lower the voltage by dissipating the excess power as heat. This is a simple, but not very efficient^[18] way of decreasing the output voltage.

The switch-mode converter uses a switch (transistor), an energy storage device (inductor or capacitor) and a diode to transform the input DC voltage to a higher or lower output DC voltage. As with the linear regulator, a lot of different switch-mode regulators exist, but they can generally be divided into four sub-categories. The buck, boost, inverter and flyback type converters^[19]. This section will give a brief introduction to the last two, namely the buck and boost converters and show that these devices may be suitable for impedance matching a piezoelectric power source.

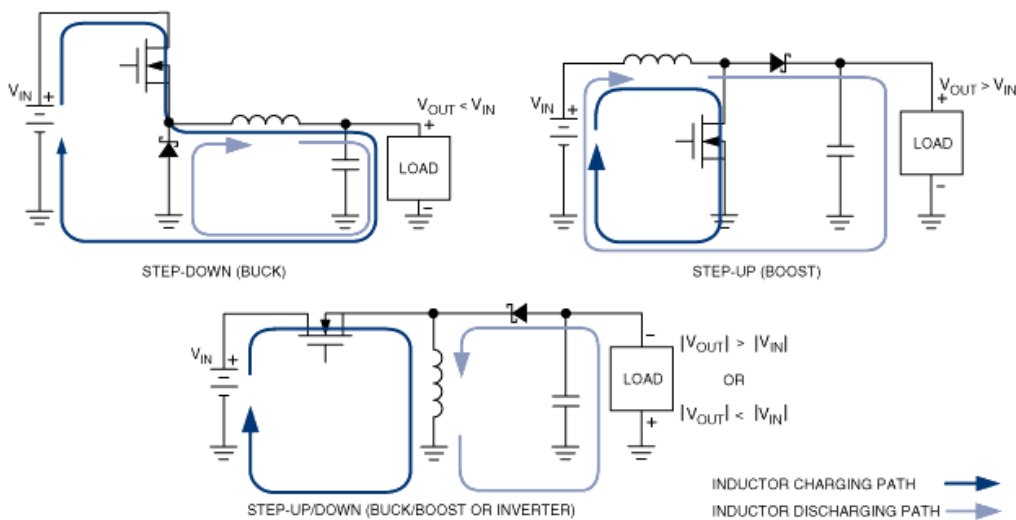


FIGURE 4.6: Fundamental switch-mode converter topologies.

Buck converters, or '*step-down*' converters (fig. 4.6, top left), produce a lower voltage on its output than on its input. The boost-converter, or '*step-up*' converter (fig. 4.6, top right) can have an output voltage higher than its input voltage. A combined topology, the buck-boost converter, also exists which can have an output voltage both higher and lower than the input voltage.

Common for all these topologies is that they rely on switching (PWM) the transistor on and off, changing the voltage drop on the inductor. The switch controller is not illustrated in figure 4.6, but it senses the output voltage of the converter and adjusts the duty cycle (D) of the PWM switch control to maintain the desired output voltage.

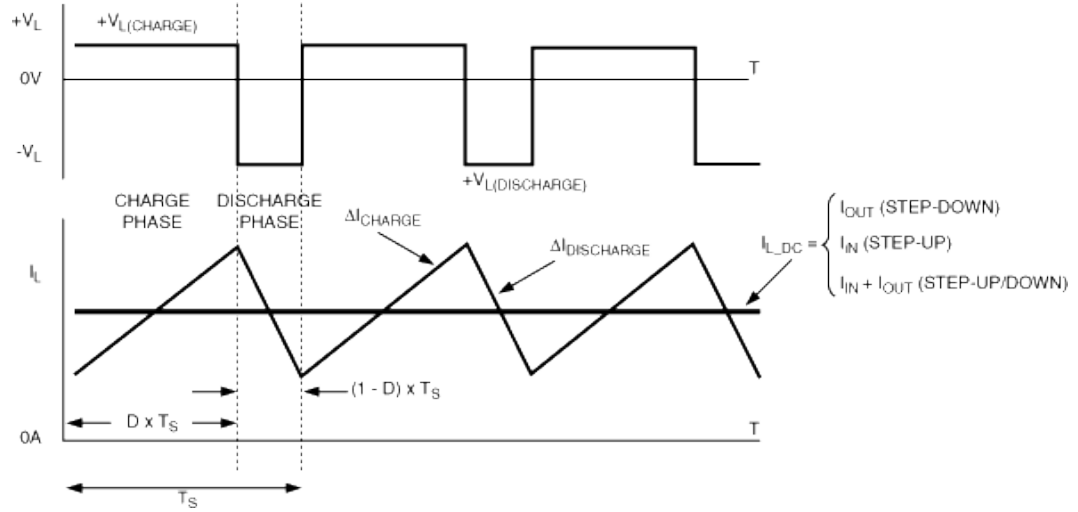


FIGURE 4.7: Voltage and current characteristics for inductor^[18].

For the buck-converter topology, the inductor current ramps up for the period the switch is closed. This is the charge phase (fig. 4.7) and the inductor current equals the output current to the load. Once the switch opens the inductor current ramps down, this is the discharge phase. Because of this, the DC-current through the inductor is dependent on the duty cycle of the PWM-signal controlling the switch. Since this switching usually happens at a fairly high frequency, a capacitor is added to the output to reduce the voltage ripple on the load.

The output voltage (V_{OUT}) of an *ideal* Step-down buck converter can be expressed by the following expression^[18] where D is the duty cycle of the switch and V_{IN} is the input voltage of the converter.

$$V_{OUT} = D \times V_{IN} \quad (4.16)$$

The boost-converter works in a similar way as the buck-converter. When the PWM-controlled switch closes, the whole input voltage is applied across the inductor, charging it and ramping up the current quite fast. When the switch opens, the energy of the charged inductor has no other option than to discharge through the diode and load. This creates a higher voltage on the converter output than on its input.

The output voltage (V_{OUT}) of an *ideal* Step-up boost converter can be expressed by the following expression^[18] where D is the duty cycle of the switch and V_{IN} is the input voltage of the converter.

$$V_{OUT} = V_{IN} \times \frac{1}{1 - D} \quad (4.17)$$

Combining these two topologies can yield a DC-DC converter capable of delivering an output voltage both lower and higher than the input voltage. This is called a *buck-boost* converter, or *step-up/down* converter, and can be seen in the lower part of figure 4.6. This configuration can be very useful in applications where the input voltage is varying over a large range, while the output voltage needs to be kept constant.

In an *ideal* buck-boost converter, the output voltage can be expressed as^[18]:

$$V_{OUT} = V_{IN} \times \frac{D}{1 - D} \quad (4.18)$$

In reality, all these topologies have inherent imperfections that limit efficiency and achievable output voltage ranges.

Continuous vs. discontinuous mode

When talking about DC-DC converters there are generally two modes of operation:

- Continuous Conduction Mode (CCM) - $I_L > 0$
- Discontinuous Conduction Mode (DCM) - $I_L \geq 0$

In *continuous mode* the current in the inductor I_L never falls to zero. The converter is always working to keep the output in regulation and there is always a voltage on the input.

In *discontinuous mode* the regulator may turn off for periods of time. This can happen if the input voltage is removed or reduced beneath the minimum input voltage of the

converter. It can also occur if the load has a high enough impedance that the output capacitance can drive the load for periods of time without dropping the voltage on the converter output enough to trigger the switching controller. In these periods the inductor current will be zero, and the converter is in DCM.

When working with energy harvesting there is often no guarantee that the energy source will remain active for the whole operational period of the system. If the output power of the source falls to zero and any DC-DC converters in the system shuts off, it is operating in discontinuous mode.

Input impedance

The input impedance of a DC-DC converter is affected by the duty cycle of the switching. If we look at the buck-converter in figure 4.6 its obvious that when the switch is constantly open, the input impedance is, given an ideal switch, infinite ($Z_{IN} \rightarrow \infty$). No load is connected to the input. On the other hand, if the switch would be constantly closed, the DC-behavior of the internal components would define the input impedance. For the discussed buck-converter the (ideal) inductor would have zero DC-resistance, and the (ideal) output capacitor would have infinite DC-resistance.

For *ideal* inductors and capacitors, their impedance can expressed as follows^[15]:

$$Z_{ind} = 2\pi f L \quad (4.19)$$

$$Z_{cap} = \frac{1}{2\pi f C} \quad (4.20)$$

For DC ($f = 0$):

$$Z_{ind} = 2\pi 0 L = 0 \quad \Omega \quad (4.21)$$

$$Z_{cap} = \frac{1}{j2\pi 0 C} = \infty \quad \Omega \quad (4.22)$$

This constitutes shorting out the inductor and disconnecting the capacitor. From fig. 4.6 (top left) it can be derived that in this case, the impedance can be defined only

by the load (and the diode). The impedance will of course vary greatly with different converter configurations, but this shows that different switch states causes different input impedances. If the switching frequency of the PWM signal is high enough, a dynamic range of impedance between the two extremes could be achieved.

Ottoman et al. proposes^[20] a buck-converter circuit to match the impedance of the piezoelectric generator.

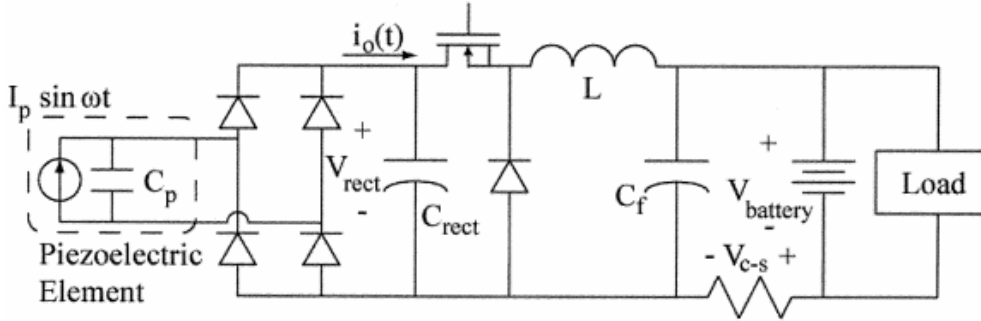


FIGURE 4.8: Buck converter circuit for piezoelectric energy harvesting proposed by Ottoman et al.^[20]

Their findings^[20] show that the optimal duty cycle for energy harvesting from a piezoelectric source, given the proposed circuit (fig. 4.8) can be expressed as a function of the rectified voltage from the generator (V_{rect}), the switching frequency of the PWM signal (f_s), the inductance (L), the piezoelectric capacitance of the source (C_p) and the mechanical excitation frequency (ω).

$$D_{opt} = \sqrt{\frac{4\omega LC_p f_s}{\pi}} \quad (4.23)$$

One major disadvantage of using such a buck-converter is that the input voltage must be higher than the output voltage^{[16][18]}. For periods of low excitation of the piezoelectric transducer there might be, depending on the transducer properties, periods of time where the transducer voltage output is lower than the desired converter output voltage. Utilizing a buck-converter could mean that during these periods, no power would be delivered to the load.

A better solution would be to utilize a buck-boost converter where the input voltage is allowed to vary below the converter output voltage while still maintaining output regulation^{[16][18]}. Such a circuit was proposed by Inman et al.^[16] and can be seen in figure 4.9.

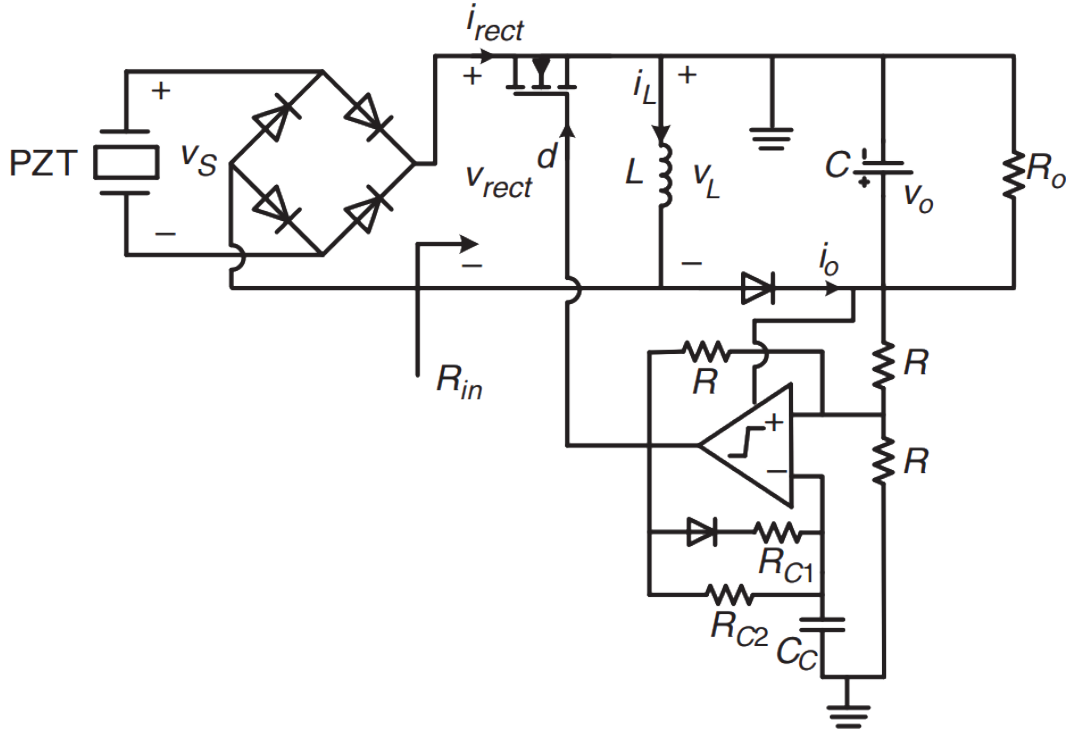


FIGURE 4.9: Buck-boost converter circuit for piezoelectric energy harvesting from a PZT source, proposed by Inman et al.^[16].

The input resistance (R_{IN}) of such a circuit operating in DCM mode can be expressed through the duty-cycle (D), inductance (L) and switching period (T_S) as follows^[16]:

$$R_{IN} \approx \frac{2L}{DT_S} \quad [\Omega] \quad (4.24)$$

Rearranging eq. 4.24 to express the duty-cycle yields:

$$D \approx \frac{2L}{R_{IN}T_S} \quad (4.25)$$

Looking back to 43 the expression for the optimal load resistance of a piezoelectric (or any other) source was given. It was also discussed that the resistive elements of the piezoelectric transducer usually could be neglected. Inserting eq. 4.14 into eq. 4.25 and removing the resistive source elements:

$$D_{opt} \approx \frac{2L}{R_{L,opt}T_S} \quad (4.26)$$

$$= \frac{2L}{X_S T_S} \quad (4.27)$$

$$= 2\omega C_p L f_s \quad (4.28)$$

Similar to the buck converter (fig. 4.8) the optimal duty cycle of the buck-boost converter is determined by the switching frequency (f_s), inductance (L), mechanical excitation frequency (ω) and the piezoelectric source capacitance (C_p).

The inductance and switching frequency are known system parameters, but the source capacitance and mechanical excitation frequency are not. The frequency could be easily captured by the duty cycle controller from the input signal (theoretically), but the source capacitance could be harder to determine in circuit. How this problem is tackled in modern IC devices is not known, but placing a capacitor on the input of the DC-DC converter of several magnitudes larger than the expected capacitance of the piezoelectric transducer could diminish the impact of different transducer topologies on the calculation of optimal duty cycle.

Chapter 5

Power storage

As discussed in the preface of this document the need for a long term power storage may be favorable in a piezoelectric vibrational energy harvesting application.

5.1 Different power storage technologies

In this section available power storage technologies from three main categories will be discussed and compared.

- Capacitors
- Batteries
- Electric double layer capacitors (Supercaps)

5.1.1 Capacitors

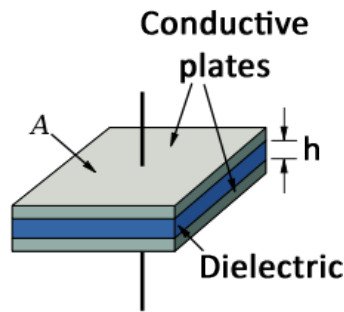


FIGURE 5.1: Illustration of plate capacitor [edited].^[21]

Capacitors are the most widely used energy storage technology in electronics today. They can be found in pretty much every electronic device today, used for *small scale* energy conservation and signal conditioning.

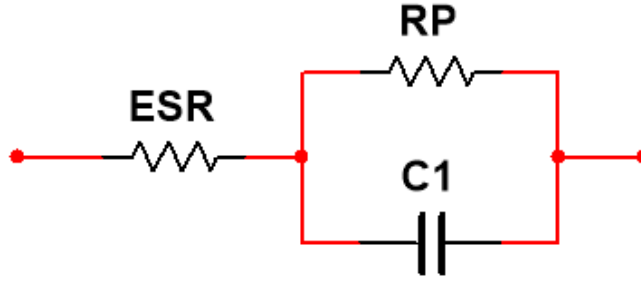


FIGURE 5.2: Equivalent circuit of capacitor.

The main advantage of using capacitors for energy storage is their low equivalent series resistance (ESR). This is a measure of how fast the capacitor can deliver its power. A drawback of the capacitor is that it can have a large leakage current, specially when the capacitance and voltage rating increases. This is caused by the inherent resistance (RP in fig. 5.2) in the dielectric material. The energy stored in a capacitor is also dependent on the capacitance and voltage (eq. 5.1) which means that as the energy increases, so does the leakage current.

$$E = \frac{1}{2}CV^2 \quad [J]^{[15]} \quad (5.1)$$

Charging a capacitor can be accomplished simply by putting a voltage differential across its two terminals. The charge time is determined by the capacitance and any series resistance^[15], internal, external or both.

$$t_{charge,63\%} = 1\tau = 1RC \quad (5.2)$$

$$t_{charge,99\%} = 5\tau = 5RC \quad (5.3)$$

This allows for fast charge (and discharge) with very low complexity and few to none extra components.

5.1.2 Batteries

Batteries have been around for over a century. They can be both disposable (*primary*) or rechargeable (*secondary*) and be constructed in various ways using different materials and structures, but they all rely on electrochemical cells capable of outputting their energy as electricity.

Batteries are still the most common way of storing large amounts of electric energy in electronic devices. They have small leakage currents, and is therefore capable of storing power over longer periods of time.

	Specific energy [Wh/kg]	Cycle life (80%)	Cell voltage [V]
Battery type	NiCD	45-80	1500
	NiMH	60-120	300-500
	Lead Acid	30-50	200-300
	Li-ion	110-160	500-1000
	Li-ion polymer	100-130	300-500
	Reuseable alkaline	80	50

TABLE 5.1: Comparison of battery technologies^[22]

Unlike capacitors, batteries can require special care to ensure the long time health of the battery. This can include controlling currents and voltages during charge as well as protecting from any transients that could damage the battery. These kind of considerations are especially true for nickel-metal hydride (NiMH) and lithium batteries (Li-ion and Li-ion polymer) which require dedicated charging circuitry, often found as dedicated ICs.

Nickel-metal hydride (NiMH) batteries have a quite high specific energy, but has a relatively short life time of 300-500 cycles^[22]. They also suffer from high discharge rates, and requires full discharge every cycle to avoid loss in performance.

Lithium batteries have a higher specific energy than NiMH batteries, which means lighter battery packs for the same amount of energy. Another advantage of the lithium batteries is cell voltage. This allows fewer series-connected cells than with NiMH batteries to achieve the same voltage range. Also, the self-discharge or *leakage* is much lower than for NiMH batteries

Although lithium cells cost more than nickel-metal hydride cells, they are the preferred choice when it comes to traditional batteries.

Solid State Batteries

A new type of battery has recently been introduced to the market. The *solid state battery*. This battery technology is based on the same lithium technology as Li-ion or Li-ion polymer batteries, but utilizes a solid electrolyte instead of the traditional liquid type. This means lighter, safer, smaller and more durable batteries^[23] with low leakage currents. Another benefit is that because they contain no liquid electrolyte, they are capable of withstanding the high temperatures found in solder reflow ovens. This

means they can be processed in high volume electronic manufacturing processes, allowing engineers to treat them as any other electronic component when designing circuits and PCBs.

5.1.3 Electric double layer capacitors (Supercaps)

Electric double layer capacitors, or *supercapacitors*, are somewhat newcomers in the energy storage industry. They can in certain cases offer the best from the both capacitors and batteries in a single device.

While regular capacitors store its charge between the conductive plates (fig. 8.1), the supercapacitors dielectric material and electrodes are more porous. This greatly increases the surface area of the electrodes, causing a significantly greater capacitance than traditional capacitor technologies. Looking back at eq. 3.28 on page 33 we see the relationship between electrode area (A) and capacitance (C).

A drawback of this configuration is that as the number of pores in the electrode-/electrolytic area increases, the risk of dielectric breakdown increases because of lower separation of charges. This means that supercapacitors are often limited to low voltage operation, and is easily susceptible to damage from transient voltage spikes.

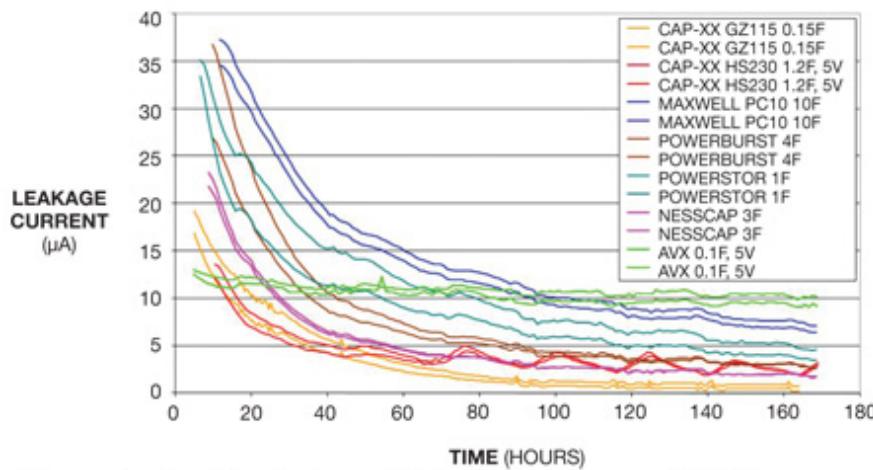


FIGURE 5.3: Leakage current for supercapacitors over time^[24]

The leakage current of supercapacitors can be quite low, but it can take some time to stabilize. This is related to the porous structure and the time it takes all the ions to diffuse^[24]. Figure 5.3 shows the leakage current over time for a handful supercapacitors. The trend is huge leakage currents for the first 20-40 hours, then the current stabilizes at decent levels. A rule of thumb for leakage of supercapacitors is 1×10^{-6} ampere per farad of capacitance^[24].

One important factor when dealing with supercapacitors, specially in energy harvesting applications, is that without an external circuit to limit the current into the capacitor the whole system could be crippled. The voltage of the input rail of the DC-DC converter would be controlled by the voltage of the supercapacitor, which may take quite some time to charge after being depleted due to its large capacitance. This could mean long periods of down-time for the energy harvester and by extension its connected WSN device.

Part III

Model and methodology

Chapter 6

Methodology

6.1 Piezoelectric transducer

6.1.1 Material selection consideration

For the support structure, copper clad FR4 material (PCB blanks) was selected. This was because it was readily available at HiST and both durable and stiff enough to prevent a "springy" behavior without deforming. It would also be easy to cut and shape without special tools.

When selecting the piezoelectric material, the findings in section 3.3.1 must be taken into account. Another and more practical consideration is how easy the material is to work with. This parameter may surpass all others when selecting the piezoelectric material, since the tools available at HiST are limited in terms of working with special materials. Availability will also play a huge part in selecting the piezoelectric material.

6.1.2 Simulation

To design the piezoelectric transducers, a model is required to predict the behavior of the device based on geometry and material selection. This modeling is done in COMSOL Multiphysics which is a widely used FEA tool. Although the author has no previous experience with these kinds of tools, both HiST and Kongsberg Maritime expressed interest in the utilization of this tool for the task.

The learning curve with this kind of software was expected to be high, and this could also be the biggest source of problems using it. COMSOL also requires the user to have a

thorough understanding to the physics behind the model, which could lead to problems if complex physical issues present themselves.

The development of the model in COMSOL is thoroughly discussed in chapter 7.

6.1.3 Production

The transducer shape could be designed in a CAD tool and then the FR4 material could be cut into shape using the CNC-mill (ProtoMat S103^[25]) available at HiST. Due to many periods of down-time for the mill during the last year, manually cutting the FR4 material was a backup plan if it should fail.

6.1.4 Commercial transducer

In addition to the produced transducers, a commercial transducer will also be used in the energy harvester and its results will be compared to the 'home made' transducer.

6.2 Power manager

Designing the power manager for the piezoelectric energy harvester mainly involves component selection, drawing of schematics and PCB design.

6.2.1 Schematic and PCB design

Design tools

For designing the schematics and PCB-layout of the power manager device, Altium Designer^[26] was utilized. It offers great flexibility and enables the user to easily design large multi-sheet projects and generate professional output documentation with the click of a button. Altium also offers a huge built-in library of electric components and PCB-footprints which can save the designer a lot of time.

Schematics

A good schematic lays the ground for a good end product. To keep things tidy, different parts of the power manager circuit would be split up over several sheets with signal labels connecting them together. A top-sheet showing the connectivity of the sub-sheets

would also be generated to show the project topology. Adding specific component part numbers and names allows Altium to generate useful part lists and bill of materials. Altium also allows adding notes and images, this can be very helpful when trying to document any special circuits or connections in the sheet.

Printed Circuit Board

Once the schematic is completed and all connections and component footprints are in order, Altium can import them into a PCB project. Now the actual placement of the components on the PCB can be determined and the connecting tracks can be laid down. Although the user has full control of component and track placement, Altium offers great interactive help functions that show you the optimal track position and automatically shifts colliding object out of the way. An auto-placer and auto-router is also built into the software. These features can basically design the whole PCB without the user having to contribute. This is often only partially desirable in projects where there are large repeating patterns of components, and not in small project like the power manager built in this thesis.

One feature that can be immensely helpful in projects like this, is the ability to add 3D-models of all components on the circuit board. Altium allows adding these models and viewing a 3D-representation of the board as a whole. This enables the user to detect component collisions and problems related to placement. Altium also allows exporting the whole PCB, including components, as a 3D-model. This can later be imported in a CAD-tool where brackets and casings can be designed *around* the actual PCB. This can ensure perfect fit without the need for several design iterations.

The PCB design for this project should at least include one copper layer (top or bottom), and a layer containing the board outline. This is the minimum amount of layers required for producing a PCB with the CNC-mill at HiST (ProtoMat S103^[25]). Since the PCB designed in this project was planned ordered from a professional PCB manufacturer, up to 4 copper layers can be utilized. Solder masks should also be added to help with soldering the SMD components without creating short-circuits. To improve both cosmetics and troubleshooting, silkscreen layers can be added to the top and bottom of the PCB to help identify components and connector pinout.

6.3 Casing

The casing for the piezoelectric energy harvester is very important. It serves four main purposes:

- Ensuring that there is a good mechanical coupling between the vibrating environment and the transducer base.
- Allowing some tuning of the transducer during installation.
- Securing a free space for the transducer end to move about.
- Keeping contaminant objects or fluids out of the system.

6.3.1 Software

Solid Edge ST6 is a CAD tool developed by Siemens. It is a commercial product, but a free academic version is offered to students and educators^[27] and will be used to design the casing.

The tool enables the user to design 3D-objects either from 2D-drawings or in a native 3D user interface. It is also possible to create pure sheet-metal objects by bending a flat reference sheet. Multiple objects and parts can be put together to form large assemblies, and the software makes generating assembly drawings and exploded views easy. Moving parts can be visualized and any collision between objects can be detected.

6.3.2 CAD modeling

When drawing the CAD-model of the casing for the energy harvester some main design elements must be included:

- Screw holes or similar to accommodate securing the power manager PCB to the casing.
- An adjustable clamping fixture for the piezoelectric transducer.
- Screw holes or similar for securing the energy harvester to the surroundings.
- Sealed but openable design. "Box with lid" type configuration could be advantageous.
- Accommodation for electrical connections to external device(s).

It is also good practice to try to incorporate scalability into the design. When dealing with different transducers lengths, it would be practical being able to scale the length (and other parameters) of the casing accordingly without the need for a complete redesign.

Keeping the casing as small as possible contributes to increasing the energy density of the system when compared to other energy sources. This is desirable, and size should be kept to a minimum.

6.3.3 3D-printing

Once a good 3D-model of the casing has been designed, the file can be prepared for 3D-printing with the MakerBot Replicator 2 available at HiST. This device allows fused deposition modeling (FDM) of polylactic acid (PLA) to form a functional prototype of the device, with the click of a button. The PLA is deposited layer for layer until the 3D-model is realized and the production time is usually measured in minutes or hours depending on the part size.

This approach allows fast and cheap prototyping of mechanical parts and is an excellent tool for producing the casing for the energy harvester.

6.4 Data acquisition and analysis

To measure the performance of the system, system parameters should be monitored and analyzed. This could be achieved by the LabVIEW system from National Instruments^[28] and their data acquisition devices. HiST has a good selection of these tools, and an appropriate combination will be selected to perform the task of data acquisition. Data analysis will be implemented on a computer through the LabVIEW platform.

Chapter 7

Modeling

Developing a transducer model in COMSOL multiphysics

COMSOL Multiphysics is a general purpose FEA software platform for modeling and simulating physical and mathematical problems. This software enables modeling of the piezoelectric transducers, and can in theory give an accurate estimations on nearly every imaginable parameter including eigenfrequencies, frequency response and output power of a system.

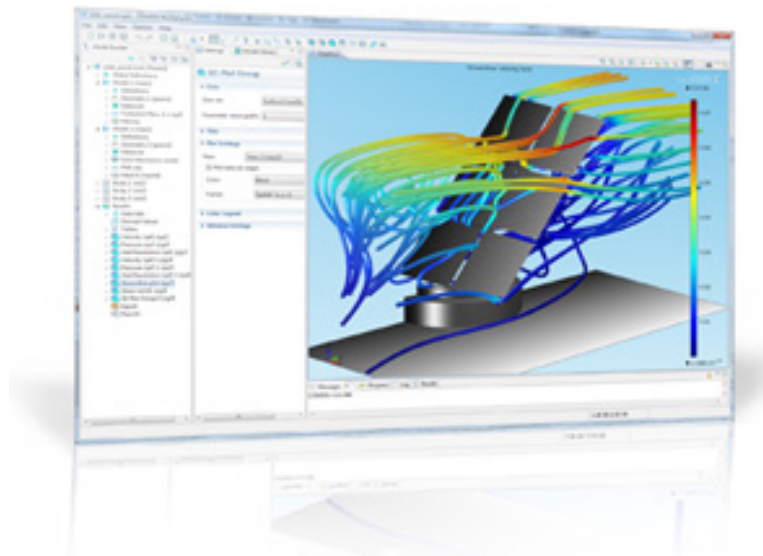


FIGURE 7.1: COMSOL Multiphysics^[29]

When modeling piezoelectric transducers, both Mechanical and Electrical domains must be include. Both static and time-dependent forces can be added in every direction and see how the material responds in either a static, time-dependent or frequency domain

analysis. Simulation of the developed electric field generated in the piezoelectric materials in the model, based on the values for strain or stress derived from the material properties module can also be achieved.

Defining the model

The process of developing a model of the piezoelectric transducer can be split into the following main steps:

- Define the model geometry
- Define the material properties of the different domains
- Define relationships and external forces
- Meshing and computing results

7.1 Model geometry

As discussed earlier, this thesis focuses on the cantilever bimorph piezoelectric transducer. The layers of the model are as defined in the bimorph transducer described in figure 3.9 on page 25, but the adhesive and electrode layers are ignored due to their low thickness and therefore *assumed* low impact on the transducers behavior. The transducer is modeled as three rectangular domains, where the center domain is the support structure with the piezoelectric domains on both sides (top and bottom). The transducer base ('fixed end') is located to the left, while the free end is located to the right (referenced to the x-axis in figure 7.2). Additionally, a round area is defined on top of the transducer as a reference area for adding a mass to tune the behavior of the transducer.

The size and position of these domains and areas are defined as global parameters (see table 7.1) so that they can be easily modified by the user or the solver during parametric sweeps. The parameter names also reflect the materials used to build the transducer.

TABLE 7.1: Geometric parameters

Parameter name	Description
L_FR4	Transducer length [m]
w_FR4	Transducer width [m]
h_FR4	Support material thickness [m]
L_PVDF	Length of piezoelectric layers [m]
w_PVDF	Width of piezoelectric layers [m]
h_PVDF	Thickness of piezoelectric layers [m]
mend	Added mass on transducer 'tip' [kg]
offset	Added mass offset from tip [m]

7.2 Adding material properties

Once the geometry of the model is defined, the different entities, or 'domains', needs to have their material properties defined.

Support structure domain

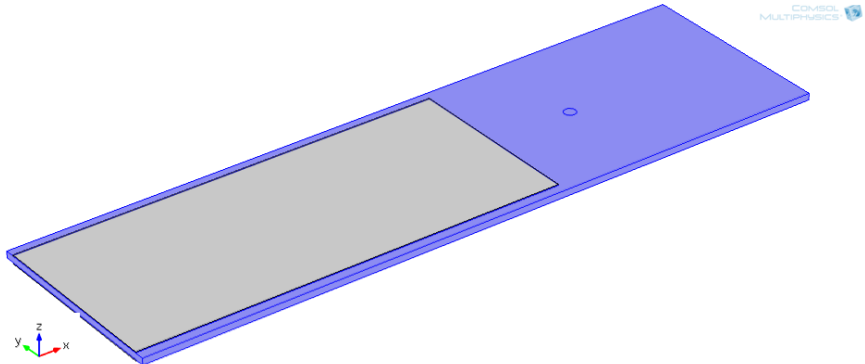


FIGURE 7.2: FR4 material domain (FR4 marked as blue).

For this model, the material for support structure (FR4) can be found as a built-in material in COMSOL.

TABLE 7.2: FR4 properties in COMSOL

Property	Value
Density	1900 [kg/m ³]
Young's Modulus (Y)	22e ⁹ [Pa]
Poisson's ratio	0.28
Relative permeability	1
Electrical conductivity)	0.004 [S/m]
Relative permittivity (ϵ_r)	4.5
Coefficient of thermal expansion)	18e ⁻⁶ [1/K]
Heat capacity at constant temperature	1369 [J/(kg * K)]
Thermal Conductivity	0.3 [W/(m * K)]

Piezoelectric domains

The piezoelectric domains exist on the top and bottom surface of the structure. Figure 7.3 shows the top piezoelectric domain in COMSOL.

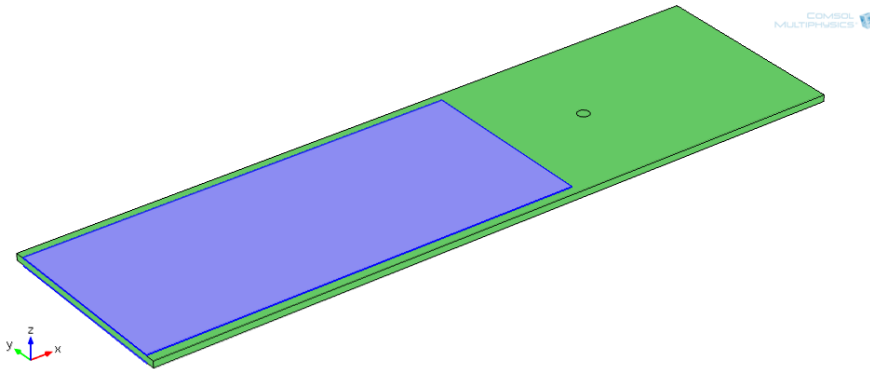


FIGURE 7.3: Piezo material domain (marked as blue). Identical domain exist on bottom side.

7.3 Defining relationships and external forces

Base excitation

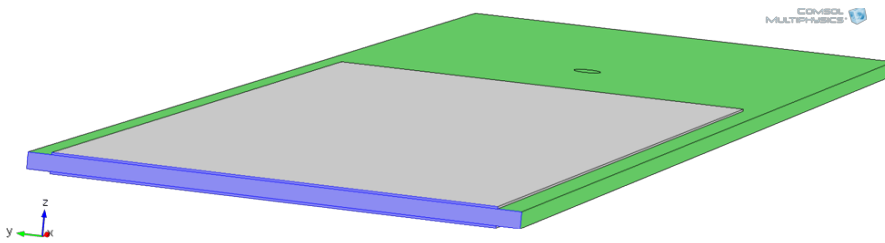


FIGURE 7.4: Prescribed displacement boundary in COMSOL (boundary placement marked as blue)

To enable the model to represent a cantilever beam, the behavior of such a system must be imposed on the model. This is done by adding a *Described displacement* boundary to the 'fixed' (see figure 7.4) end of the transducer.

The prescribed displacement boundary allows the model to emulate the fixed base of the transducer and impose a static or time-variant displacement in any axis. For analyzing the static deflection of the beam, the deflection in all axis is described as zero ('0'). This means that the base of the transducer is locked from moving in any axis.

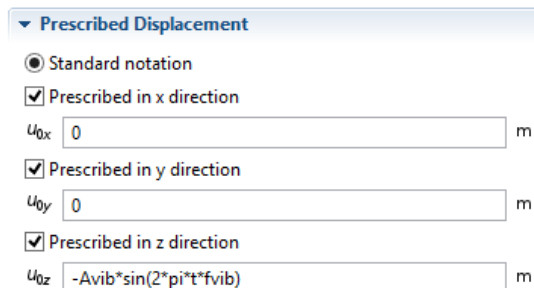


FIGURE 7.5: Prescribed displacement interface with time-dependent value in Z-axis.

For doing a time-dependent analysis COMSOL needs a time-dependent input expression for displacement. Figure 7.5 shows a scenario where the displacement in X- and Y-axis are locked while the Z-axis displacement is described as:

$$U_{0z} = -Avib \cdot \sin(2 \cdot \pi \cdot t \cdot fvib) \quad (7.1)$$

Equation 7.1 shows global parameters defined by the user in COMSOL to describe the amplitude (Avib) and frequency (fvib) of the displacement. These parameters together with the time factor (t) given by the solver when running a time dependent analysis, yields a function for displacement in Z-axis over time.

When performing frequency analysis of the system, a static value, e.g. $U_{0z} = 1e - 3$ [m] is inserted and COMSOL automatically uses this as the amplitude of the displacement while varying the frequency within the specified range.

Gravity effect

To emulate the effects of gravity on the transducer a 'Body Load' boundary is added to all domains of the geometry. The force can be described in COMSOL as:

$$F_{Vz} = -g_const \cdot solid.rho \quad [N/m^3] \quad (7.2)$$

COMSOL then gathers the density (*solid.rho*) from the material properties and calculates the distribution of 'weight' in the model by multiplying with the built-in gravitational constant (*g_const*). The force is applied in the negative Z direction or 'downwards'.

Added mass

A small mass can be attached to the tip of the transducer to change its behavior. This is achieved in the model by adding an 'Added mass' boundary to the defined circular area described in section 7.1.

Electric terminals and load

Electric terminals are added to each side of the piezoelectric layers, and connected so that the layers form a series connection. A resistive load is than added between the output terminals, enabling the model to calculate the dissipated power.

7.4 Meshing

Meshing divides the model into many small tetrahedral areas. This defines the resolution of the simulation and can play a huge role in both the accuracy and calculation time of the model. Since the piezoelectric layers in the transducer will be quite thin, the generated mesh can not be to coarse to represent the height of these layers. The standard setting ("normal") for mesh size divides the model into approx. 15325 tetrahedral elements, but also generates a warning that the selected mesh size is to coarse for thin elements. Selecting the "fine" setting eliminates this warning, but generates 53155 number of elements. This is a significant increase in resolution and required computation time.

As discussed later in section 7.5, this was problematic and a different approach was needed. COMSOL allows the user to customize the meshing parameters. Quite some time was spent trying to lower the amount of generated elements while still avoiding errors regarding thin elements. The resulting mesh parameters can be seen in table 7.3.

TABLE 7.3: COMSOL meshing paramters (note variable h_{PVDF} from table 7.1)

Parameter	Value
Maximum element size	0.02
Minimum element size	$(h_{PVDF}) * 8$
Maximum element growth rate	2
Resolution of curvature	0.5
Resolution of narrow regions	0.02

With these mesh settings the generated elements was reduced to approx. 5000 and the compute time was brought down to a realistic level using commercially available computer systems. COMSOL still reports the error message "*Warning: Low minimum element quality*" which is related to the resolution of the model and may affect the accuracy of the model output.

7.5 Verification of model and testing

Computing time

When first trying to solve the model, the calculation times were immense. Trying to simulate the mechanical frequency response of the transducer could take up to 20 min per step, and because of the narrow bandwidth of the transducer (figure 3.11 on page 31) a fine step-size was required. This meant that solving the frequency response from 50 - 100 Hz with a step-size of 1 Hz could take up to 16 hours. If the solved results for a specific step is not within the range of accepted error, COMSOL will automatically add extra computation steps around the original problematic step, further increasing simulation time.

Not knowing what simulation times to expect due to little experience with FEA-analysis, meant that a lot of time was spent trying to run timely simulations. A change in computing environment to the Amazon Elastic Computing Cloud (EC2) was successfully achieved, and the rented virtual machine was set up to run COMSOL.

TABLE 7.4: Rented EC2 computing node (m2.4xlarge) specifications

Parameter	Value
Type:	"m2.4xlarge"
Price:	\$ 1.1 per hour (On demand)
Computing Units (ECU):	26
Virtual CPUs (vCPU):	8
Memory:	68.4 Gb
Storage:	2x 840 Gb SSD

Once this system was up and running, a large test was set up with four frequency sweeps from 0 to 100 Hz with a 1 Hz step size. After 19 hours, the simulation came to a stop. This took more time than expected and since no funding was available for this part of the project, the cost at approx. \$21 per simulation was too much. This led to the refining of the model mesh discussed in section 7.4, sacrificing model accuracy for reduced computing time.

Damping

Another problem that arose in the testing of the model was the lack of damping parameters. Running simulations would result in a transducer tip-displacement of several magnitudes higher than the transducer length. This is the same behavior we witnessed in figure 3.11 on page 31 (infinite magnitude factor) where we came to the conclusion that some damping is always present in the system ($\zeta > 0$).

COMSOL allows adding a damping boundary to the model. This can be done in two different ways^[30]: *loss factor* and *Rayleigh* damping. Loss factor damping, also called structural or material damping, is based on how much energy is dissipated in the materials. Utilizing this kind of damping requires knowledge of the isotropic or anisotropic loss factors of the materials. These could not be found for the materials used in the model.

Rayleigh damping is another approach which involves measuring the response of the actual transducer at two frequencies and inserting them into the model. This would require a back-and-forth approach between building transducers and refining the model which could not be achieved within the time frame of this project.

This was a major drawback, and deemed the model useless for a lot of the desired simulated parameters. Both time-domain and frequency analysis could not be achieved without damping, and left only static analysis of e.g. the natural frequency (*eigenfrequency*) of the transducer. Although this is a sub-optimal solution, being able to calculate the natural frequencies and mode shapes of the transducer structure would help a lot in the transducer design.

Verifying against known transducer

To verify the behavior of the model, the physical parameters of a known piezoelectric cantilever beam transducer is used as parameter input in the model. The transducer used is the V21BL Voltule transducer from Midé^[31].

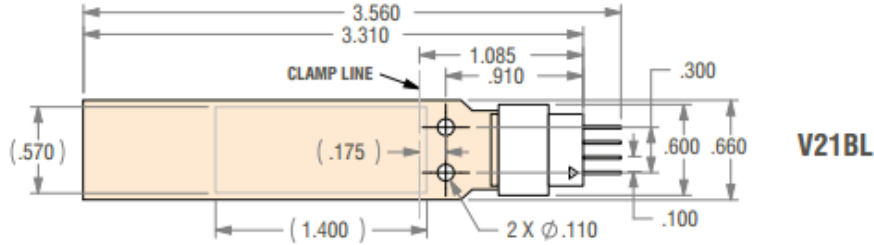


FIGURE 7.6: Dimensions of V21BL transducer (imperial units)^[31]

Entering the transducer parameters into the model and performing eigenfrequency analysis for the first 6 eigenfrequencies gives us the results seen in figure 7.7.

The natural frequency (f_n) of the modeled transducer is 104 Hz, this is close to the specified value of 110 Hz^[31]. The datasheet^[31] also specified natural frequencies for the transducer with an added tip mass of 1, 2.4 and 4.8 grams. The exact placement of this added mass is not specified. Some experimentation with the model showed that adding

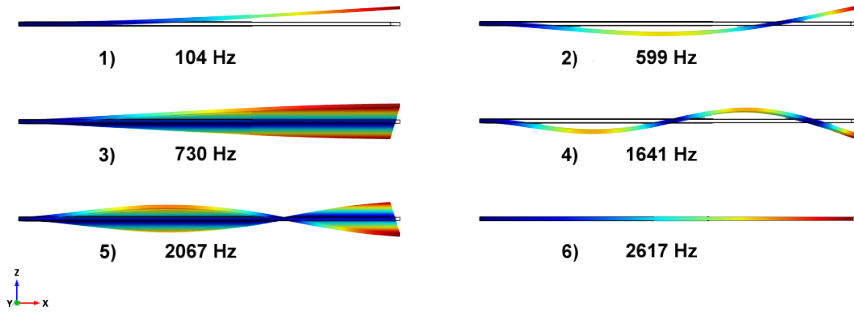


FIGURE 7.7: Eigenfrequencies of modeled Voltule V21BL transducer with no added end mass

the mass 15 mm from the transducer tip showed very similar results as stated in the datasheet^[31].

TABLE 7.5: Natural frequency (f_n) of modeled V21BL transducer with various end masses placed 15 mm from transducer tip vs. V21BL datasheet specification

End mass	f_n from simulation	f_n from datasheet ^[31]	Deviation
0 kg	104.46 Hz	110 Hz	-5.54 Hz / -5.30 %
$1e^{-3}$ kg	65.33 Hz	65 Hz	0.33 Hz / 5.08 %
$2.4e^{-3}$ kg	47.90 Hz	50 Hz	-2.1 Hz / -4.38 %
$4.8e^{-3}$ kg	35.85 Hz	40 Hz	-4.15 Hz / -11.58 %

This proves that the model can give a good estimation of the natural frequency of a cantilever beam transducer based on its geometry and materials, and it can be used for designing transducers for a specific frequency target.

Part IV

Implementation

Chapter 8

Transducers

This chapter discusses how the piezoelectric transducers were implemented with regards to material choice and production, but also choosing a commercial transducer for reference and testing.

8.1 Material selection

A lot of effort was put into finding a supplier for piezoelectric raw materials that would deliver small batches for this project, and as discussed in section 6.1.1 availability soon became the key factor in material choice. A company called *Precision Acoustics* was found to deliver a student kit^[32] containing three PVDF sheets (5×5 cm) of different thickness (28, 52 and 110 μm). Although section 3.3.1 suggested PVDF might be inferior to the PZT type materials, it would be a lot easier to work with polymers than ceramics.

The material properties of the selected PVDF material can be seen in table 8.1.

Seeing that the strain coefficient (d_{31}) is even lower than the figures presented in section 6.1.1 further implies that more suitable materials exist, but given the circumstances it would have to suffice.

8.2 Production

Producing the transducer was done using, as discussed in section 6.1.1, raw PCB material (FR4) as support structure. A base frequency in the 20-30 Hz area, which could be tuned upwards by the clamping system discussed in sections 6.3, was desirable. This would

Parameters	Density	1780 kg/m ³
	Longitudinal Acoustic Velocity	2260 m/s
	Melting temperature	175 - 180 °C
	Curie temperature	None
	Max. operating temperature	70 °C
	Metallisation	250 nm Gold + 40 nm Chrome
	Film orientation	Uni-axially oriented film
	Poling method	Continuous roll via Corona discharge
	Poling uniformity	Small scale local variations
	Piezo coefficients (approx.)	$d_{31} = -5 \times 10^{-12}$ to -6×10^{-12} m/V $d_{32} = -4 \times 10^{-12}$ to -5×10^{-12} m/V $d_{33} = -28 \times 10^{-12}$ to -32×10^{-12} m/V
	Dielectric constant	10 - 12

TABLE 8.1: Properties of chosen PVDF film^[32]

make the transducers tunable to the vibrations in the 50 Hz area illustrated in figure 2.2 on page 14.

Entering a transducer length of 150 mm, width of 25 mm and thickness of 0.9 mm into the COMSOL model (section 7), which were suitable dimension given the raw materials, gave a natural frequency of approx. 28 Hz. This was perfect, and the FR4 material was cut into shape. Since the PCB^[25] mill was down for maintenance, the cutting had to be done by hand using power tools and sand paper. This was tedious work, but the results were OK.

Once the support structures in FR4 was cut to shape, the PVDF was cut and glued to both sides of the copper-clad FR4 using silver conductive epoxy (8331S-15G^[33]). Strands of 0.127 mm copper wire were glued to the outwards facing sides of the PVDF material, using the same conductive epoxy, and brought towards the inner end of the transducers where they were soldered to connectors. Changing between series and parallel connection of the PVDF on each side of the transducer can be easily changed by resoldering the wire connections. Lastly, all conductive parts of the transducer were covered with Kapton®. tape to reduce the possibility of short circuits.

FIGURE 8.1: 8331S-15G silver conductive epoxy.^[33]

One major problem during the production of the transducer was to not get any conductive epoxy on the sides (thickness direction) of the PVDF material when gluing it to the

support material. One small misplaced epoxy drop could connect the top and bottom piezoelectric electrodes and cause a short-circuit. As the epoxy is rated at 0.006Ω ^[33] per meter, even a microscopic amount could cause a low resistive connection between the top and bottom electrodes.

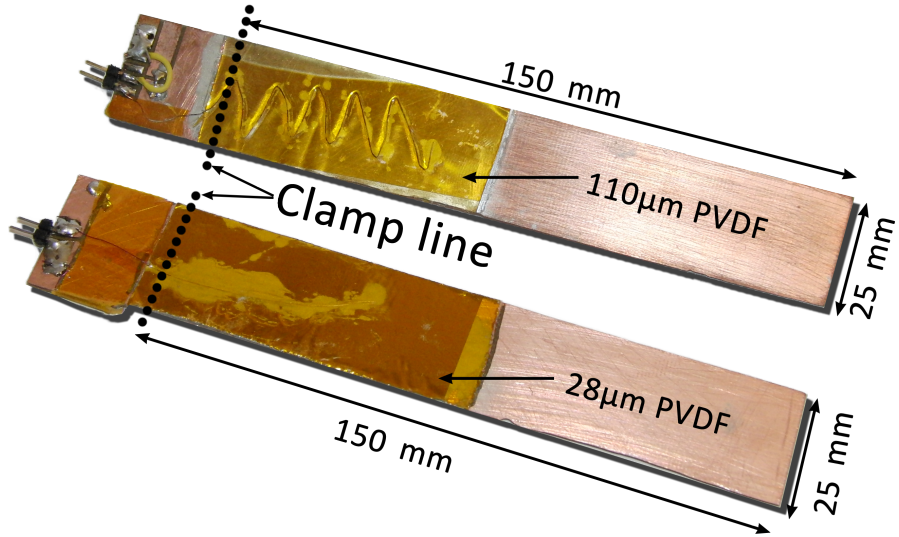


FIGURE 8.2: The two produced transducers with 28 and 110 μm PVDF layers. PVDF layers exists on both top and bottom sides of both transducers.

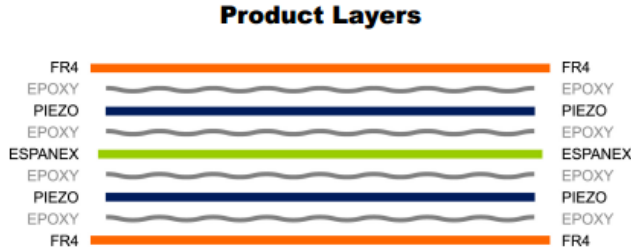
Three transducers were produced. The transducer with the 52 μm PVDF layer was damaged during production and scrapped. The 28 μm PVDF transducer was shorted out (300Ω across piezo film) by the conductive epoxy and could not be repaired. The transducer with the 110 μm PVDF layer was successful. The 28 and 110 μm PVDF transducers can be seen in figure 8.2.

8.3 Commercial transducer



FIGURE 8.3: Voltule V21BL transducer from Midé^[31]

In addition to the transducers produced in this project, a commercial product was also used for testing and comparison. The chosen commercial transducer is the V21BL transducer from *Midé*, briefly discussed in section 7.5. Since this is a commercial product there is a sparsity of information available of its composing materials, but *Midé* offers^[34] some insight into its composite structure (fig. 8.4).

FIGURE 8.4: Composite structure of V21BL^[34]

The V21BL transducers is composed of FR4, epoxy and espanex® in addition to the piezoelectric material. *Midé* does not state what piezoelectric material is used, but some of its properties are available^[34].

Parameter	Symbol	Value	Unit
Piezo Properties	ϵ_{r33}^T	1700	
	ϵ_{r33}^S	830	
	k_{33}	0.72	
	d_{33}	390×10^{-12}	C/N
	g_{33}	24×10^{-3}	Vm/N
	σ	7800	kg/m ³
	Y_{33}^E	5.3×10^{10}	N/m ⁻³
	Y_{33}^D	6.9×10^{10}	N/m ⁻³
	T_C	350	°C

TABLE 8.2: Properties of piezoelectric material in V21BL transducer^[34]

Looking at the properties for the piezoelectric material in the V21BL transducer (table 8.2) and comparing to the data in table 3.1 on page 23 the data resembles the reference data for 'SOFT PZT'.

Voltage output

The natural frequencies and open circuit output voltage of the V21BL transducer with different added tip mass is listed in table 8.3^[31].

Looking at the data we see that the output voltage varies over a great range from approx. 4 to approx. 45 Volt. Without any tip-mass the voltage still varies a lot from approx. 4 to approx. 12 volts. This must be taken into consideration when selecting an appropriate DC-DC converter.

Tip Mass [gram]	Natural Frequency [Hz]	Excitation Amplitude [g]	Open Circuit Voltage* [V]
0	110	0.25	3.95
0	110	0.375	5.35
0	110	0.5	6.6
0	110	1	12.1
1	65	0.25	8
1	65	0.375	9.9
1	65	0.5	12.4
1	65	1	22.1
2.4	50	0.25	9.8
2.4	50	0.375	13.7
2.4	50	0.5	19.1
2.4	50	1	27.5
4.8	40	0.25	13.2
4.8	40	0.375	19.2
4.8	40	0.5	25.9
4.8	40	1	44.4

* Piezo wafers connected in series

TABLE 8.3: Natural frequency and open-circuit output voltage of V21BL^[34]

Chapter 9

Power manager

This chapter discusses the implementation of the power manager device with focus on component selection, schematic drawings and PCB design.

9.1 Component selection

9.1.1 DC-DC Converter

The amount of available DC-DC converters is endless, but dealing with an energy harvesting application sets some strict demands for the IC device.

- High efficiency (low quiescent current)
- Protection from high voltage spikes from piezoelectric transducer
- Small package
- Large operational range and high maximum input voltage

Given these parameters, the amount of suitable DC-DC converters dropped drastically. Many devices are specifically made for energy harvesting applications and especially solar cells are heavily targeted by IC manufacturers. Since solar cells, TEGs and many other sources of harvestable energy generally has a low voltage output ($< 5V$), the selection of specialized energy harvesting DC-DC converters with a high maximum input voltage are sparse.

One of the devices that stood out was the LTC-3588^[35] from *Linear Technology*. It has an input voltage range of 2.7 to 20 volt, is a good fit good with the output voltage of the reference transducer (table 8.3). It also has a low quiescent current of 450

nA in UVLO-mode and 950 nA when maintaining a regulated output voltage without load. Additionally it was mentioned in the transducer (V21BL) datasheet^[31] as a recommended device for interfacing the *volute*^[31] series of transducers.

One drawback with this device is that is a buck-converter, only capable of delivering an output voltage lower than the input voltage. This was discussed in section 4.2.3, and the conclusion was that the best case would be to utilize a buck-boost converter. In lack of better options, the LTC3588 was chosen for the job.

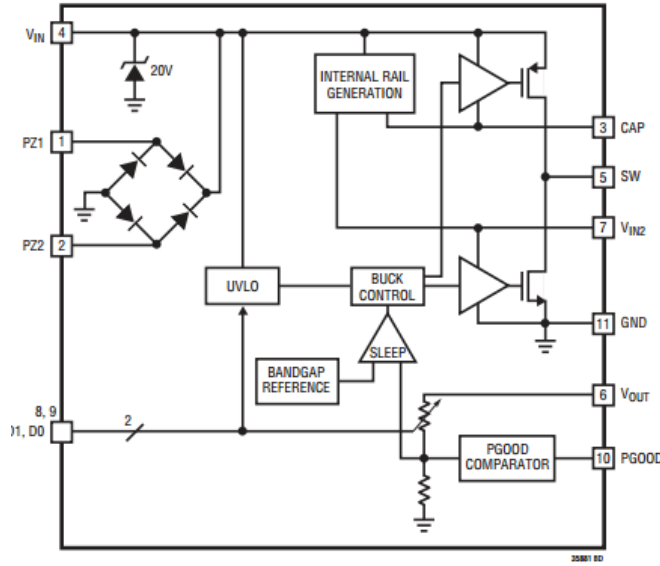


FIGURE 9.1: Block diagram of LTC3588 DC-DC step-down (buck) converter^[35]

Figure 9.3 shows a block diagram of the internal components of the LTC-3588. One big advantage of this devices is that it has an internal bridge rectifier which enables the converter to be connected directly to an A.C. power source (PZ1 and PZ2 inputs). Not having to implement an external rectifier circuit saves valuable PCB real estate and could lower component and/or production cost. The voltage input of the converter is clamped to 20 V which can provide over voltage protection from transients in the piezoelectric generator. The output voltage is pin selectable (D0 and D1) to 1.8, 2.5, 3.3 or 3.6 V.

One very important feature about the LTC3588 is that although the input voltage range goes as low as 2.7 V^[35] (for 1.8 V output voltage), there is a hysteresis on the input of the converter. This means that after the device has been shut-off, it needs a higher voltage than the minimum voltage to start up again. Once the converter has started, the voltage may fall as low as the minimum input voltage while the converter keeps the output in regulation.

In this project, 3.3 V was chosen as the output voltage based on commonness and simplicity. This means that the start-up threshold is at 5.05 V (typically), while the shutdown (or UVLO) threshold is at 3.67 (typically). After a period of no power (voltage lower than 3.67), a voltage of 5.05 V is needed to start the system.

The "power good" pin (PGOOD) goes high when the output is in regulation. If a capacitor is placed on the output (V_{OUT}), PGOOD would signal when the capacitor was fully charged. This means that if the output capacitor was correctly dimensioned to supply one full cycle of the WSN-node (wake up, measure, transmit, sleep etc.), the PGOOD pin could be used to wake it up.

$$C_{OUT} = (V_{OUT+} - V_{OUT-}) \frac{I_{LOAD} - I_{BUCK}}{t_{LOAD}} \quad (9.1)$$

The optimal capacitance of the output capacitor can be found by equation 9.1^[35], where V_{OUT+} is the value of the selected output voltage (3.3 V in this case) when PGOOD goes high and V_{OUT-} is the minimum operational voltage of the external device. I_{BUCK} is the average current being delivered from the buck converter, typically 50 mA. I_{LOAD} is the current consumption of the device, while t_{LOAD} is the required ON-time of the external device.

If this wake-up behavior is not facilitated by the connected node, a simple N-channel MOSFET (figure 9.2) could be driven by the PGOOD pin to connect V_{OUT} to the load device whenever the capacitor is fully charged. Once the device is powered, it can take over control of the MOSFET gate and turn it off as long as PGOOD is no longer 'high'. This can be an active decision by the external device when its task is complete, or a result of it depleting the energy in C_{out} and shutting off.

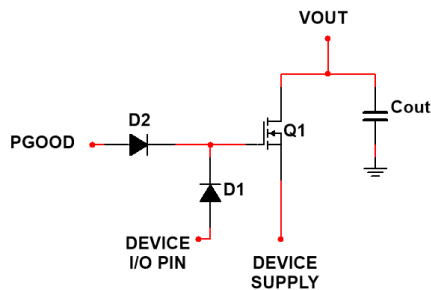


FIGURE 9.2: PGOOD driving gate of N-channel MOSFET

In this project, as no external device or node is specified, the output capacitance is selected to 100 μ F.

The LTC3588EMSE-1#PBF was chosen as the specific device for this project. It comes in a small 3×3 mm 10-pin eMSOP plastic package which has extending leads. This makes the package solderable by hand while maintaining a small footprint.

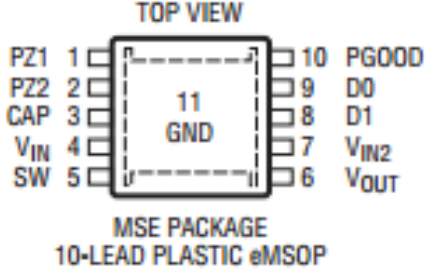


FIGURE 9.3: Pinout of LTC3588 DC-DC step-down (buck) converter in 10-eMSOP package^[35]

9.1.2 Power storage

Since the voltage from the power storage will vary depending on its state of charge, it would be beneficial to store the power at the input of the DC-DC converter, and not at the output. This would enable the DC-DC converter to convert the voltage from the power storage to the desired output voltage.

The discussion in section 5.1 found that the choice of power storage was in fact a choice between batteries and supercapacitors. As the power storage will be placed at the input of the DC-DC converter, and the expected input from the piezoelectric transducer is up to 40 V (table 8.3) or 20 V if clamped by the LTC3588 input diode, batteries may be the best solution. Supercapacitors are, as discussed in section 5.1, low voltage devices and most commercially available^[17] supercapacitors are rated at 16 V or lower. Two or more supercapacitors could be connected in series to increase their voltage tolerance, dividing the voltage between the two devices, but this would take up much space as the supercapacitors can be quite large. The decision was made to choose batteries in this project.

Batteries

*Cymbet*¹ produces small solid state batteries with capacities ranging from 5 to 50 $\mu\text{A h}$, called EnerChip™. These batteries are available as SMD, and come in DFN packages ranging from 4×5 mm to 8×8 mm. The batteries are also available as 'Bare Die' for implementing inside other ICs.

¹www.cymbet.com

The 50 $\mu\text{A h}$ version (EnerChip CBC050) of these batteries were chosen for this project, as they can promise small package backup power with low leakage. Thousands of recharge cycles^[36] could also be beneficial for long time operating in an energy harvesting application. Being able to solder the batteries directly to the PCB was also considered a large advantage.

Since the LTC3588 requires a voltage of 5.05 V to start, the voltage of the power storage should remain higher than this as long as there is power available. The nominal voltage of the CBC050 is 3.8 V and the 'Discharge Cutoff Voltage' is 3.0 V^[36], meaning that at no charge-state will the battery voltage surpass the voltage needed to start the DC-DC converter. Because of this, two CBC050 batteries in series is needed to power the system. Then the voltage range will rise to 6 - 7.6 V which is above the desired minimum voltage.

With this setup there would be a backup supply of 380 μWh . This does not sound like much, but with today's low power devices it could actually be enough to power a microcontroller for many hours. In the design phase, footprints for two additional batteries in parallel will be added. This will enable doubling of the capacity to 760 μWh , if the need should arise.

Charger(s)

To charge the batteries, the LTC4071 from *Linear Technology* was chosen. It is a simple shunt-type charger for lithium batteries with low battery disconnect and pin-selectable charge voltage^[37]. Since these chargers only charge one cell at a time, two of them are needed in this design. The charge voltage we set to 4.1 for the CBC050 batteries, the possibility of thermal feedback from the lithium cell was not implemented. This means that the batteries will not charge before the rectified input voltage (V_{IN}) of the LTC3588 reaches at least 8.2 V.

The shunt resistor (R_{SHUNT}) in the schematic was chosen to 1500Ω as recommended in the datasheet^[37].

9.1.3 Passives

The power manager device would require a handful of passive components like capacitors, resistors and inductors. Since minimizing the amount of power lost in this project is important, some considerations must be done when selecting these components. Also, since the power manager could be exposed to quite dramatic vibrations weight and robustness of components should also be considered.

One inductor is needed in this project; The switching inductor for the DC-DC converter. Inductors can often be some of the larger components on a PCB, but due to the low maximum current through this inductor^[35] a smaller wirewound SMD inductor with a 1210 footprint could be chosen.

Resistors are pretty straight-forward and require no special considerations. For this project a standard resistor footprint of 0805 is chosen.

When choosing capacitors for the project, some care must be taken to ensure both low leakage and mechanical stability. Dealing with capacitance requirements in the range of 1 - 100 μF Aluminium or Tantalum electrolytic capacitors were the main contending technologies. Tantalum capacitors were chosen due to quite low leakage current (e.g. 0.001 CV for 293D10X96R3^[38]), but also low weight and physical size which is beneficial in a vibrational environment. Tantalum capacitors are however quite expensive compared to aluminium electrolytic capacitors.

9.2 Schematics

The schematics for this project are heavily based on reference designs in the datasheets of the DC-DC converter^[35], commercial transducer^[31] and battery charger^[37].

All schematics presented in this section can be found in full size appended at the end of this document.

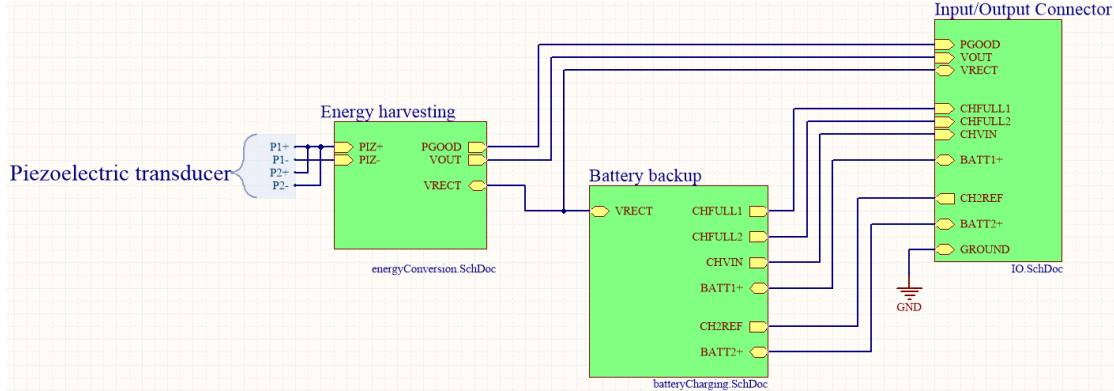


FIGURE 9.4: Top level schematic, showing schematic relationships in the project

Figure 9.4 shows the top-level relationships between the three sheets; "Energy harvesting", "Battery backup" and "Input/Output Connector".

Figure 9.5 shows the LTC3588 DC-DC converter and the required passives. Output voltage selection via D0 and D1 pins are emphasized.

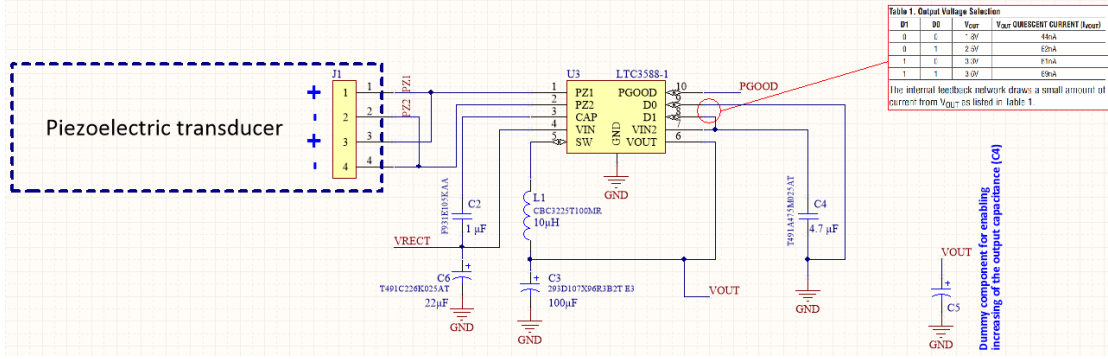


FIGURE 9.5: Schematic of DC-DC converter and related passives

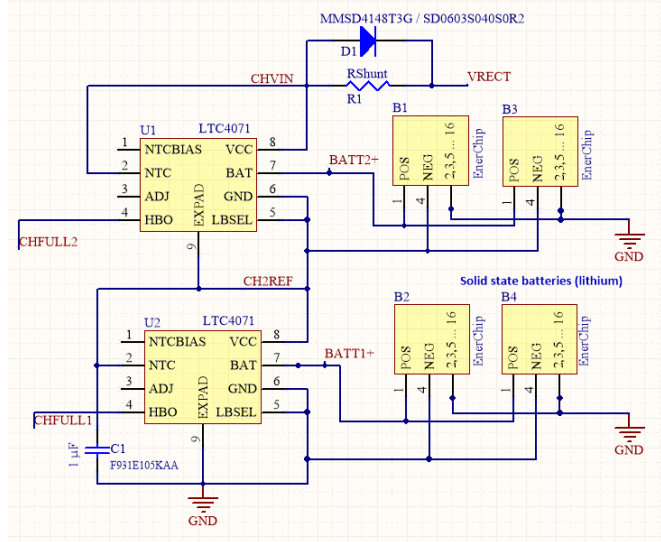


FIGURE 9.6: Schematic of battery backup, including batteries and charger circuits

In figure 9.6 the schematic of the batteries and charging circuits can be seen. The charge (float) voltage is set to 4.1 V by leaving the ADJ-pin floating^[37]. The shunt resistor (RShunt) limits the charging current and enables the chargers to dissipate any excess power (when batteries are full) as heat. The diode (D1) is added to reduce the power loss in the shunt resistor when the system is running on batteries.

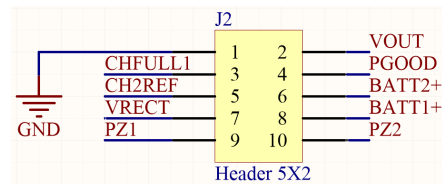


FIGURE 9.7: Schematic of Input/Output connector, showing the available signals and pinout

The input/output connector (fig. 9.7) is the connection between the energy harvester and the device it is powering (or for testing purposes, the measurement system). It is

a 10-pin (5x2) shrouded right angled connector with 2.54mm pitch. Signal descriptions for all pins can be seen in table 9.1.

Pin no.	Pin name	Description
1	GND	Ground connection
2	VOUT	Main connector for output power
3	CHFULL1	Logic signal for full battery
4	PGOOD	Power good logic output signal
5	CH2REF	Negative reference for 'BATT2+' pin'
6	BATT2+	Positive battery terminals (B1 & B3)
7	VRECT	Rectified voltage input
8	BATT1+	Positive battery terminals (B2 & B4)
9	PZ1	Piezoelectric terminal 1 (+)
10	PZ2	Piezoelectric terminal 2 (+)

TABLE 9.1: Pinout and signal description of main I/O connector

The VOUT pin is the main power output of the system. Any external device or WNS-node must be connected to this pin. The CHFULL1 pin tells the external system that the batteries of the energy harvester is full. This can indicate whether or not the system is running on backup or not. The PGOOD pin is, as discussed in section 9.1.1 used to signal that the output voltage is in regulation. CH2REF acts as 'ground' reference for the 'BATT2+' pin and is essential the mid-point between the two series-connected batteries. BATT2+ and BATT1+ are the positive terminals of the two batteries. Having these in the input/output connector enables the system to have large external batteries instead of, or in addition to the on board solid state batteries. VRECT is the rectified input voltage, this pin can be used to power the system from an external source and e.g. charge the batteries before deployment. The piezoelectric terminals are added to the input/output connector mostly for testing purposes, but it could be used by an external device to analyze the harvested power or even as a measurement of acceleration if calibrated correctly. Care must be taken to not load these terminals as this could degrade the performance of the energy harvester.

9.3 PCB design

All PCB designs depicted in this section can be found attached and enlarged at the end of this document.

The PCB design is pretty straight forward, and minimalist. It is designed with a left-to-right approach in mind, where the power enters through the piezoelectric connector on the left and the DC-DC converter. The input/output connector is located to the far left, while the batteries and charger are kept in the middle of the board. Size is important

and keeping things small was a priority, but since the board were to be soldered by hand some spacing had to be added between components. Two M3 screw-holes were also added to fix the PCB inside casing.

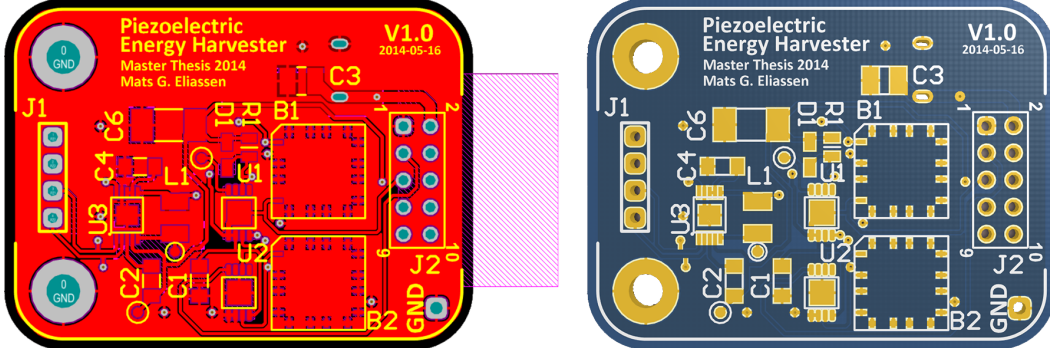


FIGURE 9.8: Gerber (left) and 3D view (right) of top-layer of power manager

All components are kept on top of the PCB, but the footprints for the extra batteries (discussed in section 9.1.2) are placed on the bottom side. An area (C5) for adding a larger output capacitor, SMD or through-hole, is also added to the bottom layer.

Figure 9.8 shows the top-layer design, while figure 9.9 shows the bottom-layer design.

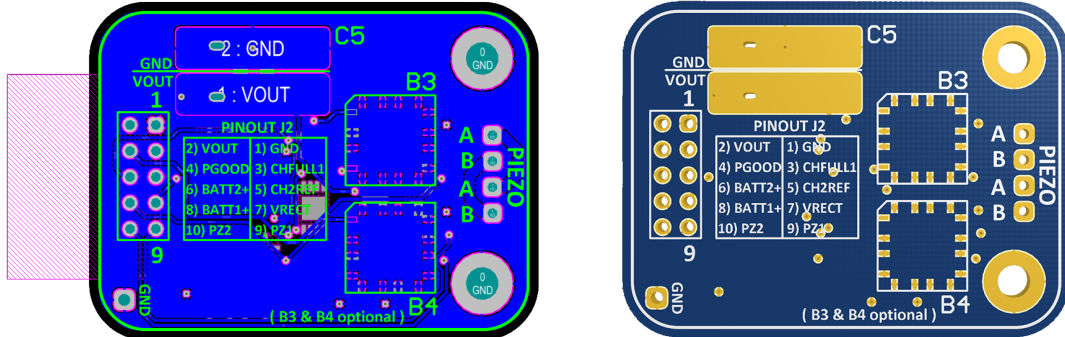


FIGURE 9.9: Gerber (left) and 3D view (right) of bottom-layer of power manager

3D models were added to all components in the design to ensure detection of component collisions and help in the design of the casing . Figure 9.10 shows the isometric view of the PCB design with 3D-modeled components.

The dimensions of the final PCB design are 44×33 mm.

9.4 Finished device

The PCB designs were sent to a professional fabricator². Once the finished PCBs arrived they were soldered using a combination of soldering irons and hot-air stations. Kapton®

²www.elprint.no

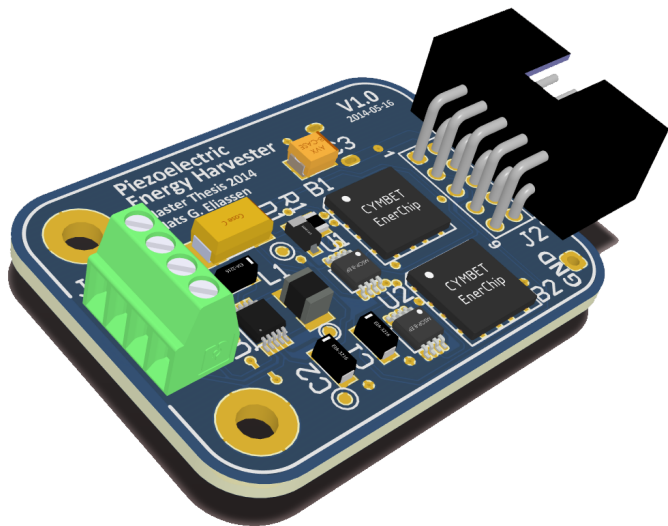


FIGURE 9.10: Isometric view of PCB design with added component 3D-models

tape was added to the exposed unsoldered pads on the bottom of the PCB to limit the risk of short-circuiting the device. The final product can be seen in figures 9.11 and 9.12.

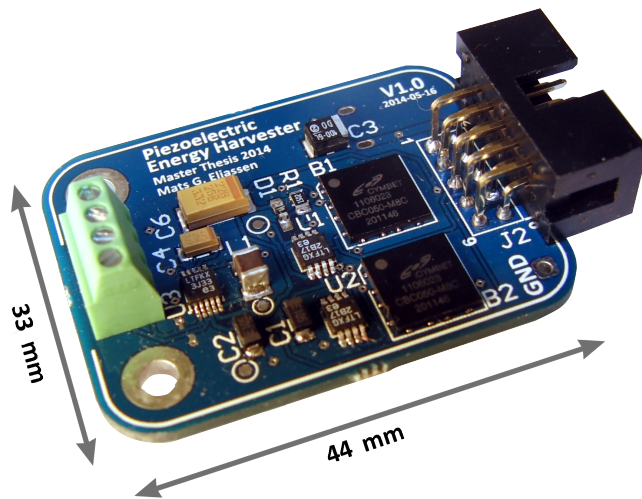


FIGURE 9.11: Finished power manager device (top view)

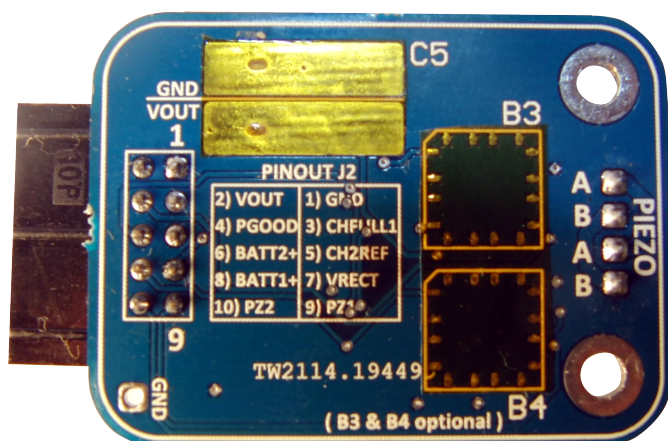


FIGURE 9.12: Finished power manager device (bottom view)

Chapter 10

Casing

The casing was designed with the four main purposes from section 6.3 in mind. It was designed as four separate parts; the box, the lid and a two-part clamping system.

Mechanical drawings of each part of the casing can be found attached at the end of this document.

10.1 The box

The box is the biggest and most important part of the casing design. It is secured to the mounting surface by the "wings" seen in figure 10.1. These wings are custom designed to fit the vibrator test rig at Kongsberg Maritime in Trondheim, but can easily be redesigned for other mounting options. It has a opening for the power manager input/output connector, and mounting holes for the power manager PCB. Along the top edge of the box, a small groove is cut into the wall. This is to allow the lid (figure 10.2) to clip on and off. Another groove can be found along the inner bottom edge opposite of the connector opening. This is to allow sliding the transducer clamp (figure 10.3 and 10.4) back and forth and thus tuning the natural frequency of the transducer. The box design is scalable in the length direction (Y) to allow adjustment for different transducer lengths.

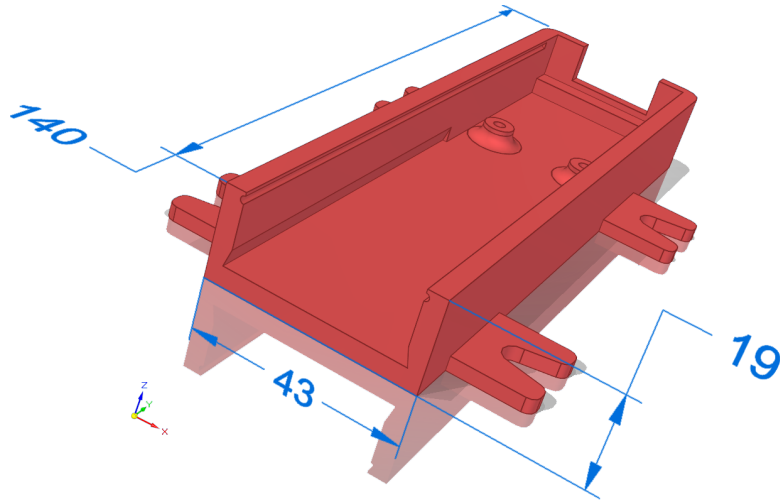


FIGURE 10.1: Rendering of bottom/main part of casing, 'the box'. Dimensions in mm.

10.2 The lid

The lid clips onto the box structure, enclosing the inner components and protecting them from contaminant objects and fluids. The lid also serves another important purpose. Once the lid is clipped into place, it pushes down on the transducer clamp (figure 10.3 and 10.4) causing it to tighten around the transducer and ensure good conductance of vibrations from the mounting surface to the transducer base.

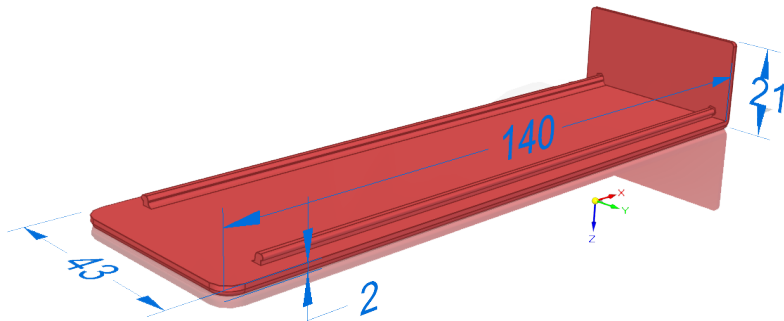


FIGURE 10.2: Rendering of top part of casing, 'the lid'. Dimensions in mm.

10.3 The transducer clamp

The transducers clamp consists of two separate pieces (fig. 10.3 and 10.4) which are to be closed around the transducer and fitted into the groove at the bottom of the box (fig 10.1). The transducers can then be shifted along the length of the transducer to tune its natural frequency. Once the lid is secured the clamp is refrained from further movement. Figure 10.5 can help visualize this feature.

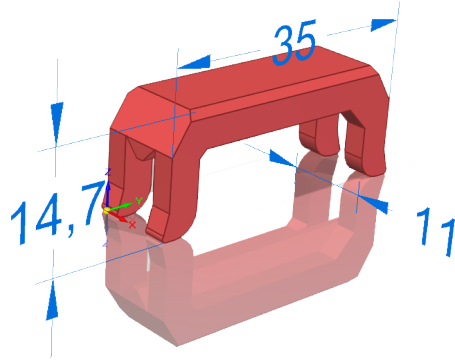


FIGURE 10.3: Rendering of top part of transducer clamp. Dimensions in mm.

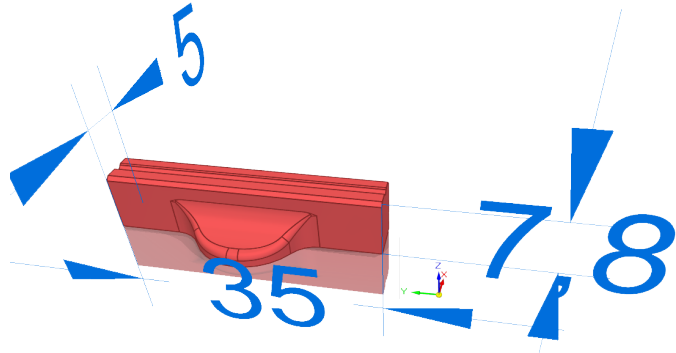


FIGURE 10.4: Rendering of bottom part of transducer clamp. Dimensions in mm.

10.4 Assembled view

The assembly of the 3D-model can be seen in figure 10.5. This illustrations demonstrates how the pieces relate to each other and helps understand the mechanical parts. It also serves as an excellent tool for test-fitting parts before 3D-printing, thus limiting iterations and manufacturing time. Lid is not present in this presentation view.

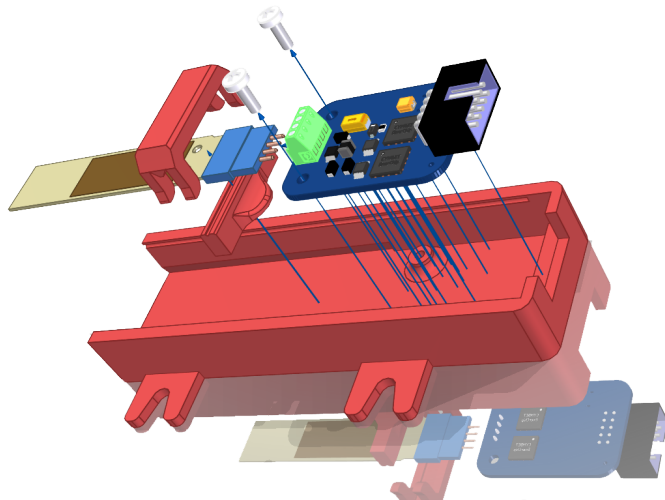


FIGURE 10.5: Exploded view of casing with mounted power manager and V21BL transducer. No lid.

10.5 Finished product

The modeled casing was 3D-printed in PLA as mentioned in section 6.3. After the parts were 3D-printed, all parts of the energy harvester fit nicely together.

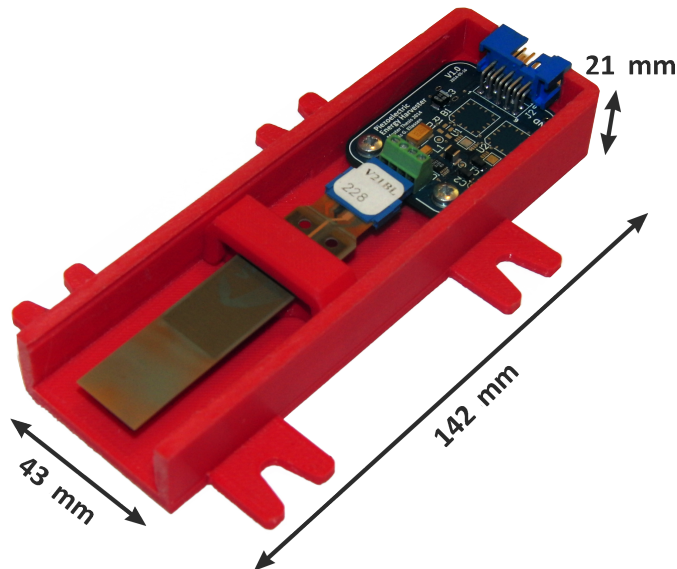


FIGURE 10.6: Photo of 3D-printed casing with power manager, transducer clamps and V21BL transducer mounted. No lid.



FIGURE 10.7: Photo of 3D-printed casing with power manager, transducer clamps and V21BL transducer mounted. Lid closed.

Chapter 11

Measurement system

11.1 Data acquisition hardware

The data acquisition system had to be made of components that could not significantly affect the energy harvester by either excessive loading the system, or supplying the system through an 'outward' leakage current. The choice fell on the CompactDAQ platform from National Instruments^[28] for data acquisition and the LabVIEW environment for data analysis. Several ADC modules exists for the CompactDAQ platform, but in this case the NI9205 and NI9207 were utilized.



FIGURE 11.1: The NI9205 data acquisition module^[28]

The NI9205 is a 32 channel 16-bit analog to digital converter with a voltage range from -10 to 10V. It supports both single-ended and differential measurements. It has a maximum sample rate of 250 kS/s, which means $f_{samp,max} = \frac{250 \times 10^3}{n}$ Hz, where n is the number of utilized channels.

The NI9207 is very similar to the NI9205, but offers 16 channels of 24-bit resolution. It has the same voltage range of -10 to 10V as the NI9205, but has a much slower conversion time of 2 ms (High-Speed mode) per channel or $f_{samp,max} = \frac{1}{n \times 2 \times 10^{-3}}$ Hz.



FIGURE 11.2: The NI9207 data acquisition module^[28]



FIGURE 11.3: The compactDAQ cdaq-9174 data acquisition platform^[28]

The two ADC modules are combined in one measurement system through the CompactDAQ 9174 4-Slot USB Chassis which feeds data from the modules to the LabVIEW interface through a USB connection.

For the measured data to tell us anything about the performance of the energy harvester, an accelerometer is needed to measure the amplitude and frequency of the mechanical excitation. The *IMU Analog Combo Board*^[39] from *SparkFun Electronics* was utilized. It has several sensors on-board, but in this project we will only be using the ADXL335^[40] accelerometer from *Analog Devices*. It runs on a 3.3 V supply and has a measurement range of ± 3 g which translates to 2.12 g (RMS). The sensitivity is 300 mV g^{-1} .

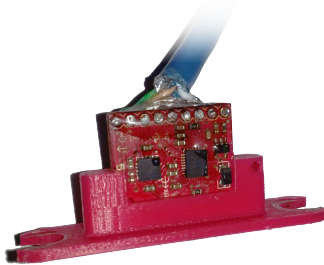


FIGURE 11.4: The accelerometer setup

Figure 11.4 shows the IMU board in a small 3D-printed bracket with a CAT-6^[41] network cable used to supply current to the board. The same cable connects the output signal

of the analog accelerometer to the NI9205 acquisition device. To ensure mechanical robustness, the cable is soldered to the board, then covered in epoxy.

During the final testing of the energy harvester, the IMU board was found to have a low-pass filter added to its accelerometer X-axis output pin rendering it useless above 10 Hz. This filter (capacitor) was removed from the original board.

11.2 Data visualization and analysis software

For data visualizing and analyzing the acquired data, the LabVIEW software platform was utilized. A front-panel GUI was designed (fig. 11.5) to visualize the output data.

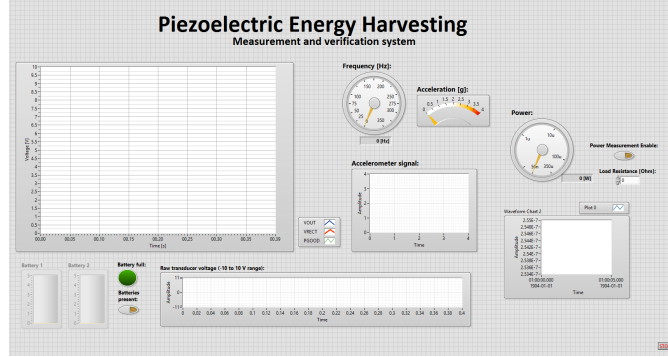


FIGURE 11.5: Graphical User Interface of LabVIEW software

The parameters measured by the system are:

- Output voltage
- Rectified input voltage*
- Power-good pin of LTC3588 IC
- Battery voltages for both batteries
- Battery full indicator pin
- Accelerometer output signal
- Raw voltage from piezoelectric input*

* Since both the NI9205 and NI9207 have a maximum input voltage of 10 V the piezo voltage and the rectified input voltage can quickly rise above the measurable range.

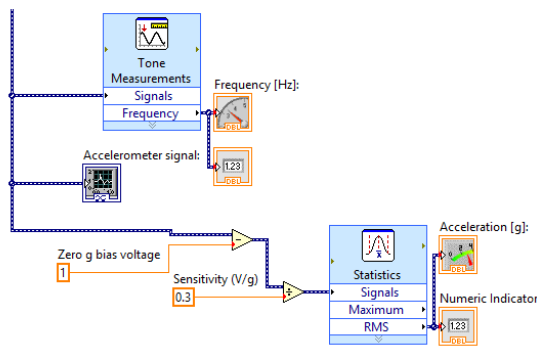


FIGURE 11.6: Conditioning of accelerometer signal in LabVIEW

Most of these acquired data is displayed as raw voltages, but the accelerometer output needs some conditioning. Figure 11.6 shows how this signal is conditioned and displayed in terms of g's (RMS). The accelerometer signal is also used to display the frequency of the mechanical excitation.

To measure the power, a resistor needs to be connected between the output voltage (V_{OUT}) and ground (GND) of the energy harvester. Care must be taken to not select a to low resistor, as the maximum output current of the LTC3588 is 100 mA^[35].

$$R_{min} = \frac{V_{OUT,max}}{I_{max}} = \frac{3.3 \text{ V}}{100 \text{ mA}} = 33\Omega \quad (11.1)$$

The value of the added resistor is entered in the LabVIEW GUI, and used for calculating the power. As there are many sources of hysteretic behavior in the system, one of them being the input voltage of the LTC3588, the voltage over the added output load (resistor) is integrated over a long period of time, typically 4 seconds. The voltage is then divided by the integration time and used to calculate the average power dissipated in the resistor. The implementation of this in LabVIEW can be seen in figure 11.7.

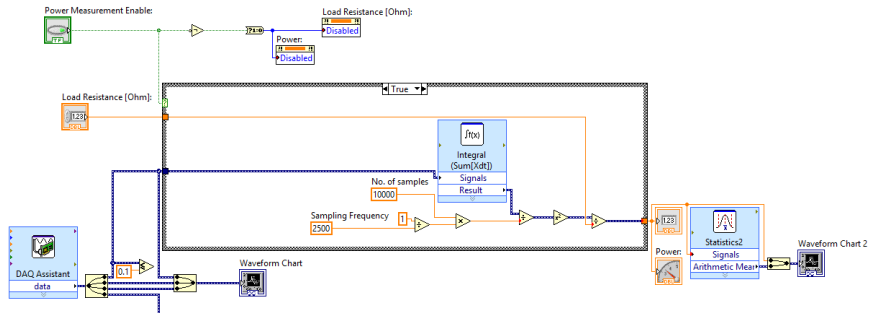


FIGURE 11.7: Implementation of power measurement in LabVIEW

Part V

Results and Discussion

Chapter 12

Results

12.1 Testing at Kongsberg Maritime

Early in the testing process, the whole energy harvester with casing, power manager and different transducers were brought to Kongsberg Maritime's (KM) offices a Lade in Trondheim. The whole energy harvester was mounted to a large vibrator and tests were ran.

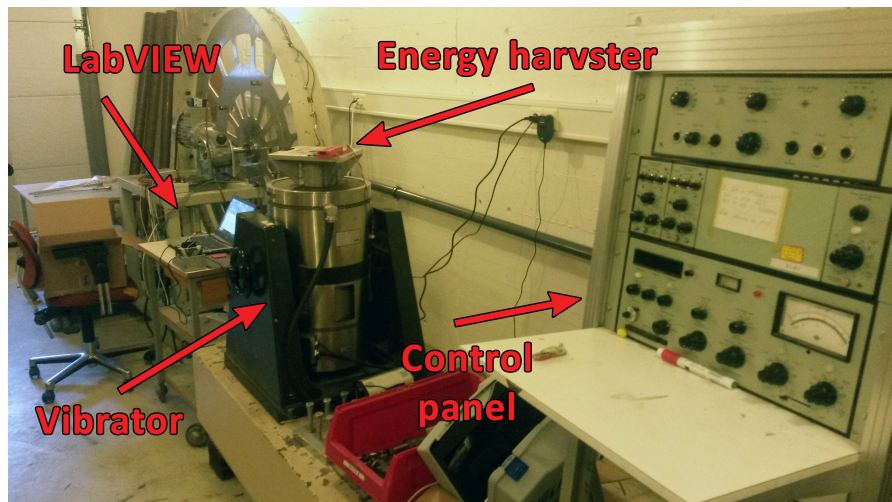


FIGURE 12.1: Overview of test setup at Kongsberg Maritime

Accelerometer readings seemed a little off during these tests, and the powerful vibrator running at max was only capable of producing just over 2 g's. It was later discovered that the accelerometer discussed in section 11.1 had a low-pass filter mounted on its signal output, rendering it useless above 10 Hz.

This rendered most of the test results useless, but some tendencies could be identified. The first noticeable tendency was hysteresis regarding resonance. The vibrator would

need to be tuned to the transducers natural frequency with a very small margin of error (approx. ± 1 Hz) before entering resonance. Once resonance occurred, the vibrator frequency could be tuned several hertz up or down while the transducer would keep resonating.

The test results showed a maximum of $200 \mu\text{W}$ output power. Although no reference acceleration was present, the vibrator was pushing the transducers very hard. An interesting observation was that while the power output was believed to be quite low compared to the violent (again, no reference was available) vibrations, the bandwidth (-3dB) was measured to approx. 20 Hz, which was much more than expected.

12.1.1 Transducer clamps

The transducer clamps should enable the user to adjust the natural frequency of the transducer. To test this, no accelerometer reference was needed and the test could be performed at KM by setting the clamp to its extreme positions and sweeping through the frequencies with the vibrator control. Once resonance could be visually confirmed, a frequency adjustable strobe-light (HELIOTROB Compact-75) was used to verify the frequency. Once aliasing occurred, and the transducer tip seemed to be stationary at a deflected position, the frequency of the system could be read from the strobe-light display.

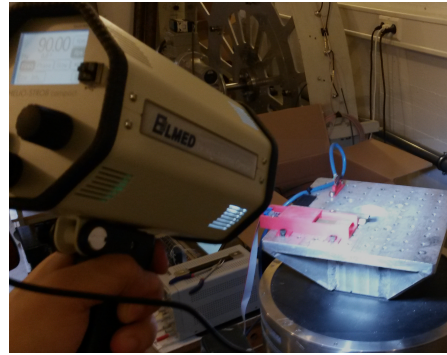


FIGURE 12.2: Testing adjustable range of transducers with strobe light (HELIOTROB Compact-75)

Both the V21BL and the PVDF transducer could be adjusted over a large range. The V21BL could be adjusted from 82 Hz to 450 Hz, while the produced PVDF transducer could be adjusted from 28 Hz to 51 Hz. This shows that the designed clamping system works as intended.



FIGURE 12.3: Sub-woofer excitation setup.

12.2 Testing at the Lab (HiST)

When the test results from the test at KM was deemed useless due to the discussed accelerometer failure, a new test was set up. This time at the Lab at HiST due to time restrictions. The tests were done by clamping the transducers in a 3D-printed clamp mounted inside the frame of a 12 inch sub-woofer. This sub-woofer was driven by an audio amplifier (Cambridge Audio P500), and the control signal was generated by a function generator (TTi TG2511). The accelerometer configuration (with its low-pass filter removed) was glued to the structure to ensure good measurement of the acceleration. The sub-woofer, clamp and transducer setup can be seen in figure 12.3. The clamp is set by 2 M3 screws which make sure the transducer is held firmly in place.

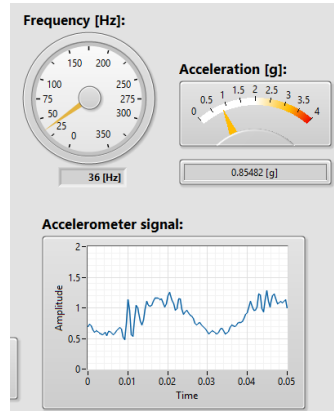


FIGURE 12.4: Non-uniform and noisy acceleration data due to eigenfrequencies in the system.

This setup was found to be surprisingly effective, but the displacement is not uniform in the Z-direction (up). This could affect the end results. Especially around 32 - 38 Hz, there seems to be a lot of eigenfrequencies in the system and a lot of movement in the XY-directions. Figure 12.4 shows accelerometer data at 36 Hz, and the presence of acceleration at higher frequency is clearly visible.

12.2.1 Transducer voltage

Testing the output voltage of the produced transducer with 110 µm PVDF film. *Note that in this test, both the PVDF layers of the transducers are connected in series.*

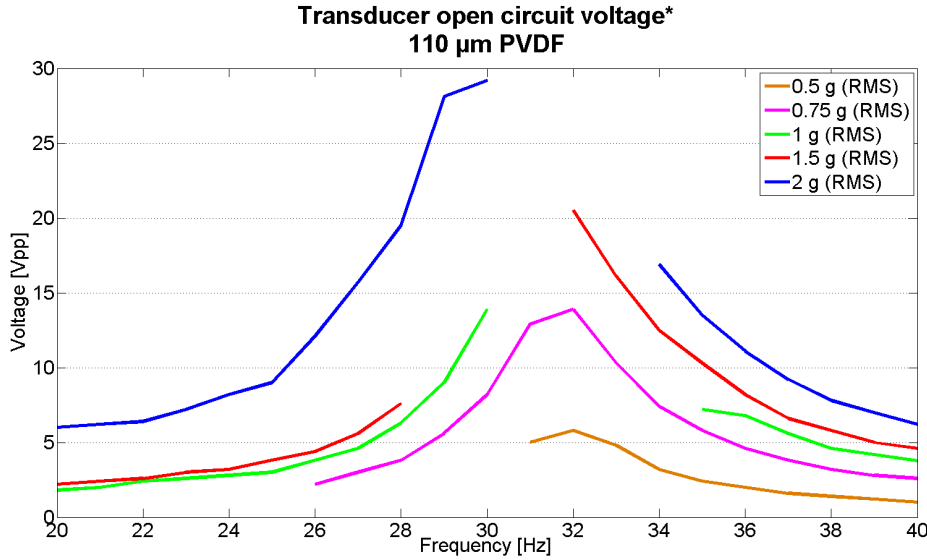


FIGURE 12.5: Open Circuit* voltage (peak-to-peak) of produced transducer. 110 µm PVDF film. (*($10\text{ M}\Omega$) Oscilloscope probes loading the terminals.)

The voltage was read on an oscilloscope (DSO-X 2002A) with high impedance probes ($10\text{ M}\Omega$, N2862B) while the acceleration was displayed in the LabVIEW GUI discussed in chapter 11.

Figure 12.5 shows the output voltage for different frequencies and amplitudes of excitation. The output voltage is as expected higher for higher levels of excitation (g). The highest voltage is found at approx. 30 Hz which is close to the 28 Hz natural frequency estimated by the model (ch. 7). Small deviations in how the transducer is clamped may shift the natural frequency of the system from measurement to measurement.

One interesting behavior observed was that when the transducer was nearing resonance, the output voltage would sometimes collapse. This is illustrated in the graph by the missing data points and by an oscilloscope screenshot (fig. 12.6).

Generally, the produced transducer shows promising output voltages ranging from 0 to 30 volts (peak-to-peak). Even at low excitation amplitude (0.5 g) the output peak-to-peak voltage reached over 5 V at resonance.

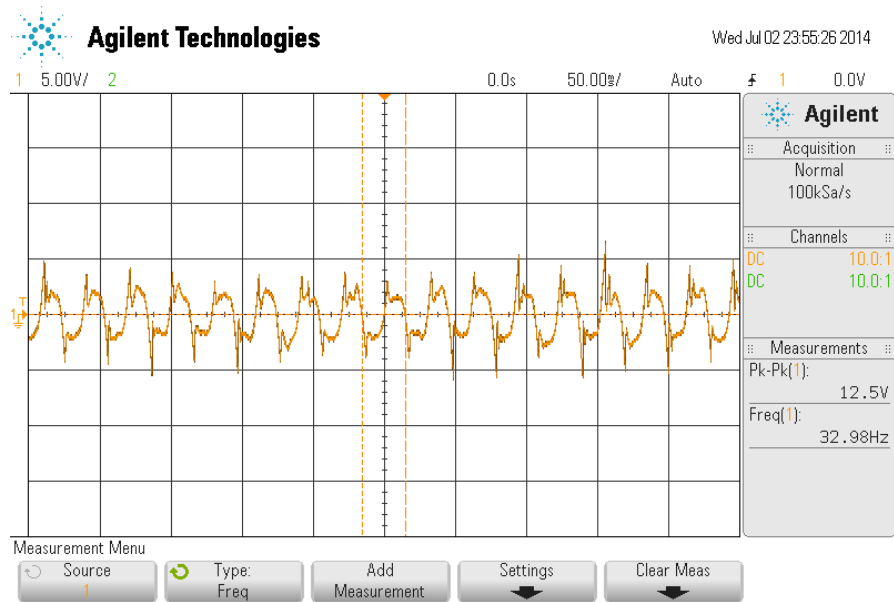


FIGURE 12.6: Collapsing output voltage (peak-to-peak) of PVDF transducer. 2 g mechanical excitation @ 33 Hz

12.2.2 Harvested power

As mentioned above, the test results from the test at KM were invalid. This meant new test had to be done, and due to time-restrictions they had to be performed at HiST in the sub-woofer setup earlier described.

PVDF transducer - No added mass

The PVDF transducer (110 µm) was mounted in the shaker (sub-woofer). The terminals of the transducer were connected to the power manager via test leads.

No output power could be measured by the LabVIEW measurement system, even when pushing the transducer to its maximum with regards to deflection. To investigate this, the oscilloscope was utilized to measure the input voltage to the LTC-3588.

Figure 12.7 shows that the PVDF transducer is only capable of charging the input capacitor to approx. 4 V. This is not enough voltage for the DC-DC converter which needs 5.05 V to trigger its hysteretic input.

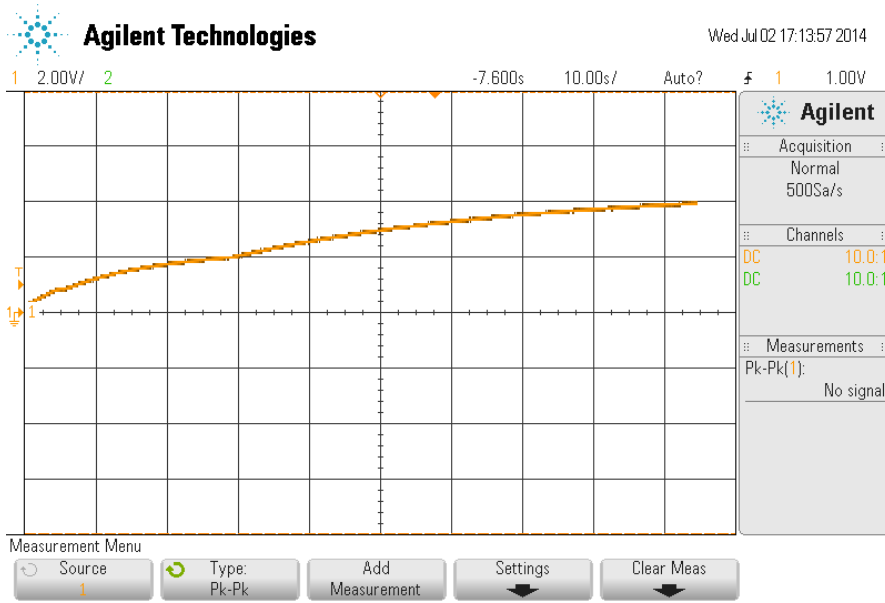


FIGURE 12.7: Input voltage of LTC-3588 with PVDF transducer connected. High vibration amplitude ($\gg 2.12$ g) with transducer in resonance.

V21BL transducer - No added mass

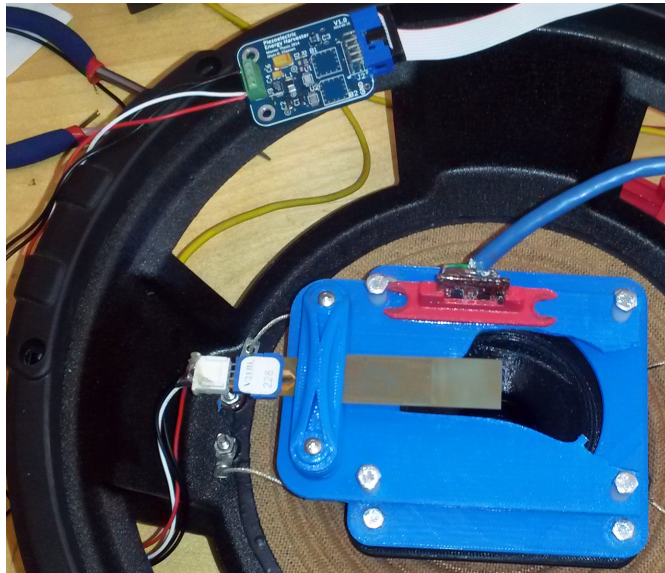


FIGURE 12.8: V21BL transducer mounted in shaker. Accelerometer and power manager visible.

The V21BL transducer was mounted in the same way (fig. 12.8) as the PVDF transducer. The frequency was varied over a large area to identify the resonance regions, and then a sweep over 40 Hz was performed while varying the amplitude of vibrations between 1, 1.5 and 2 g (RMS).

Figure 12.9 shows the measured power output. At 1 g, the maximum output power was 110 μ W at 176 Hz. Increasing the vibration amplitude to 1.5 g showed an increase in

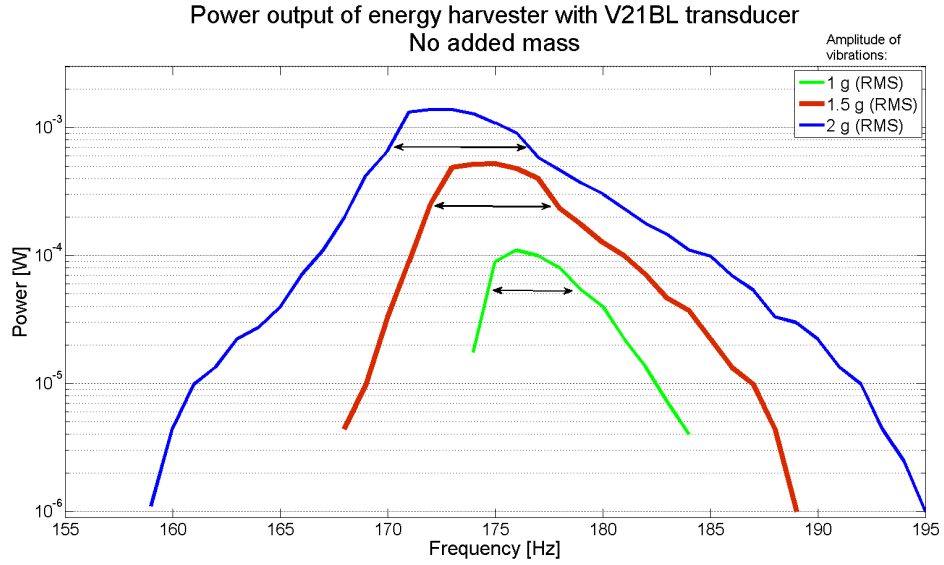


FIGURE 12.9: Harvested power from V21BL transducer for different amplitudes of vibration.

power to $522 \mu\text{W}$ at 175 Hz . Finally, increasing the amplitude to 2 g showed an output power of 1.382 mW at 173 Hz .

Another important parameter is the bandwidth. It is marked in the graph (fig. 12.9) by arrows. For 1 g the bandwidth (-3 dB) is approximately 4 Hz , 5 Hz at 1.5 g and 6 Hz at 2 g .

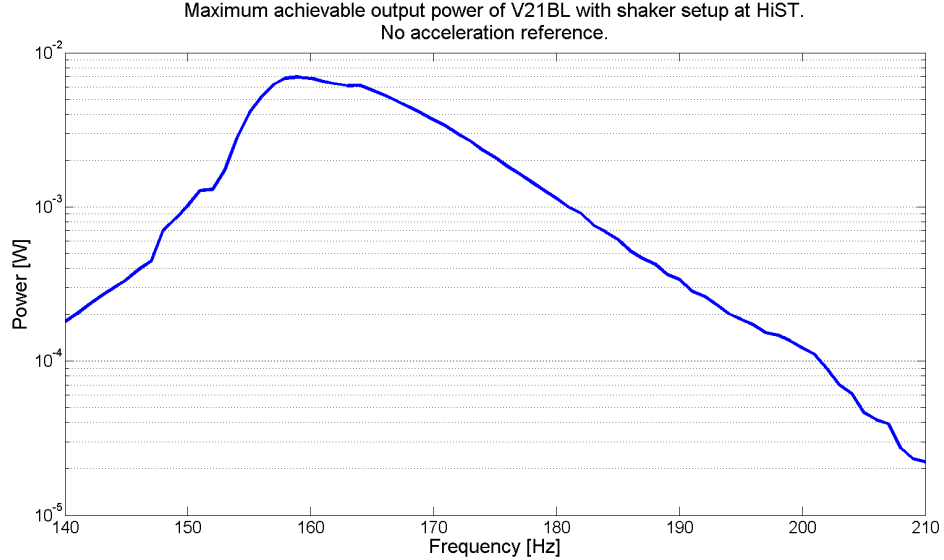


FIGURE 12.10: Maximum achievable output power of V21BL transducer with shaker setup at HiST. No acceleration reference.

It could also be interesting to investigate what kind of power levels were feasible to harvest at extreme conditions. To investiage this, the shaker was ran at maximum

and a frequency sweep was performed. The levels of excitation in this test was way outside the range of the accelerometer ($\pm 3\text{ g}$), and because of this, no reference of the acceleration exists for this measurement. The maximum achievable power output with the V21BL transducer, with no added mass, in the sub-woofer setup is 6.96 mW at 159 Hz.

V21BL transducer - Added mass

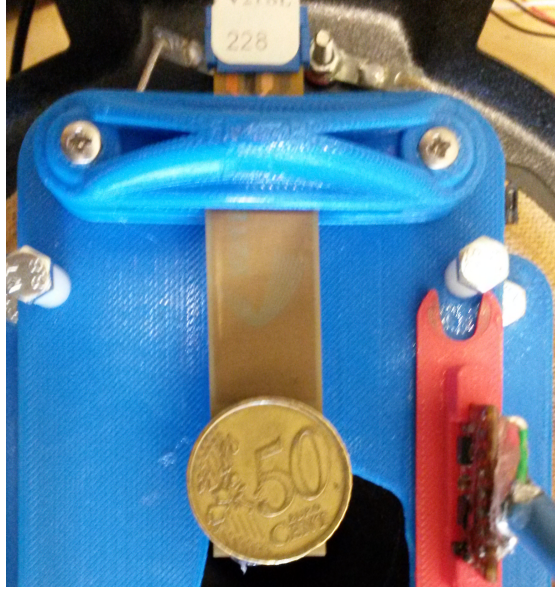


FIGURE 12.11: V21BL with 50 cent euro-coin glued to transducer tip.

To force the V21BL down to a lower frequency range, a mass was added to the end of the transducer. As no calibrated weights were available, a 50 cent euro-coin was hot-glued to the transducer (fig. 12.11). The 50 cent euro-coin has a known mass of 7.8 gram^[42].

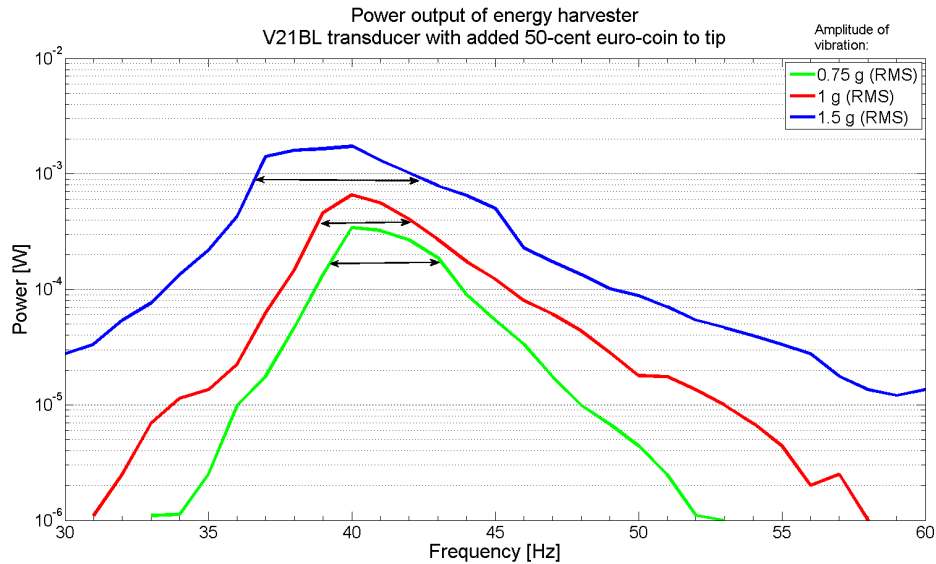


FIGURE 12.12: Power output of energy harvester. V21BL transducer with added 50-cent euro-coin to tip

Figure 12.12 shows the output power of the energy harvester with the weighed down transducer. At 0.75 g, the maximum output power was 342 μ W. Increasing vibrations to 1 g showed an increase in power to 657 μ W. Finally, increasing the amplitude to 1.5 g

showed an output power of 1.736 mW. For all levels of excitation, the power peak was found at 40 Hz.

The bandwidth (-3 dB) of the system with the weighed down transducer was approx. 6.5 Hz at 1.5 g, 3.8 Hz for both 1 and 0.5 g of base acceleration.

Battery backup

It was hard to do thorough testing of the battery system, as this requires a long time and hundreds of charge cycles. Functionality testing would have had to suffice in this project.

When connecting the charger input to a power supply at 10 V the chargers responded by immediately connecting the batteries and a voltage of 8.2 V could be measured across the two series-connected batteries. This corresponds to the 4.1 V charge voltage of each cell. Once the batteries are charged, the 'battery full' pins of the chargers go to a logic high state. The output voltage of the DC-DC converter is maintained at 3.3 V with no external power supply, meaning the power storage feature is functioning.

Chapter 13

Discussion

Transducers

Producing custom transducers from FR4 and PVDF film was achievable by hand, but it took some tries to refine the process. Adhering the PVDF film to the FR4 and letting it dry completely before milling it in a CNC mill would have been a better approach.

The one (of 3) transducer that was successfully built (110 µm film thickness), showed promising results regarding its open-circuit output voltage (film elements in series) with a peak-to-peak voltage of up to 30 V. This was more than what was specified for the commercial transducer.

When connecting the PVDF transducer to the power manager device it could not support an input voltage of over approx. 4 V which is less than the start-up voltage of the DC-DC converter. Looking back to figure 12.7 it is clear that the voltage slowly rises to approx. 4 V before flattening out. The input capacitors (T491C226K025AT^[43] and F931E105KAA^[44]), have a total specified leakage current of 1.38 µA at this voltage. Adding the 450 nA UVLO quiescent current of the LTC3588 and the produced power is 7.32 µW. This is very little, but if a DC-DC converter with a lower input threshold voltage had been used, the adaptive impedance matching could have increased the power output of the transducer. The collapsing output voltage of the PVDF transducer observed in figure 12.6 was very odd, and no explanation could be found to this behavior.

One of the main reasons for producing custom transducers were to enable harvesting of low frequency vibrations. Figure 12.12 showed that a 'high frequency' commercial transducer could be tuned down in frequency by adding a mass to the tip. Using this approach also saves space, as the 'high frequency' transducers are shorter in length. This limits the benefits of the custom transducers, even if the power output had been similar.

When adding an end mass is preferred, the mass could easily consist of a permanent magnet glued to the transducer. If an conductive coil was placed in the vicinity of the magnet as the transducer tip displaced, it would cause induction of current in the coil which could contribute to the total power output of the system. This was not implemented in this project due to time restrictions, but could be an interesting next step.

Power Manager

The power manager did its job and the LTC3588 energy harvesting DC-DC converter performs well. It does a good job of harvesting the energy from the piezoelectric transducer and making it available as a regulated 3.3 V output. Once the input voltage (rectified) climbs above approx. 8.2 V the LTC4071 chargers starts charging the solid state batteries, saving the excess power for later use.

As discussed earlier in this chapter, using a buck-boost converter instead of a buck-converter could make it easier to use low-output piezoelectric materials. Lowering the input voltage threshold of the buck-converter would also contribute in the same direction.

The input/output connector will allow interfacing to an external device, giving it access to the generated power, PGOOD pin, piezo elements, rectified input voltage battery terminals and battery-full pins of the charger ICs. Chosing not to solder the solid state batteries to the board will allow the addition of external batteries for increased capacity.

Casing

Since the casing was custom built for the vibrator rig at KM (figure 12.1 on page 107), and the test were moved to HiST, no real testing of the casing could be achieved. The adjustability of the transducer was confirmed to work great, but other interesting factors like the affect of soft plastic (PLA) clamps on the damping ratio and by extension the power output could not be tested.

The tendencies registered while testing the system testing was low amplitude and large bandwidth which according to figure 3.11 on page 31 could be a sign of high damping ratio. This could be related to both the softness of the plastic material and the 'thickness' of the transducer clamp. Future design revisions should either include screws for securing the clamp, or using a harder material like steel or aluminium.

Power output

The power output of the system with the V21BL transducer was in the micro - milliwatt range. An output power of approx 0.5 mW at 0.5 g and approx. 1.4 mW at 1.5 g are considered as good results. These kinds of power outputs could enable the system to drive a variety of electronic devices and sensor nodes. The extreme test with no acceleration reference showed an output power of approx. 7 mW which is proof that a small piezoelectric transducer can achieve a large output power. The power output could probably have been pushed even higher with a more powerful vibrator.

One of the most interesting results was when loading the V21BL transducer with a 7.8 gram tip mass. The natural frequency of the transducer shifted down to about 40 Hz which was right in the area of interest. Looking back to figure 2.3 on page 15, the largest vibrational amplitude was given as 5.5 mm s^{-1} at 50 Hz which translates to approx. 0.25 g. This is a lower excitation than was tested, but looking at figure 12.12 it should be possible to harvest power even at these low amplitudes, although it would only be an assumption. Using a transducer more suitable for low excitation harvesting, or increasing the number of transducers could help improve the low-excitation power output of the system.

Chapter 14

Further work

Further work with the piezoelectric energy harvesting system includes:

- **Buck-boost converter.** If a commercially available buck-boost converter capable of interfacing to the piezoelectric transducer could be found, it is believed that it could help utilize other piezoelectric materials like PVDF. This should be looked into, and if a device is found, a prototype should be made.
- **Testing at higher and lower vibrational amplitude.** Testing over a larger range of amplitudes than was done in this project should be performed. Both the high and low amplitude behavior is of interest, but low amplitude is most important with regards to industrial and maritime applications.
- **Improved casing.** A better casing should be designed, keeping the adjustable clamping patent, but using screws to secure the clamp or a harder material to avoid high damping ratios in the system. Robustness should also be a key factor, and the IP57 standard could be a good benchmark for industrial environments.
- **Different commercial transducers** The transducer used in this project (V21BL) showed good performance, but there might be better suitable transducer available. More testing should be done with a selection of different transducers to map performance of materials and geometries.
- **Testing on a maritime vessel.** The system should be mounted on various locations on a maritime vessel to investigate what power outputs are achievable in a real-world application.
- **Damping parameters for COMSOL model.** The damping parameters for the COMSOL model should be found so that it can be used to estimate power output of different transducers materials and geometries.

- **Transducer tip loading.** A more thorough investigation into mass loading of the transducer should be performed to map the optimal length/weight ratio for larger power outputs.
- **Testing the system with multiple transducers.** Adding multiple transducers at different frequencies could increase the bandwidth of the system. Adding identical transducers with the same natural frequency could increase the output power.
- **Magnetic end mass.** When/if the transducer is to be fitted with an end mass, the mass could be a permanent magnet. Adding a coil around this magnet as it is displaced with the transducer could induce a current in the coil, supplementing the piezoelectric energy.

Chapter 15

Conclusion

In this thesis it has been proved that a piezoelectric energy harvesting system is achievable with technology readily available. The designed system was capable of harvesting up to 1.4 mW of power with vibrational excitations of up to 2 g (RMS) with the unaltered commercial transducer (V21BL). Adding a 7.8 gram end tip mass to the transducer lowered its natural frequency from 110 Hz^[31] to 40 Hz which is in the region of interest for industrial maritime applications. Although the LTC3588 power manager device showed good performance, it is suggested that improvements in DC-DC converter technology aimed for piezoelectric energy harvesting could further improve the results.

Modeling of piezoelectric transducers in COMSOL multiphysics was harder and more time-consuming than expected, and in the end the resulting model was only able to calculate eigenfrequencies of the system. This was disappointing compared to the possibilities if the goals of the model had been fully achieved. Although the model delivered weak results, the only lacking component of a fully working model was the damping ratio which could be estimated based on measurements from an existing system.

Building custom transducers were achieved without special equipment, but the results were not that great. 1 of 3 attempted transducers survived the production process, and although the successful transducer had promising open-circuit output voltages, no power could be extracted from it with the designed power manager device.. Without special production tools and equipment, it is best to use commercially available transducers. If a large quantity is needed, most manufacturers will custom make transducers for any application.

The casing of the transducer showed, despite faulty test results, signs of introducing damping to the system which in turn reduced the output power. This could not be

confirmed by the test results. The designed clamping system would allow tuning the frequency of the system during installation.

Combining the results for all tests and discussion in this thesis, the conclusion can be made that commercialization of a energy harvesting product is very achievable with today's available technology and components and with the ongoing research in material science and low power electronics we will likely be seeing an increasing number of piezoelectric energy harvesting systems.

Bibliography

- [1] D. Evans, “The internet of things - how the next evolution of the internet is changing everything,” *Cisco Internet Business Solutions Group*, April 2011.
- [2] M. Ballve, “Wearable gadgets are still not getting the attention they deserve — here’s why they will create a massive new market,” *Buisness Insider - Tech*, August 29th, 2013.
- [3] BBC Research LLC, “Global markets and technologies for wireless sensors (report highlights).” <http://www.bccresearch.com/market-research/instrumentation-and-sensors/wireless-sensors-technologies-markets-ias019a.html>, Februray 2012 - [Accessed 2014-06-18].
- [4] J. Liang and W.-H. Liao, “Energy harvesting and dissipation with piezoelectric materials,” in *Information and Automation, 2008. ICIA 2008. International Conference on*, pp. 446–451, June 2008.
- [5] MESH Engineering & Software Co., “Hydroelastic vibrational aspects of fluid-structure interaction simulations...” <http://www.mesh.com.tr/hydroelastic-vibration-analyses.html>, [Accessed 2014-06-21].
- [6] 1st International Ship Noise and Vibration Conference, *Ship vibration and noise: Some topical aspects*, (London), Loyd’s Register Technical Papers, June 2005.
- [7] Hannu Tienhaara - Wärtsilä Corporation, “Guidelines to engine dynamics and vibration.” http://www.lme.ntua.gr:8080/academic-info-1/prospheromena-mathemata/egkatastaseis-prooses/files/guidelines_dynamics_vibration.pdf, February, 2004 [Accessed 2014-06-21].
- [8] Piezo Systems Inc., “Introduction to piezoelectricity (*Application note*).” <http://www.piezo.com/catalog8.pdf%20files/Cat8.59-61.pdf>, [Accessed 2014-06-21].
- [9] Measurement Specialites, Inc., “Piezo Film Sensors - Technical Manual (1005663-1 Rev. B 2002),” April, 1999.

- [10] A. Daniels, M. Zhu, and A. Tiwari, "Evaluation of piezoelectric material properties for a higher power output from energy harvesters with insight into material selection using a coupled piezoelectric-circuit-finite element method," *Ultrasonics, Ferroelectrics and Frequency Control, IEEE Transactions on*, vol. 60, pp. 2626–2633, Dec 2013.
- [11] R. Lakes , University of Wisconsin, "Introduction to viscoelastic composites." <http://silver.neep.wisc.edu/~lakes/VECmp.html>, [Accessed: 2014-05-12].
- [12] E. Oberg, F. D. Jones, H. L. Horton, and H. H. Ryffel, *Machinery's Handbook*. Industrial Press Inc., 27th ed., 2004.
- [13] H. Young, R. Freedman, and L. Ford, *Sears and Zemansky's University Physics*. No. v. 12, Addison-Wesley, 2008.
- [14] Dr. M. A. Kamoji - KLE Society's college of Engineering & Technology, "Forced Vibrations." <http://elearning.vtu.ac.in/14/enotes/Mech%20vib/4&5-MAKamoji.pdf>, [Accessed 2014-06-27].
- [15] R. Boylestad, *Introduction to Circuit Analysis*. Prentice Hall international editions, Prentice Hall PTR, 1997.
- [16] N. Kong, D. S. Ha, A. Erturk, and D. J. Inman, "Resistive impedance matching circuit for piezoelectric energy harvesting," *Journal of Intelligent Material Systems and Structures*, vol. 21, no. 13, pp. 1293–1302, 2010.
- [17] DigiKey Corporation, "Electronic Components Distributor." <http://www.digikey.com/>.
- [18] Maxim Integrated, "APPLICATION NOTE 4087: An introduction to switch-mode power supplies." <http://www.maximintegrated.com/en/app-notes/index.mvp/id/4087>, [Accessed 2014-06-26].
- [19] Maxim Integrated, "TUTORIAL 2031: DC-DC Converter Tutorial." <http://www.maximintegrated.com/en/app-notes/index.mvp/id/2031>, [Accessed 2014-06-26].
- [20] G. Ottman, H. Hofmann, and G. Lesieutre, "Optimized piezoelectric energy harvesting circuit using step-down converter in discontinuous conduction mode," *Power Electronics, IEEE Transactions on*, vol. 18, pp. 696–703, Mar 2003.
- [21] Wikimedia Commons, "A database of 21,637,254 freely usable media files to which anyone can contribute." <http://commons.wikimedia.org/>.

- [22] Hearst Business Communications, Inc., “Electronic Products - What is the best type of battery?.” http://www.electronicproducts.com/Power_Products/Batteries_and_Fuel_Cells/What_is_the_best_type_of_battery.aspx, [Accessed: 2014-06-30].
- [23] K. Bulls, “Solid-state batteries - high-energy cells for cheaper electric cars,” *MIT Technology Review*, May / June 2011.
- [24] P. Mars, “Coupling a supercapacitor with a small energy-harvesting source,” *EDN Network*, June 2012.
- [25] LPKF Laser and Electronics, “ProtoMat S103 Product page.” <http://www.lpkf.com/products/rapid-pcb-prototyping/circuit-board-plotter/protomat-s103.htm>, [Accessed: 2014-06-30].
- [26] Altium Limited, “Altium website.” <http://www.altium.com/>, [Accessed 2014-06-29].
- [27] Siemens, “Solid Edge ST6 Academic version [Product download].” https://www.plm.automation.siemens.com/en_us/academic/resources/solid-edge/student-download.cfm, [Accessed 2014-06-29].
- [28] National Instruments, “Official website, year =”
- [29] COMSOL Inc., “Comsol website.” <http://www.comsol.com/>, [Accessed 2014-06-29].
- [30] COMSOL Inc., “Comsol documentation,” [Accessed 2014-06-29].
- [31] Midé, “Volture piezoelectric energy harvesters (datasheet).” http://www.mide.com/pdfs/Volute_Datasheet_001.pdf, January 23rd, 2013.
- [32] Precision Acoustics, “PVDF Student kit - Datasheet.” <http://acoustics.co.uk/products/piezo-electric-materials/student-starter-kit/students-datasheet/>, [Accessed: 2014-06-30].
- [33] MG Chemicals, “Silver Conductive Epoxy (datasheet).” <http://media.digikey.com/pdf/Data%20Sheets/MG%20Chemicals%20PDFs/Silver%20Conductive%20Epoxy.pdf>, [Accessed: 2014-06-30].
- [34] Midé, “Volture products - material properties.” http://www.mide.com/pdfs/volute_material_properties_2010.pdf.
- [35] Linear Technology Corporation, “Ltc3588-1 piezoelectric energy harvesting power supply.” <http://http://cds.linear.com/docs/en/datasheet/35881fa.pdf>, [Accessed 2014-06-07].

- [36] Cymbet Corporation, “EnerChip CBC050 (datasheet).” <http://www.cymbet.com/pdfs/DS-72-01.pdf>, [Accessed: 2014-07-01].
- [37] Linear Technology, “LTC4071 - Li-Ion/Polymer Shunt Battery Charger System with Low Battery Disconnect (datasheet).” <http://cds.linear.com/docs/en/datasheet/4071fc.pdf>, [Accessed: 2014-07-01].
- [38] Nichicon, “Solid Tantalum Electrolytic Capacitors.” <http://nichicon-us.com/english/products/pdfs/e-f97.pdf>, [Accessed: 2014-07-01].
- [39] SparkFun Electronics, “IMU Analog Combo Board - 5 Degrees of Freedom IDG500/ADXL335 - Product page.” <https://www.sparkfun.com/products/retired/9268>, [Accessed: 2014-07-01].
- [40] Analog Devices, “ADXL335 - Small, Low Power, 3-Axis 3 g Accelerometer.” http://www.analog.com/static/imported-files/data_sheets/ADXL335.pdf, [Accessed: 2014-07-01].
- [41] Assmann Components, “Cat6 SSTP Patch cable, 26 awg, coloed (Datasheet).” http://www.assmann.us/specs/A-MCSSP60010_Y-R.pdf, [Accessed: 2014-07-01].
- [42] European Union, “Denominations and technical specifications of euro coins.” http://europa.eu/legislation_summaries/economic_and_monetary_affairs/introducing_euro_practical_aspects/125028_en.htm, [Accessed: 2014-07-01].
- [43] Kemet Electronic Components, “Tantalum surface mount capacitors.” http://www.kemet.com/Lists/ProductCatalog/Attachments/254/KEM_T2005_T491.pdf, [Accessed: 2014-07-04].
- [44] AVX, “F93 series - resin-molded chip, standard tantalum j-lead.” <http://www.avx.com/docs/Catalogs/f93.pdf>, [Accessed: 2014-07-04].

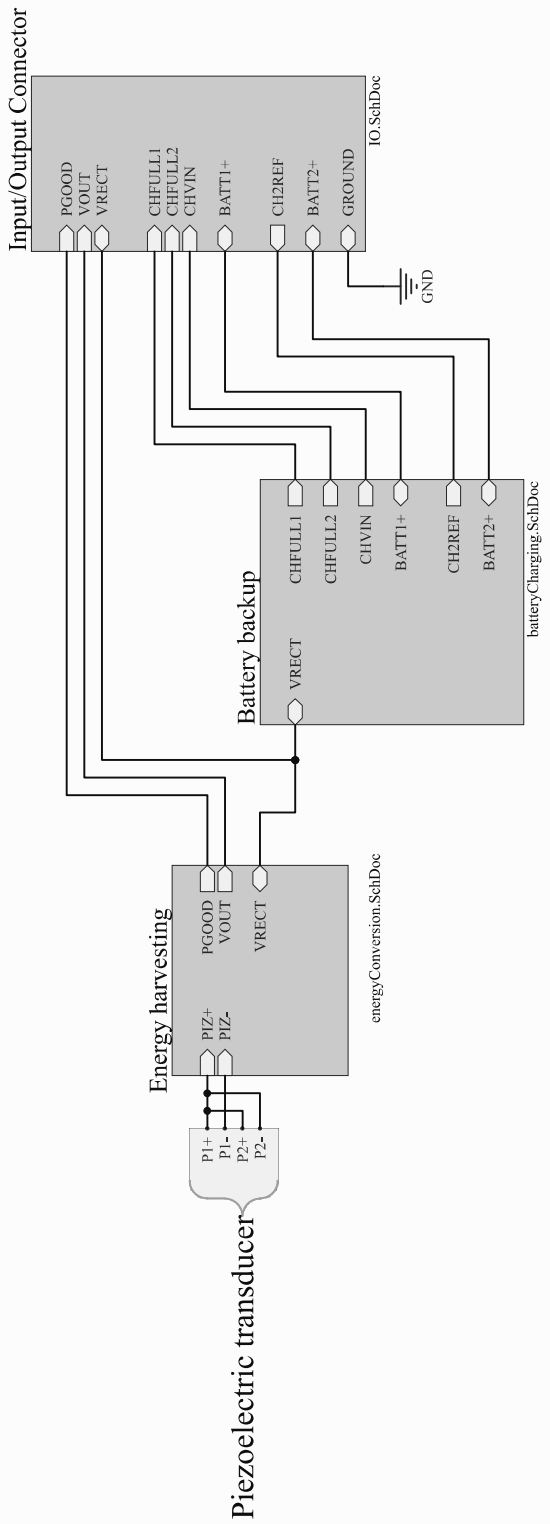
Part VI

Appendices

A Schematic - Sheet overview

4

A



1

2

3

4

B

C

D

Title PEEH.PjPcb

Sheet overview

Size	Number	Revision
A4	MGE201406-PEEH0	1.0

Date: 2014-06-26
File: C:\ownCloud\..\sheets.SchDoc

Sheet 0 of 3
Drawn By: Mats Granmo Eliassen

4

B Schematic - Power management

4 3 2 1

A

1

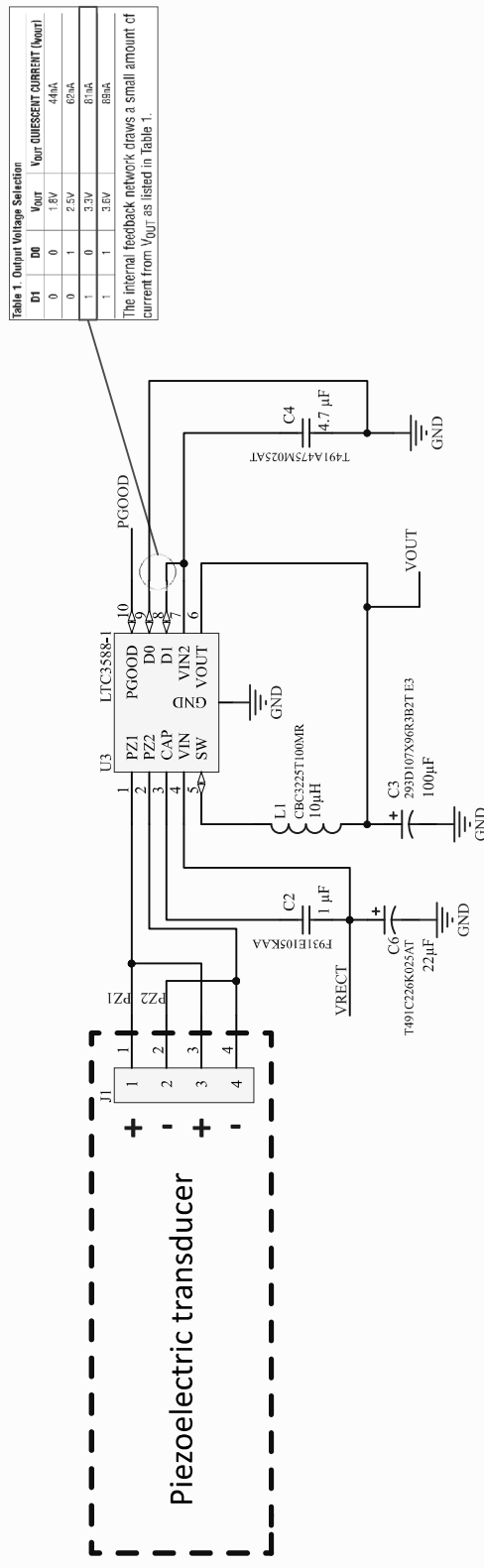


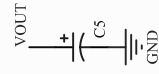
Table 1 Output Voltage Selection

Table 1. Output Voltage Selection			
D1	D0	Vout	V _Q (QUIESCENT CURRENT) (mV)
0	0	1.6V	44mA
0	1	2.5V	62mA
1	0	3.3V	61mA
1	1	3.6V	68mA

The internal feedback network draws a small amount of current from V_{out} as listed in Table 1.

The internal feedback network draws a small amount of current from V_{HIT} as listed in Table 1.

Dummy component for enabling increasing of the output capacitance (C4)



Power management circuit

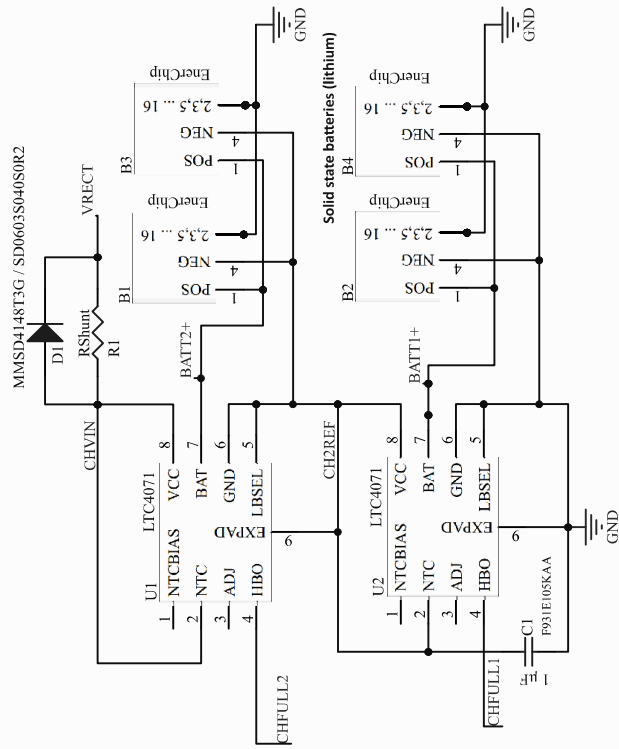
Title	PEEH.PjPcb
Size	Numbr
A4	1

01

D1

Sheet 1 of 3

C Schematic - Power storage



寸

1

6

1

Title	PEEH-PIPeb		
Size	Long Term Energy Conservation & Backup Power		
A4	Number	MGE201406-PEEH02	Revision 1.0
Date:	2014-06-23	C:\ownCloud\batteryChanging.SchDoc	Sheet of 3 Mats Grammo Eliasson
File:			Drawn By:

D Schematic - Input/Ouput

4

A

A

B

B

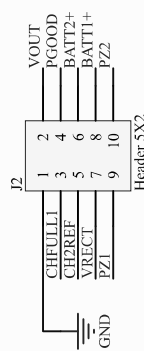
B

C

C

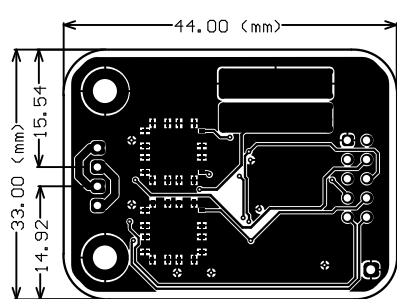
D

D

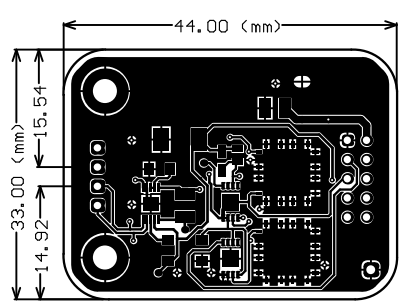


Title PEEH.PjPcb		Input/Output		Revision
Size	Number	MGE201406-PEEH03		
A4				1.0
Date:	2014-06-26	Sheet 3 of 3		
File:	C:\ownCloud\10.SchDoc	Drawn By:	Mats Granmo Eliassen	4

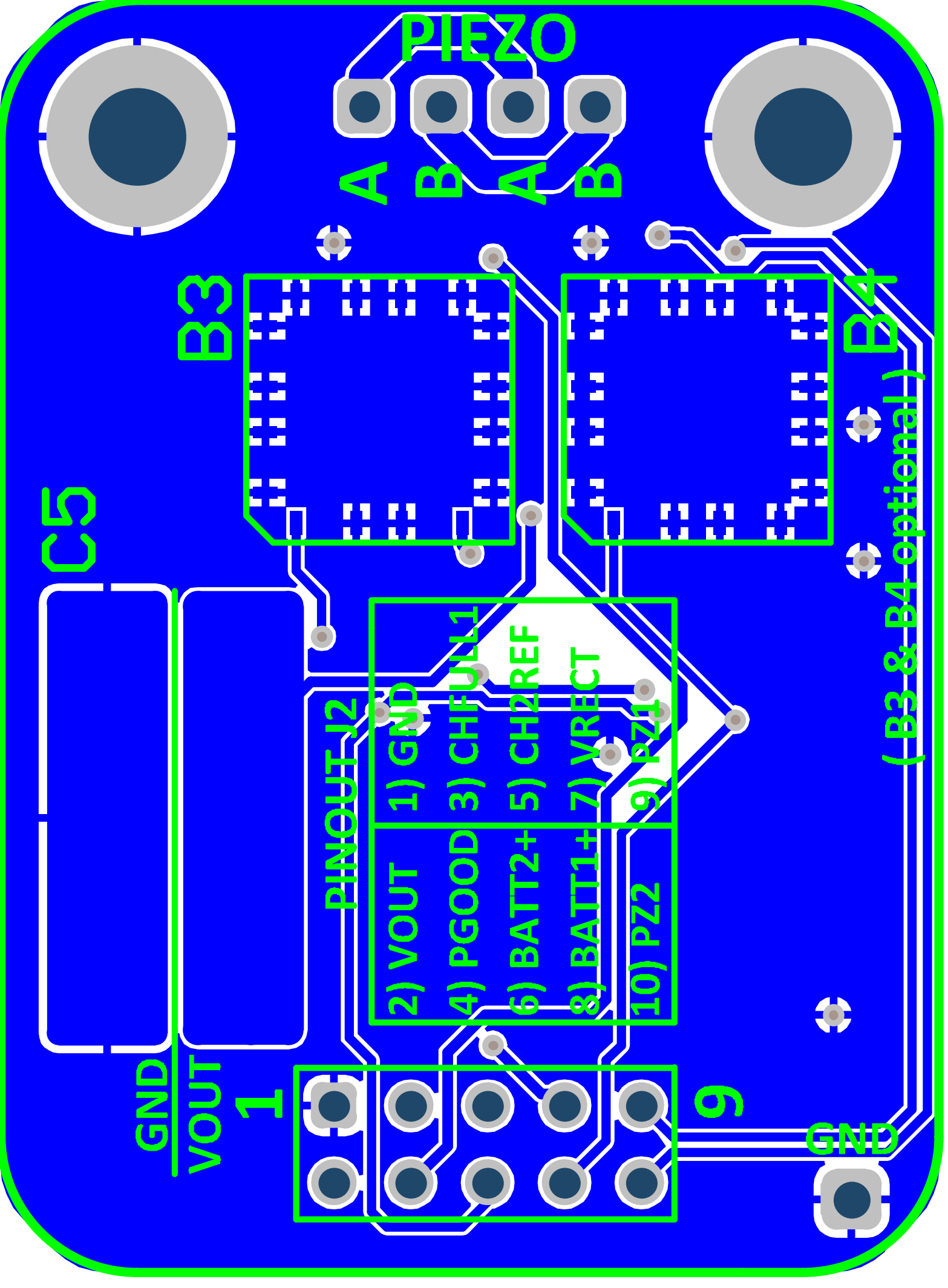
**E Gerber - Bottom layer
(approximate scale)**



**F Gerber - Top layer
(approximate scale)**



**G Gerber - Bottom layer
w/overlay (enlarged and
mirrored)**

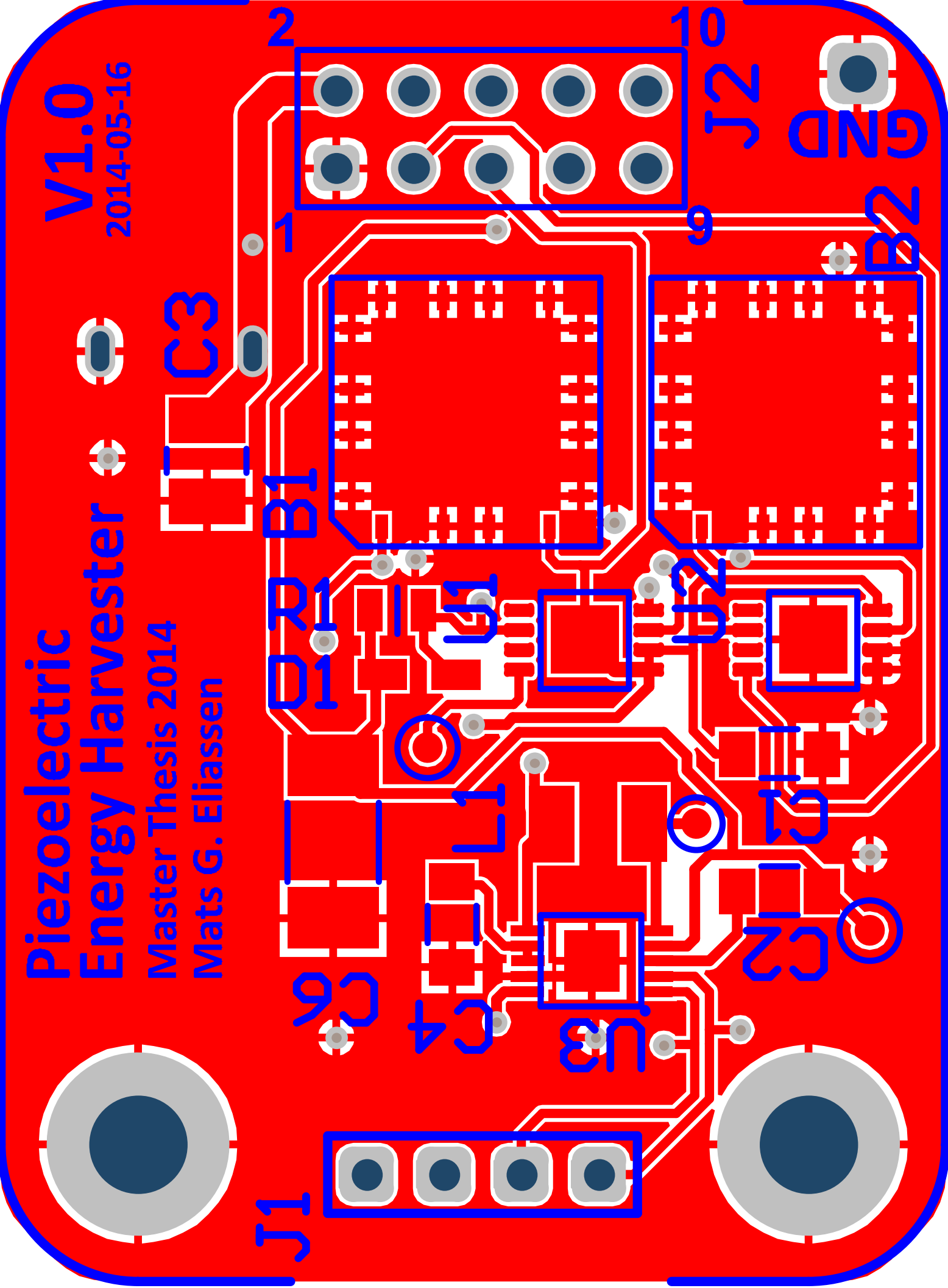


**H Gerber - Top layer w/overlay
(enlarged)**

Piezoelectric Energy Harvester

Master Thesis 2014
Mats G. Eliassen

V1.0
2014-05-16



I Mechanical drawing - Casing Bottom

REVISION HISTORY

REV	DATE	APPROVED
-----	------	----------

DESCRIPTION

DRAWN	NAME	DATE
CHECKED	Mats	06/25/14
ENG APPR		
MGR APPR		

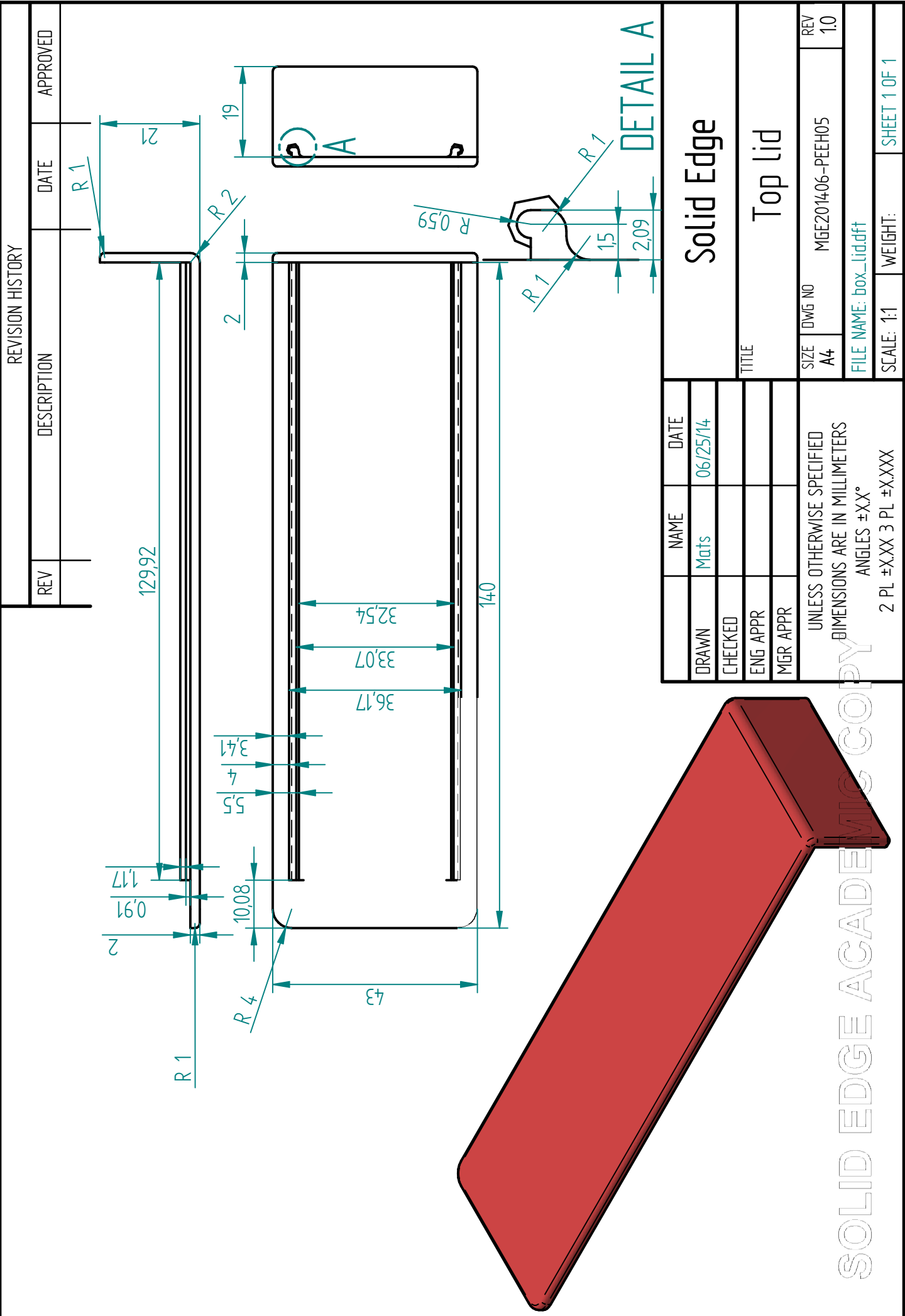
DETAIL A

DETAIL B

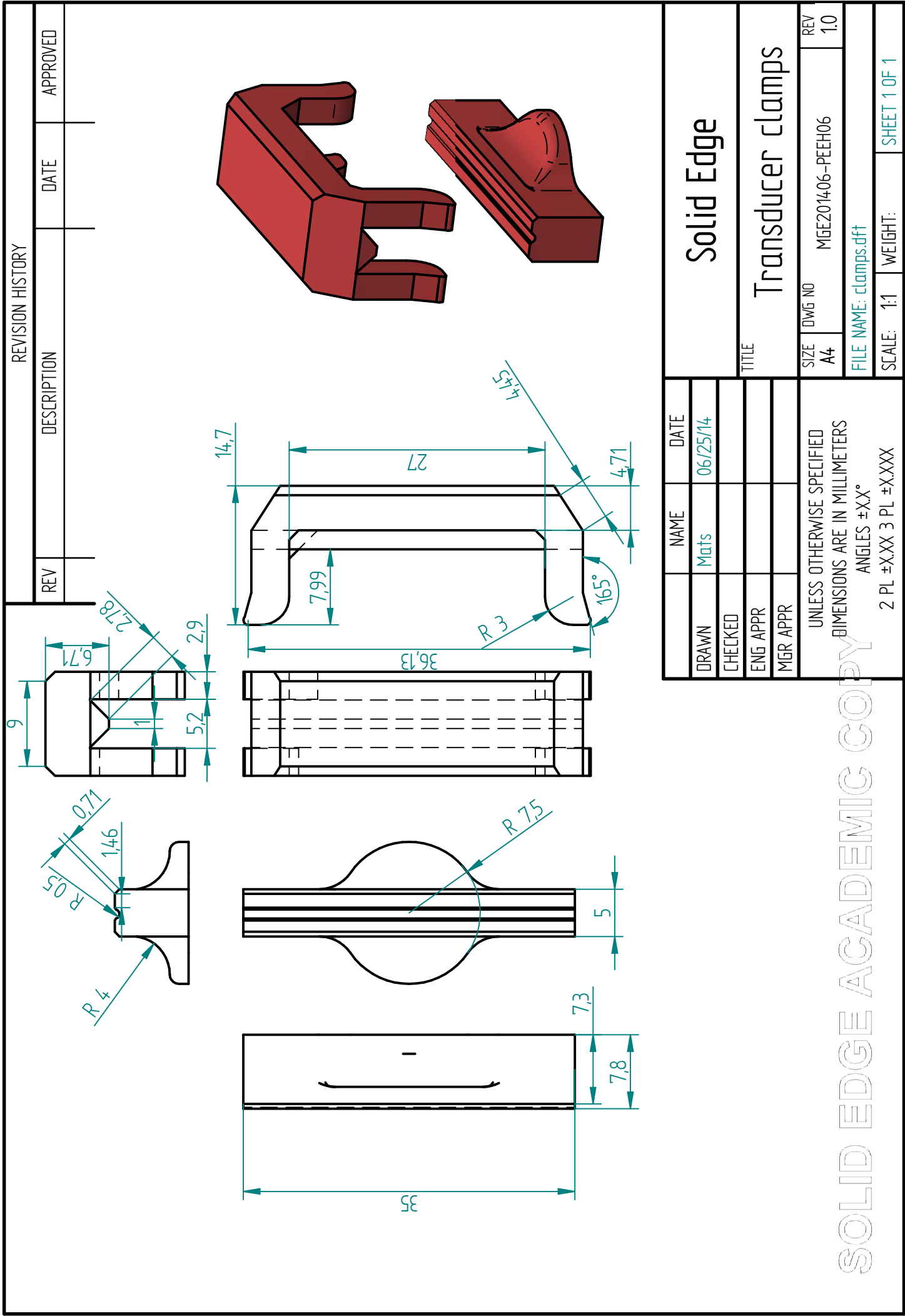
SOLID EDGE Academic Copy

SHEET 1 OF 1

J Mechanical drawing - Top Lid



K Mechanical drawing - Transducer clamps



L - MATLAB script for frequency response

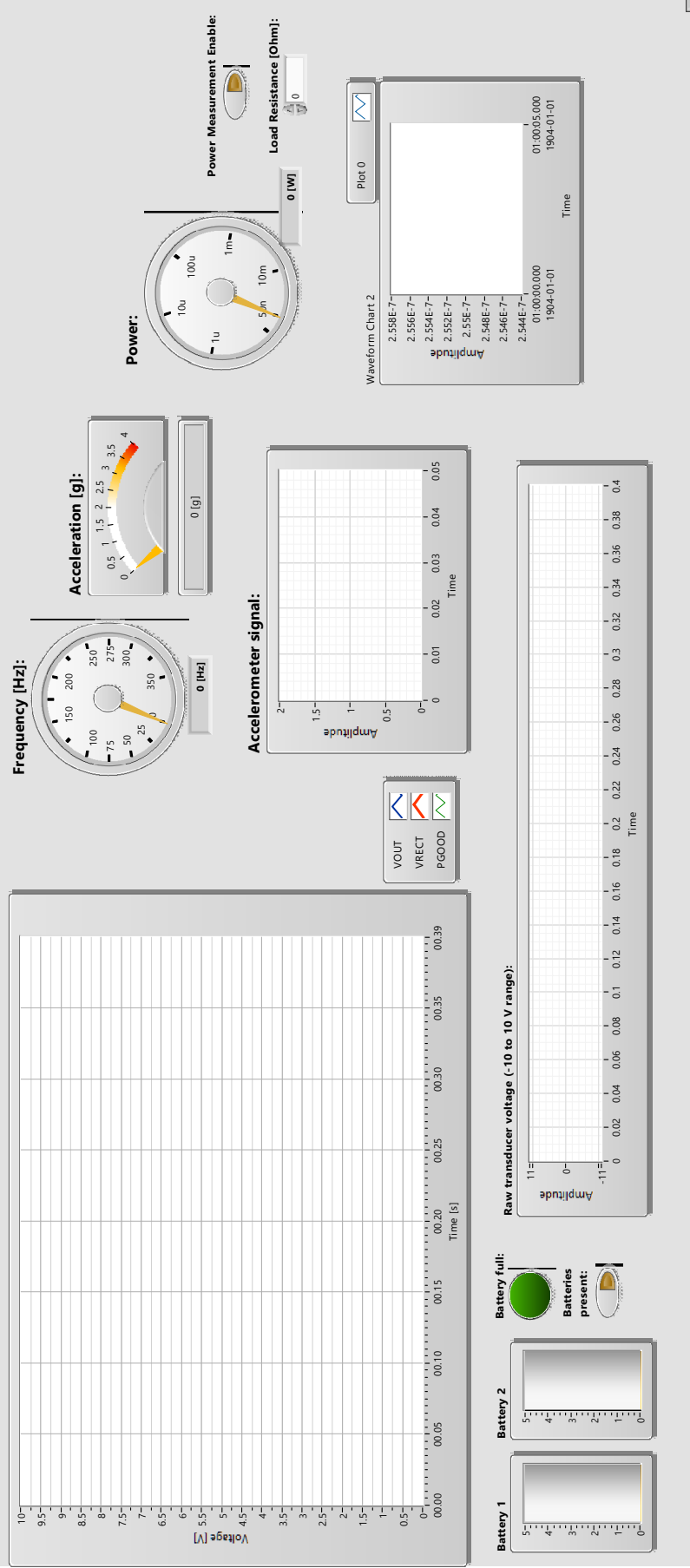
```
1 clear;
2 m = 0.01; %kg
3
4 c = 0.5%Dampin ratio
5 a = 9.80665;
6 k = 1579136.7;%1.93*100 %1.93 N/mm -> kg/mm
7 F = m*a;
8
9 fn = (1/2*pi)*(sqrt(k/m))
10
11 F = m*a
12 %X = zeros(1,20);
13 PShift = 0;
14
15
16 c = 0
17 k = 1;
18
19 for c=0:0.1:1
20     i = 1;
21     for r=0:0.000005:2
22         %X2(i,k) =
23         X(i,k) = ( 1 / sqrt(((1-r)^2)+((2*c*r)^2))); %(F/k)*
24         PShift(i,k) = atan((2*c*r)/(1-(r^2)));
25         ir(i,k) = r;
26         i = i+1;
27     end;
28     k = k+1
29 end;
30 X(isinf(X)) = max(max(X(~isinf(X))));
31 figure()
32 hold on
33 for l =1:k-1
34     plot(ir(:,l),X(:,l),'LineWidth',3)
35 end;
36 set(gca,'yscale','log')
37 legend('0','0.1','0.2','0.3','0.4','0.5','0.6','0.7','0.8','0.9','1')
```

```
40
41 figure()
42 hold on
43 for l =1:k-1
44     plot(ir(:,l),PShift(:,l),'LineWidth',3)
45 end;
46 set(gca,'yscale')
47 legend('0','0.1','0.2','0.3','0.4','0.5','0.6','0.7','0.8','0.9','1')
48 grid
```

M - Documentation output for developed LabVIEW measurement system

Piezoelectric Energy Harvesting

Measurement and verification system





Page 2

Measurement.vi
C:\ownCloud\Projects\School\Masteroppgave\Hovedoppgave\LabVIEW\Measurement.vi
Last modified on 2014-07-06 at 20:03
Printed on 2014-07-06 at 20:04

